ABSTRACT

Schneider, Ian Christopher. Engineering Analysis of Spatial Gradient Sensing in Platelet-derived Growth Factor-stimulated Fibroblasts (Under the direction of Jason M. Haugh)

Wound healing is a well-coordinated process in which different cell types invade the wound at different times, secreting different enzymes and factors. An important event in this process is the proliferation and directed migration of dermal fibroblasts. Evidence has shown that gradients of platelet-derived growth factor (PDGF) mediate the process of directed cell migration in fibroblasts. These cells use membrane lipids, specifically 3' phosphoinositides (PIs), to spatially sense the extracellular PDGF gradient by creating an intracellular gradient of 3' PIs. PDGF receptor stimulates 3' PI production by activating phosphoinositide 3-kinase (PI 3-kinase), a lipid kinase. However, the mechanism by which the cell generates intracellular 3' PI gradients is not well known in fibroblasts.

A 3' PI specific binding domain fused to a fluorescent protein can be used as a 3' PI probe and can be imaged quantitatively using total internal reflection fluorescence (TIRF) microscopy. This technique allows for the selective illumination of the adherent portion of the cell membrane, providing a powerful technique to visualize protein translocation to the membrane in live cells. A mathematical model has been developed to quantitatively analyze the fluorescence data and we show here that these data are sufficient to set bounds on parameters that determine 3' PI production, diffusion and degradation. Under uniform PDGF stimulation we also find areas of differentially controlled 3' PI production, diffusion and degradation that can be linked to the specific morphology of the cell. This indicates that cell polarization may play an important role in PI 3-kinase signaling. Finally, we find that fibroblasts sense gradients in a manner distinct from other more common chemotactic models such as *Dictyostelium discoideum* and neutrophils. Fibroblasts are only sensitive to large relative PDGF gradients and intermediate PDGF concentrations. Consequently, the ability of these cells to spatially sense relies on the competition between the intrinsic bias caused by cell polarization and the external bias caused by the PDGF gradient, each of which may have different contributions depending on the extracellular gradient conditions.

Engineering Analysis of Spatial Gradient Sensing in Platelet-derived Growth Factor-stimulated Fibroblasts

by

Ian Schneider

A dissertation submitted to the Graduate Faculty of North Carolina State University
in partial fulfillment of the requirements for the
Degree of Doctor of Philosophy

CHEMICAL AND BIOMOLECULAR ENGINEERING

Raleigh, NC
August 2005

APPROVED BY:

_____	_____
(Chair of Advisory Committee)	(Robert M. Kelly)
(Jason M. Haugh)	
_____	_____
(John H. van Zanten)	(Nina S. Allen)

PERSONAL BIOGRAPHY

Ian Schneider was born on April 7th, 1978 in Des Moines, Iowa. He grew up with his parents, Chris and Molly and his two younger sisters Sarah and Emily in the small bedroom-community of Carlisle, Iowa. Very early in life Ian indicated that he wanted to pursue a career as a professor at a university in an undetermined field. Through high school he developed a love for math and science, particularly chemistry and biology, while still having time to play the trumpet in jazz band and participate in sports such as golf and football. Because of his love for math and science, he enrolled at Iowa State University, where he studied to become a chemical engineer. Attending Iowa State University was a life-changing experience. Ian got his first taste of research under the direction of Peter Reilly, working on artificial rumen fermentation. Professor Reilly was quite supportive, fueled his interest in research and solidified his desire to attend graduate school. Ian also met his future wife, Maria Meisch in Professor Reilly's laboratory six weeks before he left for graduate school at North Carolina State University. They eventually married on June 19th, 2004 in Maria's hometown of Dyersville, Iowa.

ACKNOWLEDGEMENTS

My experience here at North Carolina State University has been wonderful and truly memorable. Successfully navigating the Ph.D. program in the Department of Chemical and Biomolecular Engineering is one of the hardest things that I have ever done and required a lot of help and encouragement from many people in my life. I would first like to thank my advisor, Dr. Jason Haugh for allowing me to join the lab. While I still have much to learn, he has taught me a lot about research as well as how to run a successful laboratory, each of which will be crucial to my own success in the future, if I am to pursue a faculty position. I would also like to acknowledge the rest of my committee for their encouragement and support, particularly Dr. Nina Allen who has taught me so much about light microscopy. I owe a great debt to Yue Xu in the Botany Department for technical support pertaining to generating gradients (Chapter 5). I would also like to thank the rest of the students and post-docs in the Haugh laboratory for helpful discussions on topics related and unrelated to research, and in particular Michael Weiger for his help generating figures. I was also very lucky to work with a wonderful undergraduate student, Elizabeth Parrish, who helped with the analysis of the hot and cold spots in Chapter 4. Finally, I must thank my family for their confidence and encouragement, especially my wife, Maria, who was by my side, providing unwavering support during the frustrations as well as the successes over the past years.

TABLE OF CONTENTS

LIST OF TABLES

Pages

LIST OF FIGURES

Pages

Chapter 1
Wound Healing at the Cellular and Molecular Level: Understanding Chemotaxis

1.1 MOTIVATION

Wound healing is a well-coordinated series of events in which different cell types that perform different tasks invade the wound at different times (Clark 1996; Martin 1997). Very quickly after cutaneous wounding, the blood clotting cascade is initiated and a fibrin mesh is formed. This fibrin mesh both traps platelets, causing their degranulation, and provides a provisional matrix upon which invading cells migrate. The platelet degranulation process releases α-granules, rich in growth factors such as platelet-derived growth factor (PDGF), which diffuses from the wound site into the surrounding tissue, signaling cells that an injury has occurred (Deuel and others 1991; Pierce and others 1991; Pierce and others 1989).

One of the first cell types to invade the wound is the neutrophil. When a wound is formed, the walls of the surrounding blood vessels change and allow these cells to pass through on their way toward the clot. Neutrophils are directed by cytokines, released in the wound and formyl peptides, released as byproducts from bacterial metabolism. Although neutrophils can secrete growth factors and cytokines, their primary role is to clear the wound by phagocytosing foreign pathogens. This role is easily filled by neutrophils because their migration is rapid allowing them to catch relatively fast moving bacteria.

Macrophages are also recruited to the wound on slightly longer timescales as compared to neutrophils. They perform similar functions, but also provide a potent source of PDGF. This second wave of PDGF is important because dermal fibroblasts, which are recruited to the wound by PDGF, must emerge from quiescence and change transcriptional profiles before they begin to proliferate and migrate (Martin 1997; Pierce and others 1991). This process may take days and thus this additional source of PDGF, separate from platelet degranulation is crucial. Fibroblasts' primary role at the wound site is to remodel and excrete extracellular matrix in order to provide a scaffold for new tissue. A secondary role is to contract the wound, helping to pull the edges of the wound towards each other (Deuel and

others 1991; Pierce and others 1989). When fibroblasts cannot migrate to the wound and perform these jobs adequately, wound healing is delayed or stopped completely.

Fibroblast invasion occurs through a cellular process called chemotaxis, which is the directed migration of cells in response to a soluble extracellular ligand gradient. In cell culture, fibroblasts show a strong chemotactic behavior towards PDGF and inhibiting PDGF signaling abolishes chemotaxis in fibroblasts (Kundra and others 1994; Wennstrom and others 1994a; Wennstrom and others 1994b). This supports the idea that gradients of PDGF in the tissue recruit fibroblasts to the wound site. We are only starting to uncover the molecular mechanisms by which PDGF stimulates directed migration of fibroblasts. Insights into how fibroblasts sense gradients of PDGF and convert this information into biased migration may lead to further understanding of the overall process of wound healing. This knowledge could suggest therapeutic interventions aimed at enhancing wound healing rates or possibly inhibiting the formation of scar tissue.

1.2 INTRODUCTION

The entire process of wound healing heavily rests on a cell's ability to take in cues from the environment, integrate them and produce a specific response. One way in which cells can access information from their environment is by sensing certain molecules in the extracellular space. Cells express proteins on the surface of the plasma membrane called receptors, which can specifically bind these extracellular molecules or ligands. These receptors contain three general domains; an extracellular domain mediates recognition of the ligand, a transmembrane domain anchors the receptor in the plasma membrane, and an intracellular domain facilitates interaction with intracellular signaling molecules. When a ligand binds the extracellular domain of a receptor, it induces the receptor to either oligomerize or change conformation. This oligmerization or conformational change is transduced to the intracellular environment of the cell and activates signaling pathways that elicit a cellular response appropriate for a given ligand.

Many receptors have a high specificity for a ligand or family of ligands, affording the cell the ability to link specific cellular responses to specific ligands. However, similar signaling pathways are used by a number of different receptors so the cell must make a decision based on additional information, such as the timing and spatial localization of the pathway. Consequently, knowing which pathways are activated is not enough to understand how a given cell makes a decision based on an environmental cue. One must understand the kinetics and spatial localization of the ligand-receptor interaction and downstream signaling in order to understand why cells respond in a given manner.

1.2.1 Platelet-derived growth factor

As mentioned above fibroblasts are directed to migrate to wound sites by sensing gradients of PDGF. PDGF exists as a homo or heterodimer, composed of either A, B, C or D monomers, the most common being A and B (Heldin and Westermark 1999; Westermark and Sorg 1993). These monomers form the dimers PDGF-AA, -AB, -BB, -CC, and -DD. Our main interest is in PDGF-BB, hereinafter referred to as PDGF, because it has approximately the same affinity for PDGF-α and -β receptors (Ostman 1989). PDGF receptor comes in

only two flavors, α and β. The β-isoform is most often associated with fibroblast migration and is expressed more highly in the cell line used in this study (NIH3T3 fibroblasts) (Grotendorst and others 1991; Heldin and Westermark 1999), consequently for the duration of this manuscript PDGF receptor-β will be referred to as PDGF receptor. PDGF receptor is in the family of receptor tyrosine kinases, which contain a kinase domain in the intracellular tail of the receptor (Schlessinger 2000; Vandergeer and others 1994). This kinase domain is activated when a PDGF dimer crosslinks two PDGF receptors, allowing it to phosphorlyate tyrosine residues in trans on the tails of the receptors in the dimer (fig. 1.1). These tyrosine residues are then able to recruit and activate molecules in specific signaling pathways.

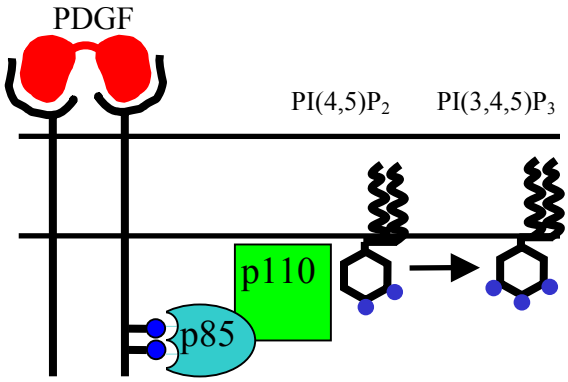

Figure 1.1: PI 3-kinase is activated by PDGF receptor- The p85 adaptor subunit of class IA PI 3-kinasess binds phosphorylated PDGF receptor. The p110 subunit of PI 3-kinase catalyzes the reaction of $PI(4,5)P_2$ to $PI(3,4,5)P_3$.

1.2.2 Phosphoinositide 3-kinase and 3' phosphoinositides

One pathway that is robustly activated by the PDGF receptor is the phosphoinositide (PI) 3-kinase pathway (Hawkins and others 1997; Rameh and Cantley 1999; Vanhaesebroeck and Waterfield 1999; Wymann and Pirola 1998). PI 3-kinase is a lipid kinase that phosphorylates membrane phosphoinositides on the 3' position (fig. 1.1). Notably, PI 3-kinase has been shown to be required for PDGF-mediated chemotaxis. Experiments with fibroblasts using mutant receptors, PI 3-kinase inhibitors (wortmannin or LY294002), or dominant-negative PI 3-kinase constructs showed no chemotaxis toward PDGF (Kundra and others 1994; Wennstrom and others 1994a; Wennstrom and others 1994b). Inhibition of PI 3-kinase also abolishes membrane ruffling and lamellipod formation (Haugh and others 2000; Hooshmand-Rad and others 1997; Wymann and Arcaro 1994). Lamellipod formation

along with membrane ruffling represent membrane activity that results from dynamic changes in the actin network initiated by PDGF signaling. These results coincide with evidence that PI 3-kinase is upstream of Rac, a signaling molecule also involved in controlling actin dynamics leading to membrane ruffling and lamellipod formation in fibroblasts (Anand-Apte and others 1997; Hooshmand-Rad and others 1997; Ridley and others 1992).

The isoforms of PI 3-kinases that engage activated PDGF receptors are of class IA. The class IB PI 3-kinase is activated by G-protein coupled receptors (GPCRs) and is involved in chemotactic signaling in the slime mold, *Dictyostelium discoideum* and neutrophils. While *in vitro* studies have shown some promiscuity, the preferred *in vivo* substrate for class I PI 3-kinases is phosphatidylinositol (4,5) bisphosphate (PIP2). This substrate is phosphorylated to form phosphatidylinositol (3,4,5) trisphosphate (PIP3) (fig. 1.1) (Hawkins and others 1997; Vanhaesebroeck and Waterfield 1999; Wymann and Pirola 1998). PIP3 can, in turn, be dephosphorylated to phosphatidylinositol (3,4) bisphosphate ($PI(3,4)P_2$) by the lipid phosphatase SHIP. Class IA PI 3-kinases contain two subunits, a regulatory subunit and a catalytic subunit. The 85kD regulatory subunit interacts with the PDGF receptor tail through dual Src-homology-2 (SH2) domains (fig. 1.1). SH2 domains are modular domains found in many proteins and facilitate binding to phosphorylated tyrosine residues. The regulatory subunit binds the 110kD catalytic subunit via an SH3 domain/proline rich interaction and thus acts as an adaptor. When the regulatory domain binds the receptor it both activates the catalytic domain and brings it in close proximity to its substrate PIP2.

The 3' PI lipid products of PI 3-kinase, $PI(3,4)P_2$ and PIP3, are of particular interest because they are known to bind specific pleckstrin-homology (PH) domains found in many cytosolic signaling proteins (Blomberg and others 1999; Lemmon and others 2002; Lemmon and others 1996; Shaw 1996). In fact the activation of Rac is thought to be mediated by recruitment of Rac activators to the membrane via PH domains (Welch and others 2003). One particular PH domain-containing protein receiving much attention, because of its role in promoting cell survival is Akt/PKB. The AktPH domain fused to green fluorescent protein (GFP) has been used frequently as a probe of the 3' PI lipid concentration in the membrane

(Haugh and others 2000; Kontos and others 1998; Meili and others 1999; Servant and others 2000). This probe has moderate affinity towards $PI(3,4)P_2$ and PIP3 (*in vitro* K_d ~0.57 μM and ~0.4 μM, respectively) (Frech and others 1997), but fast on and off rates (Marshall and others 2001). Bound and unbound probe then exist in pseudo-equilibrium on the time scale of 3' PI lipid kinetics, essentially tracking membrane lipid concentration.

1.2.3 Phosphatase and tensin homologue deleted on chromosome 10

Phosphatase and tensin homologue deleted on chromosome 10 (PTEN) is a 3' phosphoinositide phosphatase the controls the reverse reaction of PIP3 to PIP2 (as well as $PI(3,4)P_2$ to PI(4)P) and thus antagonizes PI 3-kinase signaling (Leslie and Downes 2004). Phophatases have traditionally been thought of as background, mere requirements for reversibility and not controlled actively by the cell. However, PTEN plays an important role in PI 3-kinase signaling. It is known that in several human cancers, mutations in PTEN allow PI 3-kinase activity to go unchecked, which produces cells with high proliferation and survival characteristics (Leslie and Downes 2004; Tamura and others 1999). PTEN's importance also extends to migration where PTEN null *D. discoideum* cells chemotax less efficiently (Iijima and Devreotes 2002; Iijima and others 2004). Unfortunately, the regulation of PTEN is extremely complex and seems to differ between species (Lacalle and others 2004; Li and others 2005; Li and others 2003; Xu and others 2003). In *D. discoideum*, upon receptor stimulation PTEN is deactivated via translocation from the plasma membrane to the cytosol (Iijima and Devreotes 2002). On the other hand mammalian PTEN seems to be at the membrane before and after receptor stimulation, thus its activity may be controlled by tyrosine/threonine/serine phosphorylation, binding with acidic memberane or redox potential rather than membrane translocation (Leslie and Downes 2004). Even through PTEN seems to play a large part in PI 3-kinase signaling, much is still unknown about how it is regulated spatially and whether receptors can modulate its activity.

1.3 BACKGROUND

1.3.1 Chemotaxis: spatial sensing, polarization and the migration cycle

In order for cells to chemotax, they must be able to translate an extracellular concentration gradient of ligand into an intracellular biochemical signal via cell surface receptors. It is well established that bacterial cells employ a temporal sensing mechanism in order to sense chemical gradients (Berg 1978; Berg and Brown 1972). Bacterial cells sample extracellular ligand concentrations at different times; if the signal of a chemoattractant decreases or a chemorepellent increases the flagella reverse their direction of motion, causing the bacterium to tumble. This allows the cell to randomly choose another direction, but requires that the bacterium adapt to a given concentration of chemoattractant (Block and others 1982; Block and others 1983). Because of their size, eukaryotic cells (~20 μm) can rely on spatial sensing rather than the aforementioned temporal sensing. Instead of sampling ligand concentrations at different time points, eukaryotic cells sample ligand concentrations at different locations, a mechanism called spatial sensing (fig. 1.2). A cell in a gradient of chemoattractant will have more activated receptors at the front of the cell than at the back of the cell, consequently there will be more intracellular signaling at the front of the cell as compared to the back. Once the direction of migration has been chosen, the cell must progress through the migration cycle.

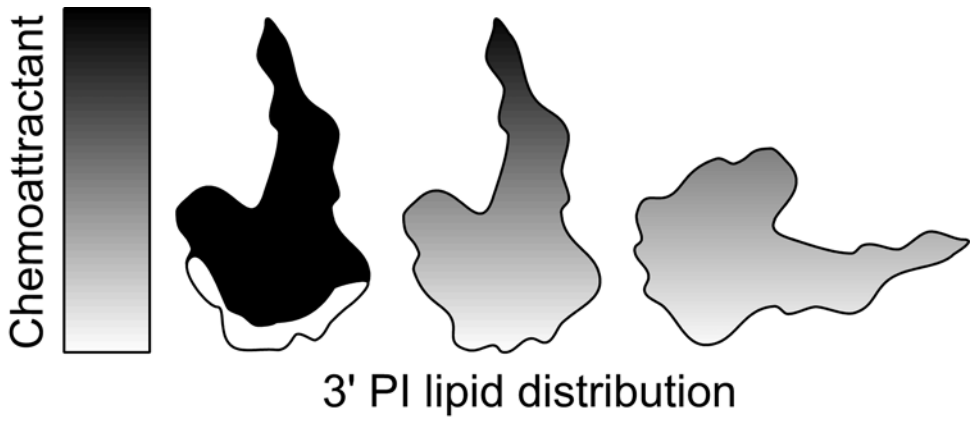

Figure 1.2 A chemoattractant gradient is shown on the left and cells in different orientations with respect to the gradient are shown. The cell on the left shows a sharp intracellular signaling gradient (amplification). This could be due to the fact that this cell is morphologically polarized in the direction of the gradient. The cell in the middle shows a shallow gradient and less of a contribution of polarization to the overall signaling. The cell on the right is oriented 90º and thus has a smaller gradient in intracellular signaling across its membrane.

Cell migration on a two-dimensional substrate occurs in three basic steps. First, a lamellipod extends and adhesions form between the ventral surface of the cell and the substrate. Lamellipodia are broad, thin membrane structures that extend preferentially from the cell and are formed as a result of force applied by the actin network on the inner leaflet of the plasma membrane. This actin network is spatially controlled (Pollard and Borisy 2003) through modulation of actin modifying proteins such as Arp2/3 (Nicholson-Dykstra and others 2005), ADF/cofilin (Bamburg 1999; DesMarais and others 2005) and formins (Watanabe and Higashida 2004). Signaling molecules such as small GTPases of the Rho family (Cdc42 and Rac) are believed to regulate these actin modifying proteins thus connecting receptor mediated events and PI 3-kinase signaling with actin network modification (Ridley 2001). Also, there has been work suggesting that 3' PI lipids can circumvent the Rho family GTPases and directly activate WAVE, a regulator of the Arp2/3 complex (Oikawa and others 2004). After lamellipod extension, the nucleus and cell body are pulled towards the front of the cell through a myosin-dependent contraction of the actin network. The traction needed for this process is achieved by mechanically linking the actin network to the substrate via the adhesions that are formed in the front of the cell (Lauffenburger and Horwitz 1996; Ridley and others 2003). Finally adhesions from the back of the cell detach and the uropod retracts, starting the cycle anew.

While spatial sensing is crucial in order to bias the direction of migration, there is another mechanism working to influence this biased direction. That mechanism is cell polarization (Devreotes and Janetopoulos 2003; Manahan and others 2004). When cells migrate there is a tendency to localize certain molecules in specific places; two such places that exemplify this are the leading edge and the trailing tail of the cell. This segregation of molecules is called cell polarization and this polarization is generally described as being oriented in a given direction. The spatial segregation of molecules limits the change in direction of the leading edge if the kinetics of the rearrangement is slow. Therefore, if these segregated molecules directly influence the signaling coming from the spatial sensing mechanism then polarization can be thought of as an intrinsic signal that must be integrated along with the spatial sensing signal in order for the cell to pick a direction in which to

migrate (fig. 1.2). This sets up an interesting situation where polarization may enhance or inhibit a cell's ability to sense extracellular gradients depending on the orientation of the cell in a given gradient. Consequently, it is important to understand how the intrinsic signaling of cell polarization is integrated along with spatial sensing.

The key to spatial sensing is the localization of a signaling molecule induced by differential ligand concentrations between the front and back of the cell, implicating the diffusion coefficient and lifetime of these signaling molecules as important parameters. In fibroblasts the molecules thought to hold this spatial information are 3' PI lipids, primarily because of their slow diffusion relative to turnover. Diffusion in the membrane ($D \sim 1$ $\mu m^2/s$) (Haugh and others 2000) of the cell is much slower than that in the cytosol ($D \sim 100$ $\mu m^2/s$) (Yokoe and Meyer 1996), so it compelling that 3' PI lipid second messengers could provide a means for the cell to hold spatial information in the membrane. Contact areas of fibroblasts are ~1000 μm^2. For a lifetime of ~100 s the search area for membrane lipids is only ~ 100 μm^2, whereas the search area for cytosolic molecules is ~10,000 μm^2.

1.3.2 Chemotaxis in traditional models of Dictyostelium discoideum and neutrophils

The PDGF-fibroblast system is just one of many different chemotaxis systems that have been examined. Two more common models in chemotaxis research are *D. discoideum*, a soil slime mold, and neutrophils, a type of white blood cell . These two cell models have been well-characterized due to their dramatic chemotactic responses to stimuli and rapid migration (Chung and others 2001; Devreotes and Zigmond 1988; Rickert and others 2000). *D. discoideum* is a single celled organism that primarily utilizes chemotaxis to aggregate upon starvation. Starved *D. discoideum* cells release cyclic AMP (cAMP), which attracts other *D. discoideum* in order to produce an aggregated multicellular slug or mound. Neutrophils use chemotaxis to sense the formyl peptides produced by bacteria. This enables them to eliminate harmful pathogens, especially during the early stages of wound healing. Consequently, the environment that these cells live in require that they migrate quickly and sense gradients dynamically.

It appears that PI 3-kinase is also important in *D. discoideum* and neutrophil chemotaxis (Merlot and Firtel 2003; Wang and others 2002). Inhibiting PI 3-kinase-γ as well

as knocking out the PI 3-kinase-γ gene produces cells with dramatically decreased chemotactic responses (Hirsch and others 2000; Li and others 2000; Sasaki and others 2000). Recently, PTEN, which antagonizes PI 3-kinase activity by dephosphorylating 3' PI lipids, has been shown to adversely affect chemotaxis. Overexpression of PTEN negatively impacts chemotaxis by abolishing the cell's ability to spatially sense extracellular gradients (Funamoto and others 2002; Iijima and Devreotes 2002). While phenotypic responses to gene perturbations are important, more work is being done to elucidate the mechanism by which the extracellular gradient in chemoattractant is transduced into an intracellular signaling gradient. Most of this research has taken advantage of fluorescently labeled PH domains as probes of local 3' PI lipid concentration. Several key features of PI 3-kinase signaling have emerged from this research.

First, stimulating *D. discoideum* and neutrophils with a uniform dose of chemoattractant produces a transient PI 3-kinase response that decays over the order of 1 minute as measured by PH domain translocation (Parent and others 1998; Servant and others 1999). Second, the accumulation of 3' PI lipids in the membrane of *D. discoideum* and neutrophils allow for sensing an extracellular chemoattractant gradient as shallow as 2% (Devreotes and Zigmond 1988). Obviously, this requires some sort of amplification of the biochemical signal between the chemoattractant stimulant and the actin polymerization response, which leads to membrane protrusion. This amplification was found to occur at the level of PIP3, underlying the importance of PI 3-kinase and PIP3 in spatial sensing for these cell types (Janetopoulos and others 2004; Jin and others 2000; Meili and others 1999; Parent and others 1998; Servant and others 2000; Servant and others 1999; Wang and others 2002). In neutrophils this amplification may in fact be mediated by Rac, which acts both upstream and downstream of PI 3-kinase and is required for chemoattractant stimulated PI 3-kinase activity (Servant and others 2000; Srinivasan and others 2003; Wang and others 2002). Third, *D. discoideum* in particular is not sensitive to the midpoint chemoattractant concentration, but only to the relative gradient. This has the effect of producing an all or none spatial sensing response after exposure to a gradients over many logs of average chemoattractant concentration (Janetopoulos and others 2004). Finally, these cells can respond at the level of PI 3-kinase to rapidly changing directions of the chemoattractant

gradient, allowing for a rapid change in migration direction (Parent and others 1998; Servant and others 2000). These observations would drive the development of several mathematical models of eukaryotic chemotaxis in the coming years.

1.3.3 Mathematical models of spatial sensing

A group of models were devised in order to explain the qualitative experimental observations outlined above, primarily that 1) The PI 3-kinase response in *D. discoideum* and neutrophils adapts on short timescales after uniform doses of chemoattractant. 2) These cells are sensitive to the relative gradient of chemoattractant at the level of PI 3-kinase signaling, but not the midpoint chemoattractant concentration. This sensitivity occurs even at very low relative gradients of chemoattractant (~2%). 3) *D. discoideum* and neutrophils are able to quickly change the intracellular signaling to follow changing directions of the external chemoattractant gradients.

From these observations came the necessity to invoke mathematical constructs such as positive/negative feedback (Meinhardt 1999; Narang and others 2001; Subramanian and Narang 2004), activator depletion (Postma and Van Haastert 2001) and/or receptor mediated local excitation and global inhibition (Janetopoulos and others 2004; Levchenko and Iglesias 2002; Ma and others 2004) in order to explain the conversion of the extracellular gradient into an intracellular signaling gradient. Models that contained positive feedback loops could predict the observed degree of amplification, but lacked the ability to change with changing extracellular gradients, producing cells that were essentially stuck with a given intracellular signaling profile. Artificial long timescale degradation of the signaling needed to be included in these models to poison the positive feedback loop and allow the cell to regain sensitivity to the extracellular gradient (Meinhardt 1999). On the other hand, models containing activator depletion were not good at predicting the high amplification of the signal. With refinement of the local excitation/global inhibition model came a reasonably good explanation of the spatial sensing response of *D. discoideum*. This allowed researchers to directly compare results from this reaction-diffusion model to experimental imaging results obtained using fluorescently labeled PH domains (Janetopoulos and others 2004; Ma and others 2004).

1.4 APPROACH

We believe this direct comparison of live-cell fluorescence imaging experiments to reaction-diffusion models provides a powerful means to understand the underlying mechanisms of spatial sensing. Consequently, we have developed a spatial sensing model that can be directly compared to imaging data. By stimulating fibroblasts expressing GFP-AktPH with both uniform and gradient doses of PDGF we can follow the spatial distribution of 3' PI lipids in time.

The primary technique used in this study is called total internal reflection fluorescence (TIRF) microscopy or evanescent wave microscopy (Axelrod 2001; Schneckenburger 2005; Steyer and Almers 2001; Toomre and Manstein 2001). TIRF microscopy was developed by Dan Axelrod in the early eighties as a way to image membrane-substratum separation (Axelrod 1989), and interest in this technique has been revived with the ability to tag proteins with GFP. TIRF microscopy involves producing an evanescent wave that propagates normal to the surface of reflection (fig. 1.3). An evanescent wave results when the angle of reflection, θ, is greater than the critical angle, θ_c. The intensity, I of the evanescent wave is a function that decays exponentially from the point of reflection (Eqn. 1.1).

$$I = I_0 e^{-d/z}$$
$$d = \frac{\lambda}{4\pi\sqrt{n_1^{\,2}\sin\theta^2 - n_2^{\,2}}} \qquad (1.1)$$

The exponential decay of the wave is advantageous because it allows for the selective excitation of fluorophores close to the point of reflection i.e., close to the surface of the cell contact area. Consequently, only ~5% of the intensity remains after ~270 nm (θ = 68°, n_1 = 1.51, n_2 = 1.33, λ = 488nm). Cell-surface separation distances are ~10-100 nm, membrane thicknesses are ~10 nm and total cell heights are ~1000 nm. Consequently, there is anywhere from 30% to 90% of the wave intensity exciting the fluorophores close to the inner leaflet of the membrane, leaving most (>70%) of the cytosol unexcited.

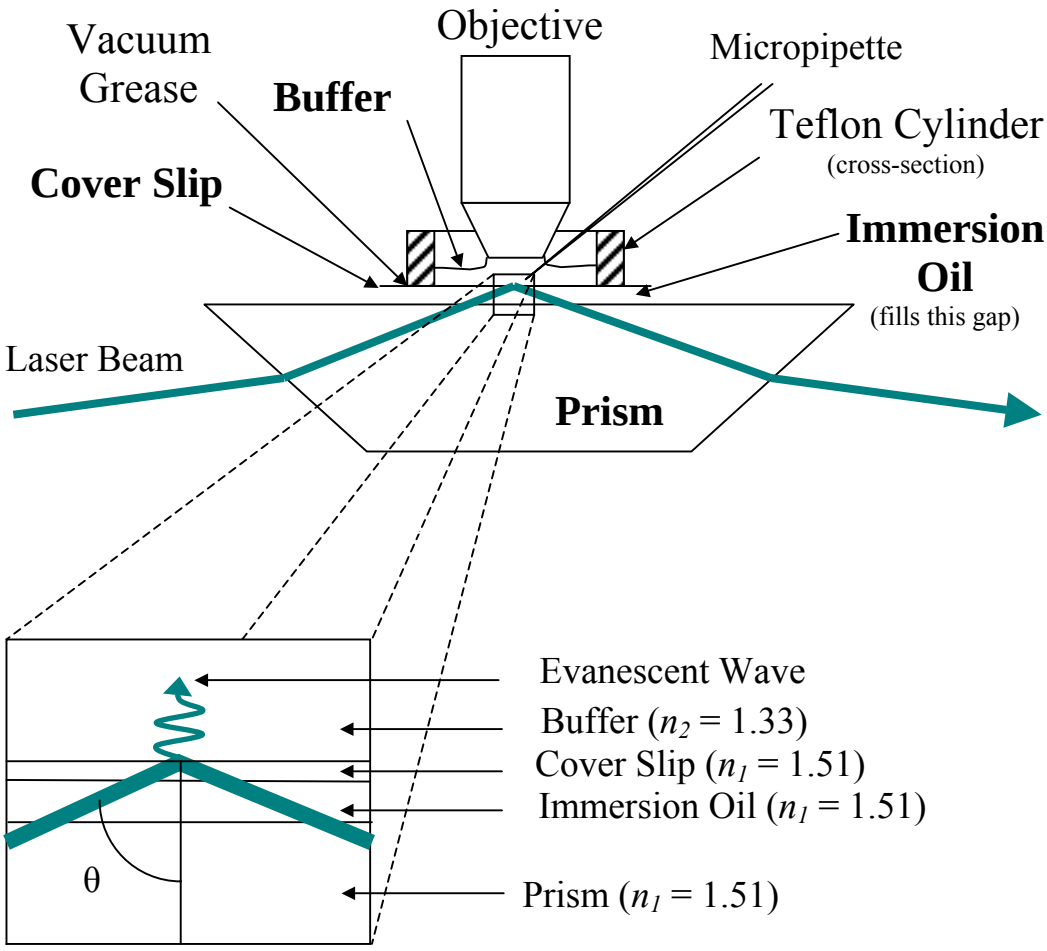

Figure 1.3: **TIRF microscope set-up-** The objective is optically linked to a conventional microscope. A charged coupled device (CCD) is mounted on the microscope to capture images and send them to the data acquisition software. The micropipette is used to deliver PDGF to the buffer solution in the gradient experiments described in Chapter 5.

This selective excitation gives another important advantage to TIRF microscopy when using fluorescently labeled PH domains. Confocal microscopy, which illuminates the entire sample and selectively focuses on a section of the sample, is prone to probe photobleaching. TIRF microscopy illuminates only fluorophores close to the surface, allowing for "fresh" non-bleached probe to diffuse into the region, bind to the membrane and replace bleached fluorophores.

The properties of TIRF microscopy allow one to obtain quantitative fluorescence images of the translocation of the PH domain probe in space and time. Using a reaction-diffusion model that incorporates the membrane processes of 3' PI production, diffusion and degradation as well as the binding characteristics of the AktPH probe allows for direct comparison of the model to fluorescence imaging experiments. We then hope to address several questions associated with spatial sensing in fibroblasts:

1. How sensitive are the parameters that determine 3' PI production, diffusion and turnover to actual fluorescence measurements in cells? (Chapter 2)
2. What are the ranges of the diffusion coefficient and turnover rate constant for 3' PIs in the membrane? (Chapter 3 and 4)
3. It is known that PI 3-kinase is regulated by PDGF receptor activation, but is the turnover of 3' PIs receptor-regulated? (Chapter 3)
4. During uniform receptor activation, is the production, diffusion and degradation of 3' PIs spatially controlled in the membrane, and if so, can this be linked to cell polarization? (Chapter 4)
5. Is the spatial sensing mechanism of fibroblasts the same as in *D. discoideum* and neutrophils? If this mechanism is different, then how does it depend on the relative PDGF gradient and the midpoint PDGF concentration? (Chapter 5)

1.5 REFERENCES

Anand-Apte B, Zetter BR, Viswanathan A, Qiu RG, Chen J, Ruggieri R, Symons M. 1997. Platelet-derived growth factor and fibronectin-stimulated migration are differentially regulated by the Rac and extracellular signal-regulated kinase pathways. J. Biol. Chem. 272(49):30688-30692.

Axelrod D. 1989. Total Internal-Reflection Fluorescence Microscopy. Methods in Cell Biology 30:245-270.

Axelrod D. 2001. Total internal reflection fluorescence microscopy in cell biology. 2(11):764-774.

Bamburg JR. 1999. Proteins of the ADF/cofilin family: Essential regulators of actin dynamics. Annual Review of Cell and Developmental Biology 15:185-230.

Berg HC. 1978. Bacterial Chemotaxis. Biophysical Journal 21(3):A29-A29.

Berg HC, Brown DA. 1972. Chemotaxis in Escherichia-Coli Analyzed by 3-Dimensional Tracking. Nature 239(5374):500-&.

Block SM, Segall JE, Berg HC. 1982. Impulse Responses in Bacterial Chemotaxis. Cell 31(1):215-226.

Block SM, Segall JE, Berg HC. 1983. Adaptation Kinetics in Bacterial Chemotaxis. Journal of Bacteriology 154(1):312-323.

Blomberg N, Baraldi E, Nilges M, Saraste M. 1999. The PH superfold: a structural scaffold for multiple functions. Trends in Biochemical Sciences 24(11):441-445.

Chung CY, Funamoto S, Firtel RA. 2001. Signaling pathways controlling cell polarity and chemotaxis. Trends Biochem.Sci. 26(9):557-566.

Clark RAF. 1996. The Molecular and Cellular Biology of Wound Repair. Clark RAF, editor: Plenum Press.

DesMarais V, Ghosh M, Eddy R, Condeelis J. 2005. Cofilin takes the lead. Journal of Cell Science 118(1):19-26.

Deuel TF, Kawahara RS, Mustoe TA, Pierce GF. 1991. Growth-Factors and Wound-Healing - Platelet-Derived Growth- Factor as a Model Cytokine. Annu. Rev. Med. 42:567-584.

Devreotes P, Janetopoulos C. 2003. Eukaryotic chemotaxis: Distinctions between directional sensing and polarization. Journal of Biological Chemistry 278(23):20445-20448.

Devreotes PN, Zigmond SH. 1988. Chemotaxis in Eukaryotic Cells - a Focus on Leukocytes and Dictyostelium. Annu. Rev. Cell Biol. 4:649-686.

Frech M, Andjelkovic M, Ingley E, Reddy KK, Falck JR, Hemmings BA. 1997. High affinity binding of inositol phosphates and phosphoinositides to the Pleckstrin homology domain of RAC protein kinase B and their influence on kinase activity. Journal of Biological Chemistry 272(13):8474-8481.

Funamoto S, Meili R, Lee S, Parry L, Firtel RA. 2002. Spatial and temporal regulation of 3-phosphoinositides by PI 3- kinase and PTEN mediates chemotaxis. Cell 109(5):611-623.

Grotendorst GR, Igarashi A, Larson R, Soma Y, Charette M. 1991. Differential Binding, Biological and Biochemical Actions of Recombinant Pdgf Aa, Ab, and Bb Molecules on Connective-Tissue Cells. Journal of Cellular Physiology 149(2):235-243.

Haugh JM, Codazzi F, Teruel M, Meyer T. 2000. Spatial sensing in fibroblasts mediated by 3 ' phosphoinositides. J. Cell Biol. 151(6):1269-1279.

Hawkins PT, Welch H, McGregor A, Eguinoa A, Gobert S, Krugmann S, Anderson K, Stokoe D, Stephens L. 1997. Signalling via phosphoinositide 3OH kinases. Biochem. Soc. Trans. 25(4):1147-1151.

Heldin CH, Westermark B. 1999. Mechanism of action and in vivo role of platelet-derived growth factor. Physiol. Rev. 79(4):1283-1316.

Hirsch E, Katanaev VL, Garlanda C, Azzolino O, Pirola L, Silengo L, Sozzani S, Mantovani A, Altruda F, Wymann MP. 2000. Central role for G protein-coupled phosphoinositide 3-kinase gamma in inflammation. Science 287(5455):1049-1053.

Hooshmand-Rad R, ClaessonWelsh L, Wennstrom S, Yokote K, Siegbahn A, Heldin CH. 1997. Involvement of phosphatidylinositide 3'-kinase and Rac in platelet-derived growth factor-induced actin reorganization and chemotaxis. Experimental Cell Research 234(2):434-441.

Iijima M, Devreotes P. 2002. Tumor suppressor PTEN mediates sensing of chemoattractant gradients. Cell 109(5):599-610.

Iijima M, Huang YE, Luo HR, Vazquez F, Devreotes PN. 2004. Novel mechanism of PTEN regulation by its phosphatidylinositol 4,5-bisphosphate binding motif is critical for chemotaxis. Journal of Biological Chemistry 279(16):16606-16613.

Janetopoulos C, Ma L, Devreotes PN, Iglesias PA. 2004. Chemoattractant-induced phosphatidylinositol 3,4,5-trisphosphate accumulation is spatially amplified and adapts, independent of the actin cytoskeleton. 101(24):8951-8956.
Jin T, Zhang N, Long Y, Parent CA, Devreotes PN. 2000. Localization of the G protein beta gamma complex in living cells during chemotaxis. Science 287(5455):1034-1036.
Kontos CD, Stauffer TP, Yang WP, York JD, Huang LW, Blanar MA, Meyer T, Peters KG. 1998. Tyrosine 1101 of Tie2 is the major site of association of p85 and is required for activation of phosphatidylinositol 3-kinase and Akt. Molecular and Cellular Biology 18(7):4131-4140.
Kundra V, Escobedo JA, Kazlauskas A, Kim HK, Rhee SG, Williams LT, Zetter BR. 1994. Regulation of Chemotaxis by the Platelet-Derived Growth-Factor Receptor-Beta. Nature 367(6462):474-476.
Lacalle RA, Gomez-Mouton C, Barber DF, Jimenez-Baranda S, Mira E, Martinez C, Carrera AC, Manes S. 2004. PTEN regulates motility but not directionality during leukocyte chemotaxis. Journal of Cell Science 117(25):6207-6215.
Lauffenburger DA, Horwitz AF. 1996. Cell migration: A physically integrated molecular process. Cell 84(3):359-369.
Lemmon MA, Ferguson KM, Abrams CS. 2002. Pleckstrin homology domains and the cytoskeleton. Febs Letters 513(1):71-76.
Lemmon MA, Ferguson KM, Schlessinger J. 1996. PH domains: Diverse sequences with a common fold recruit signaling molecules to the cell surface. Cell 85(5):621-624.
Leslie NR, Downes CP. 2004. PTEN function: how normal cells control it and tumour cells lose it. Biochemical Journal 382:1-11.
Levchenko A, Iglesias PA. 2002. Models of eukaryotic gradient sensing: Application to chemotaxis of amoebae and neutrophils. Biophysical Journal 82(1):50-63.
Li Z, Dong XM, Wang ZL, Liu WZ, Deng N, Ding Y, Tang LY, Hla T, Zeng R, Li L and others. 2005. Regulation of PTEN by Rho small GTPases. Nature Cell Biology 7(4):399-U42.
Li Z, Hannigan M, Mo ZC, Liu B, Lu W, Wu Y, Smrcka AV, Wu GQ, Li L, Liu MY and others. 2003. Directional sensing requires G beta gamma-mediated PAK1 and PIX alpha-dependent activation of cdc42. Cell 114(2):215-227.
Li Z, Jiang HP, Xie W, Zhang ZC, Smrcka AV, Wu DQ. 2000. Roles of PLC-beta 2 and -beta 3 and PI3K gamma in chemoattractant-mediated signal transduction. Science 287(5455):1046-1049.
Ma L, Janetopoulos C, Yang L, Devreotes PN, Iglesias PA. 2004. Two complementary, local excitation, global inhibition mechanisms acting in parallel can explain the chemoattractant-induced regulation of PI(3,4,5)P-3 response in Dictyostelium cells. 87(6):3764-3774.
Manahan CL, Iglesias PA, Long Y, Devreotes PN. 2004. Chemoattractant signaling in Dictyostelium discoideum. 20:223-253.
Marshall JG, Booth JW, Stambolic V, Mak T, Balla T, Schreiber AD, Meyer T, Grinstein S. 2001. Restricted accumulation of phosphatidylinositol 3-kinase products in a plasmalemmal subdomain during Fc gamma receptor- mediated phagocytosis. Journal of Cell Biology 153(7):1369-1380.
Martin P. 1997. Wound healing - Aiming for perfect skin regeneration. Science 276(5309):75-81.
Meili R, Ellsworth C, Lee S, Reddy TBK, Ma H, Firtel RA. 1999. Chemoattractant-mediated transient activation and membrane localization of Akt/PKB is required for efficient chemotaxis to cAMP in Dictyostelium. Embo J. 18(8):2092-2105.
Meinhardt H. 1999. Orientation of chemotactic cells and growth cones: models and mechanisms. Journal of Cell Science 112(17):2867-2874.
Merlot S, Firtel RA. 2003. Leading the way: directional sensing through phosphatidylinositol 3-kinase and other signaling pathways. Journal of Cell Science 116(17):3471-3478.
Narang A, Subramanian KK, Lauffenburger DA. 2001. A mathematical model for chemoattractant gradient sensing based on receptor-regulated membrane phospholipid signaling dynamics. Ann. Biomed. Eng. 29(8):677-691.
Nicholson-Dykstra S, Higgs HN, Harris ES. 2005. Actin dynamics: Growth from dendritic branches. Current Biology 15(9):R346-R357.
Oikawa T, Yamaguchi H, Itoh T, Kato M, Ijuin T, Yamazaki D, Suetsugu S, Takenawa T. 2004. PtdIns(3,4,5)P-3 binding is necessary for WAVE2-induced formation of lamellipodia. 6(5):420-+.

Ostman A, Thyberg, B., Westermark, B., and Heldin, C.H. 1989. Expression of three recombinant homodimeric isoforms of PDGF in Saccharomyces cerevisiae: evidence for difference in receptor binding and functional activities. Growth Factors 1:271-281.
Parent CA, Blacklock BJ, Froehlich WM, Murphy DB, Devreotes PN. 1998. G protein signaling events are activated at the leading edge of chemotactic cells. Cell 95(1):81-91.
Pierce GF, Mustoe TA, Altrock BW, Deuel TF, Thomason A. 1991. Role of Platelet-Derived Growth-Factor in Wound-Healing. Journal of Cellular Biochemistry 45(4):319-326.
Pierce GF, Mustoe TA, Lingelbach J, Masakowski VR, Griffin GL, Senior RM, Deuel TF. 1989. Platelet-Derived Growth-Factor and Transforming Growth Factor- Beta Enhance Tissue-Repair Activities by Unique Mechanisms. J. Cell Biol. 109(1):429-440.
Pollard TD, Borisy GG. 2003. Cellular motility driven by assembly and disassembly of actin filaments. 112(4):453-465.
Postma M, Van Haastert PJM. 2001. A diffusion-translocation model for gradient sensing by chemotactic cells. Biophysical Journal 81(3):1314-1323.
Rameh LE, Cantley LC. 1999. The role of phosphoinositide 3-kinase lipid products in cell function. Journal of Biological Chemistry 274(13):8347-8350.
Rickert P, Weiner OD, Wang F, Bourne HR, Servant G. 2000. Leukocytes navigate by compass: roles of PI3K gamma and its lipid products. Trends Cell Biol. 10(11):466-473.
Ridley AJ. 2001. Rho GTPases and cell migration. Journal of Cell Science 114(15):2713-2722.
Ridley AJ, Paterson HF, Johnston CL, Diekmann D, Hall A. 1992. The Small Gtp-Binding Protein Rac Regulates Growth-Factor Induced Membrane Ruffling. Cell 70(3):401-410.
Ridley AJ, Schwartz MA, Burridge K, Firtel RA, Ginsberg MH, Borisy G, Parsons JT, Horwitz AR. 2003. Cell migration: Integrating signals from front to back. 302(5651):1704-1709.
Sasaki T, Irie-Sasaki J, Jones RG, Oliveira-dos-Santos AJ, Stanford WL, Bolon B, Wakeham A, Itie A, Bouchard D, Kozieradzki I and others. 2000. Function of PI3K gamma in thymocyte development, T cell activation, and neutrophil migration. Science 287(5455):1040-1046.
Schlessinger J. 2000. Cell signaling by receptor tyrosine kinases. Cell 103(2):211-225.
Schneckenburger H. 2005. Total internal reflection fluorescence microscopy: technical innovations and novel applications. 16(1):13-18.
Servant G, Weiner OD, Herzmark P, Balla T, Sedat JW, Bourne HR. 2000. Polarization of chemoattractant receptor signaling during neutrophil chemotaxis. Science 287(5455):1037-1040.
Servant G, Weiner OD, Neptune ER, Sedat JW, Bourne HR. 1999. Dynamics of a chemoattractant receptor in living neutrophils during chemotaxis. Mol. Biol. Cell 10(4):1163-1178.
Shaw G. 1996. The pleckstrin homology domain: An intriguing multifunctional protein module. Bioessays 18(1):35-46.
Srinivasan S, Wang F, Glavas S, Ott A, Hofmann F, Aktories K, Kalman D, Bourne HR. 2003. Rac and Cdc42 play distinct roles in regulating PI(3,4,5)P-3 and polarity during neutrophil chemotaxis. Journal of Cell Biology 160(3):375-385.
Steyer JA, Almers W. 2001. A real-time view of life within 100 nm of the plasma membrane. 2(4):268-275.
Subramanian KK, Narang A. 2004. A mechanistic model for eukaryotic gradient sensing: Spontaneous and induced phosphoinositide polarization. 231(1):49-67.
Tamura M, Gu JG, Tran H, Yamada KM. 1999. PTEN gene and integrin signaling in cancer. J. Natl. Cancer Inst. 91(21):1820-1828.
Toomre D, Manstein DJ. 2001. Lighting up the cell surface with evanescent wave microscopy. 11(7):298-303.
Vandergeer P, Hunter T, Lindberg RA. 1994. Receptor Protein-Tyrosine Kinases and Their Signal-Transduction Pathways. Annual Review of Cell Biology 10:251-337.
Vanhaesebroeck B, Waterfield MD. 1999. Signaling by distinct classes of phosphoinositide 3-kinases. Experimental Cell Research 253(1):239-254.
Wang F, Herzmark P, Weiner OD, Srinivasan S, Servant G, Bourne HR. 2002. Lipid products of PI(3)Ks maintain persistent cell polarity and directed motility in neutrophils. Nat. Cell Biol. 4(7):513-518.
Watanabe N, Higashida C. 2004. Formins: processive cappers of growing actin filaments. Experimental Cell Research 301(1):16-22.
Welch HCE, Coadwell WJ, Stephens LR, Hawkins PT. 2003. Phosphoinositide 3-kinase-dependent activation of Rac. 546(1):93-97.

Wennstrom S, Hawkins P, Cooke F, Hara K, Yonezawa K, Kasuga M, Jackson T, Claessonwelsh L, Stephens L. 1994a. Activation of Phosphoinositide 3-Kinase Is Required for Pdgf- Stimulated Membrane Ruffling. Curr. Biol. 4(5):385-393.

Wennstrom S, Siegbahn A, Yokote K, Arvidsson AK, Heldin CH, Mori S, Claessonwelsh L. 1994b. Membrane Ruffling and Chemotaxis Transduced by the Pdgf Beta- Receptor Require the Binding-Site for Phosphatidylinositol 3' Kinase. Oncogene 9(2):651-660.

Westermark B, Sorg C. 1993. Biology of Platelet-Derived Growth Factor. Sorg CM, editor. Basel: New York: S. Karger AG. 1-163 p.

Wymann M, Arcaro A. 1994. Platelet-Derived Growth Factor-Induced Phosphatidylinositol 3- Kinase Activation Mediates Actin Rearrangements in Fibroblasts. Biochemical Journal 298:517-520.

Wymann MP, Pirola L. 1998. Structure and function of phosphoinositide 3-kinases. 1436(1-2):127-150.

Xu JS, Wang F, Van Keymeulen A, Herzmark P, Straight A, Kelly K, Takuwa Y, Sugimoto N, Mitchison T, Bourne HR. 2003. Divergent signals and cytoskeletal assemblies regulate self-organizing polarity in neutrophils. Cell 114(2):201-214.

Yokoe H, Meyer T. 1996. Spatial dynamics of GFP-tagged proteins investigated by local fluorescence enhancement. 14(10):1252-1256.

Chapter 2

Spatial Analysis of 3' Phosphoinositide Signaling in Living Fibroblasts: I. Uniform Stimulation Model and Bounds on Dimensionless Groups

Adapted from Haugh and Schneider, Biophys. J., 86: 589-598 (2004)

2.1 ABSTRACT

Fluorescent protein probes now permit spatial distributions of specific intracellular signaling molecules to be observed in real time. Mathematical models have been used to simulate molecular gradients and other spatial patterns within cells, and the output of such models may be compared directly with experiments if the binding of the fluorescent probe and the physics of the imaging technique are each incorporated. A comprehensive model describing the dynamics of 3' phosphoinositides (PIs), lipid second messengers produced in the plasma membrane in response to stimulation of the PI 3-kinase signaling pathway, as monitored in the cell-substratum contact area using total internal reflection fluorescence (TIRF) microscopy is presented here. With this technique it was previously shown that uniform stimulation of fibroblasts with platelet-derived growth factor (PDGF) elicits the formation of axisymmetric 3' PI gradients, which are now characterized in the context of this model. We find that upper and lower bounds on the relevant dimensionless model parameter values for an individual cell can be calculated from four well-defined fluorescence measurements. Based on our analysis we expect that the key dimensionless group, the ratio of 3' PI turnover and diffusion rates, can be estimated within ~ 20% or less.

2.2 INTRODUCTION

Cells in multicellular organisms must co-exist, and thus their behaviors are tightly regulated through inter- and intracellular signaling mechanisms. Although our knowledge of the complex biochemical interactions used by cells to process information has rapidly expanded (Hunter, 2000), the integration of these molecular level details into a holistic framework is now presenting a significant challenge. A tool that has shown promise in the synthesis and analysis of signal transduction networks is mathematical modeling (Weng et al., 1999; Asthagiri and Lauffenburger, 2000). Most of the signaling models offered to date have been of the kinetic variety, comprised of deterministic, ordinary differential equations (ODEs) in which the amounts of molecular species in various states change with respect to time only. Such models are appropriate for comparison with cell biochemical experiments, in which a large number of cells are homogenized and analyzed. Although these methods can be quantitative and are appropriate for determining population averages, it must be acknowledged that the concentrations of signaling components certainly vary from cell to cell, and that the kinetics of individual cell responses may be asynchronous and/or noisy.

Another aspect of cell signaling that is not adequately addressed in either ODE kinetic models or cell biochemical experiments is the spatial distribution of the intracellular species. Although kinetic models can effectively model exchange of signaling molecules between intracellular locations and compartments (Haugh and Lauffenburger, 1998; Xu et al., 2003), this approach does not lend itself to the description of spatial gradients in molecular concentration, which can form through production of molecules at localized intracellular sites. In such cases, partial differential equations (PDEs) can be formulated in spatial dimensions as well as time, and thus molecular transport mechanisms can be modeled explicitly. Computational approaches for the efficient simulation of three-dimensional spatial patterns within the cytosol have been conceived and used to compare models with spatially resolved fluorescence imaging experiments (Schaff et al., 1997; Fink et al., 1999).

Two-dimensional molecular gradients in cell membranes are also relevant in signal transduction. Most signaling pathways involve specific membrane-associated intermediates that are produced or activated through recruitment of signaling enzymes to the plasma

membrane. Gradients in the density of specific membrane lipids or activated lipid-anchored proteins may form on the scale of nanometers if the rates of the reactions that produce them are rapid enough to be limited by lateral diffusion (Shea et al., 1997; Haugh, 2002), while gradients on longer length scales can form when the extracellular stimulus is spatially confined or otherwise organized. A prominent example is the production of 3' phosphoinositide (PI) lipids through activation of the intracellular enzyme PI 3-kinase (Vanhaesebroeck et al., 2001). One of the cellular functions of 3' PI lipids is to influence cell adhesion, spreading, and motility through remodeling of the actin cytoskeleton (Rameh and Cantley, 1999), and thus the localization of 3' PI production is critical for cell guidance (Weiner, 2002). Localization can be induced by gradients of soluble factors or extracellular matrix components, or by cellular interactions with other cells or particles, and such systems lend themselves to PDE modeling (Narang et al., 2001; Postma and Van Haastert, 2001; Levchenko and Iglesias, 2002; Pribyl et al., 2003) and fluorescence microscopy techniques (Parent and Devreotes, 1999; Botelho et al., 2000; Marshall et al., 2001; Harriague and Bismuth, 2002; Wang et al., 2002). However, no studies have yet successfully integrated modeling and experiments of lipid second messenger signaling, to the extent of a quantitative and direct comparison with respect to space as well as time.

Even when cell stimulation is spatially uniform, intracellular gradients can form if activation of cell surface receptors is confined to certain regions of the plasma membrane. Indeed, in previous work using an enhanced green fluorescent protein fusion probe (GFP-AktPH) and high-resolution total internal reflection fluorescence (TIRF) microscopy, it was found that two kinds of 3' PI lipid gradients can form in the membrane-substratum contact area of platelet-derived growth factor (PDGF)-stimulated fibroblasts. In the presence of a PDGF gradient, 3' PI production is polarized towards the highest PDGF concentration, while uniform PDGF stimulation yields a radial 3' PI gradient, presumably through the restriction of PDGF-stimulated PI 3-kinase activation to the nonadherent portion of the membrane (Haugh et al., 2000). In either case, the ability to maintain a second messenger gradient within a cell of given dimensions depends on the relative rates of turnover, mediated by specific enzymatic activities, and molecular transport, typically dominated by diffusion.

In this work, we present a generalized mathematical model that describes the 3' PI dynamics in response to uniform stimulation. With appropriate assumptions, it is shown that the model can directly simulate TIRF intensity measurements in fibroblasts, and that the prominent features of these simulations are sensitive to the values of the dimensionless model parameters. Although the fluorescence characteristics of a cell do not correspond to a unique set of parameter values, upper and lower bounds on each of the parameters are defined by examining specific limiting cases of the model. Using this constraints-based approach we demonstrate that the primary parameter of interest, which compares the rates of 3' PI turnover and diffusion, can be estimated with reasonable precision from defined fluorescence measurements.

2.3 GENERALIZED UNIFORM STIMULATION MODEL

2.3.1 Axisymmetric reaction-diffusion model of 3' phosphoinositide dynamics

The geometry of the model cell is depicted in Figure 2.1. In this formulation of the model, the hemispherical top and circular bottom membrane domains of the model cell are allowed to have different rates of 3' PI generation, diffusion in two dimensions, and consumption by first order reaction(s) (Fig. 2.1a). The generalized conservation equation for the 3' PI number density X (#/μm2) in each domain i (bottom or top) is thus

$$\partial X_i / \partial t = D_i \nabla^2 X_i - k_i X_i + V_i(t) \qquad (2.1),$$

where t is time, D_i is the molecular diffusion coefficient, k_i the observed consumption rate constant, and $V_i(t)$ the generation rate of the second messenger in domain i. The kinetics of the latter depend on the assembly of ligand, receptor, and intracellular enzyme molecules. The symmetry of the problem is such that the 3' PI distribution in the bottom domain varies with radial position r only, and that of the top domain varies with azimuthal angle θ only (η = cos θ) (Fig. 2.1b). The interface joining the two domains ($r = R$ and η = 0) is subject to matching boundary conditions:

$$\begin{aligned} X_b(R,t) &= X_t(0,t) \\ D_b \nabla X_b(R,t) &= D_t \nabla X_t(0,t) \end{aligned} \qquad (2.2).$$

Additionally, $X_b(r,t)$ and $X_t(\eta,t)$ must be finite. Our solution employs the following dimensionless variables and parameters:

$$\begin{aligned} &x_i \equiv \frac{X_i}{X^*}; \quad \tau \equiv k_b t; \quad \rho \equiv \frac{r}{R}; \quad \upsilon_i(\tau) \equiv \frac{V_i(t)}{k_i X^*}; \\ &Da \equiv \frac{k_b R^2}{D_b}; \quad \alpha \equiv \frac{k_t}{k_b}; \quad \gamma \equiv \frac{D_t}{D_b}; \quad \nu \equiv \frac{V_{t,SS} k_b}{V_{b,SS} k_t}; \end{aligned} \qquad (2.3),$$

where X^* is, for now, an arbitrary scaling quantity in units of number density, and $V_{t,ss}$ and $V_{b,ss}$ are the steady state values of $V_t(t)$ and $V_b(t)$, respectively. Perhaps the most important of the model parameters is the Damköhler number *Da*, which compares the rates of 3' PI consumption and diffusion in the bottom domain and thus controls the formation of 3' PI gradients there. The details of the solution and the calculation of $x_b(\rho,\tau)$ and $x_t(\eta,\tau)$ are given in Appendix A.

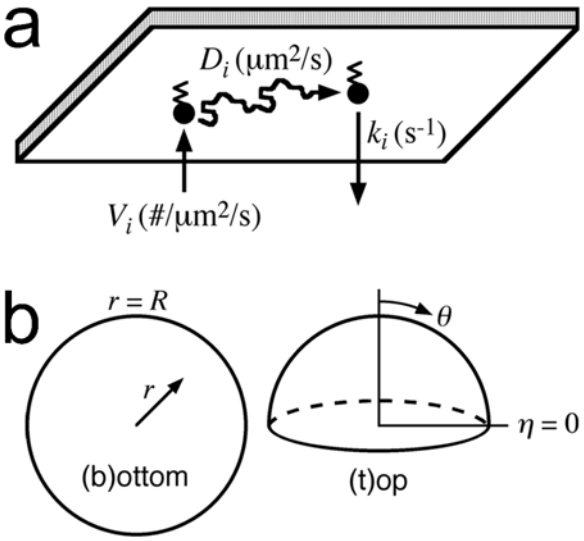

FIGURE 2.1 Generalized lipid second messenger model. (a) Within each membrane domain *i*, the lipid second messenger is inserted at random positions at a rate V_i. Once inserted, the lipid experiences lateral diffusion with effective diffusion coefficient D_i, and it is consumed with observed first order rate constant k_i. (b) Geometry and spatial coordinates of the two domains.

2.3.2 TIRF intensity profiles and simulation of association-dissociation experiments

A model of the 3' PI dynamics is not sufficient for comparison with experiments, because the spatial distribution of specific membrane lipids cannot be measured directly. Rather, the most common method is to use an intracellular fluorescent probe that binds specifically to 3' PIs, such as GFP-AktPH, which will translocate from the cytosol to the plasma membrane as the 3' PI level increases. The extent of probe translocation is then resolved by fluorescence microscopy, and thus the nature of the fluorescence intensity data depends on the imaging technique used. We focus our attention on the aforementioned TIRF microscopy technique, in which an evanescent wave selectively excites intracellular fluorophores in close proximity to the membrane-substratum contact area (Axelrod, 2001; Steyer and Almers, 2001; Toomre and Manstein, 2001). The fluorescence intensity is thus a

sum of contributions from membrane-bound probe and a small fraction of the unbound, cytosolic probe molecules.

We assume that the binding of a fluorescent probe to the membrane is in pseudo-equilibrium with free probe in the cytosol. Based on experiments in a macrophage cell line, it has been determined that it requires about 5 seconds for membrane-bound GFP-AktPH probe to exchange with the cytosolic pool (Marshall et al., 2001), significantly faster than the time scale of 3' PI turnover in fibroblasts or macrophages, ~ 1 minute (Haugh et al., 2000; Marshall et al., 2001). Distribution of GFP-AktPH within the cytosol is assumed to be similarly rapid, based on an intracellular diffusion coefficient for enhanced GFP of ca. 40 $\mu m^2/s$ (Yokoe and Meyer, 1996; Swaminathan et al., 1997) and a characteristic length scale of 10 μm. The normalized fluorescence intensity for TIRF excitation, $f(\rho,\tau)$, is then readily calculated from the 3' PI distributions, as described in Appendix B. Importantly, this quantity can be determined from fluorescence image data, allowing a direct comparison of model and experiment. To obtain $f(\rho,\tau)$, three dimensionless groups must be specified in addition to those listed in Equation 2.3:

$$\sigma \equiv \frac{V_{cyt}}{A_c d_{cell}}; \quad \kappa \equiv \frac{K_D V_{cyt}}{P_{Tot}}; \quad \mu \equiv \frac{A_c X^*}{P_{Tot}} \tag{2.4},$$

where V_{cyt} is the volume of the cytosol, A_c is the cell contact area ($A_c = \pi R^2$ for our model cell), d_{cell} is the effective penetration depth of the evanescent wave into the cell (~ 100 nm), K_D is the dissociation constant of the probe-3' PI interaction, and P_{Tot} is the total number of probe molecules in the cell. The fluorescence gain parameter σ is the fold increase in evanescent wave fluorescence observed when a probe molecule translocates from the cytosol to the contact area, and thus it is the only parameter that reflects the physics of the imaging technique. The other two parameters, along with the calculated number of 3' PI molecules in the cell, determine the extent of probe-3' PI binding. The fraction of the probe recruited to the plasma membrane is defined as $p(\tau)$, and its value at steady state, p_{ss}, can be specified in place of either κ or μ. The dimensionless model variables and parameters are summarized in Table 2.1.

TABLE 2.1 Dimensionless variables and parameters.

Variable	Definition	Description
ρ	r/R	Dimensionless radius, bottom domain
τ	$k_b t$	Dimensionless time
$x_b(\rho,\tau)$	$X_b(r,t)/X^*$	Lipid number density, bottom domain
$x_t(\eta,\tau)$	$X_t(\eta,t)/X^*$	Lipid number density, top domain
$f(\rho,\tau)$	$F(r,t)/F_{cyt}-1$	Dimensionless fluorescence intensity
$p(\tau)$		Fraction of fluorescent probe bound

Parameter	Definition	Description
Da	$k_b R^2/D_b$	Damköhler #; consumption vs. diffusion
α	k_t/k_b	Ratio of lipid consumption rate constants
γ	D_t/D_b	Ratio of lipid diffusion coefficients
ν	$V_{b,ss}k_t/V_{t,ss}k_b$	Ratio of steady state lipid insertion rates
σ	$V_{cyt}/A_c d_{cell}$	Fluorescence gain parameter
κ	$K_D V_{cyt}/P_{Tot}$	Dimensionless probe dissociation constant
μ	$A_c X^*/P_{Tot}$	Maximum ratio of lipid/probe molecules
x_0	$x_b(\rho,0)$	Pre-stimulus lipid density (constant)

We have designed an experimental TIRF microscopy protocol to examine the accumulation of 3' PIs in the contact area during stimulation with PDGF, and the subsequent decay of the 3' PI level following the addition of a PI 3-kinase inhibitor. These are termed *association-dissociation* experiments because of the net changes in the membrane recruitment of the GFP-AktPH probe induced by the two treatments. Here we wish to use the uniform stimulation model to simulate these experiments, as illustrated in Figure 2.2. In order to visualize the kinetics of GFP-AktPH recruitment as well as the development of a radial 3' PI gradient, three normalized fluorescence values are followed with time: the values at the center and periphery of the contact area ($f(0,\tau)$ and $f(1,\tau)$, respectively), and the value

averaged over the surface of the contact area ($f_{avg}(\tau)$) (Fig. 2.2b). Although the model can accommodate any kinetics for the stimulation of PI 3-kinase activity, for simplicity we assume step changes ($\upsilon_t(\tau) = 1$, $\upsilon_b(\tau) = \nu$ for association, $\upsilon_t(\tau) = \upsilon_b(\tau) = 0$ for dissociation; Appendix A). In the Chapter 3, this assumption is validated for our cells when the concentrations of PDGF and inhibitor are sufficiently high.

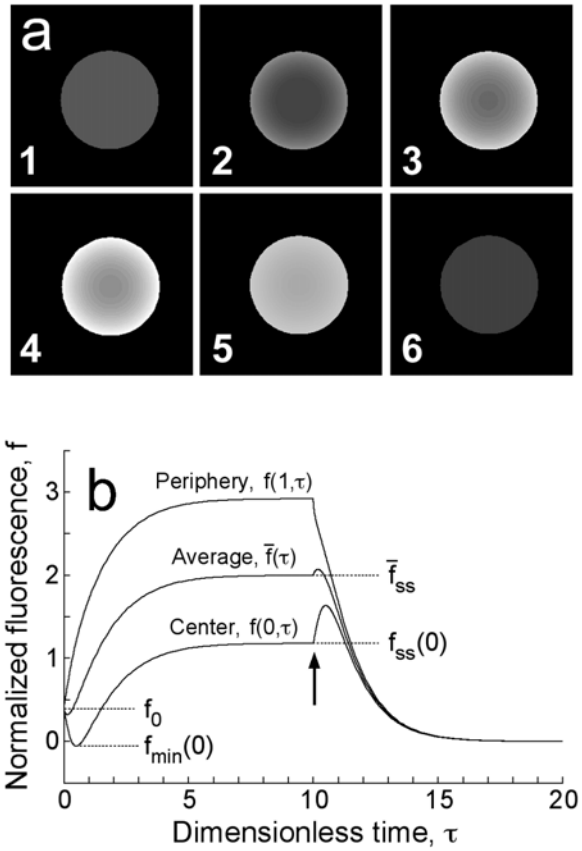

FIGURE 2.2 Simulation of *association-dissociation* fluorescence experiments. Calculations are shown for a simulated cell contact area imaged with total internal reflection fluorescence (TIRF) excitation. Dimensionless parameters are $Da = 3$, $\alpha = \gamma = 1$, $\nu = 0$, $p_{ss} = 0.75$, $\kappa = 0.3$, $\sigma = 16.8$, and $x_0 = 0.047$. (a) Panel 1 shows the simulated cell prior to treatment, and panels 2, 3, and 4 show the contact area at $\tau = 0.5$, 2, and 10 following addition of PDGF, simulated as a step increase in the 3' PI production rate in the top domain (association phase). The 3' PI production is then inhibited abruptly at $\tau = 10$, and the fluorescence decays (dissociation phase); panels 5 and 6 show the contact area at $\tau = 10.6$ and 20. (b) The simulated profiles at all time points were converted into kinetic traces by plotting the normalized fluorescence intensities at the contact area periphery $f(1,\tau)$, at the contact area center $f(0,\tau)$, and averaged over the contact area $f(\tau)_{avg}$. Time zero corresponds to the addition of PDGF, and the arrow signifies the inhibition of PI 3-kinase activity. Also indicated on the plot are the initial fluorescence (f_0), the minimum fluorescence achieved at the contact area center ($f_{min}(0)$), and the steady state fluorescence values at the center ($f_{ss}(0)$) and averaged over the contact area ($f(\tau)_{avg}$).

2.4 RESULTS

2.4.1 The steady state fluorescence profile and aspects of the simulated probe association kinetics are sensitive to the relative rates of 3' PI consumption and diffusion

As described in the previous section, the uniform stimulation model can be used to simulate *association-dissociation* experiments; the simplest and most general aspect of these simulations is the steady state fluorescence profile, $f_{ss}(\rho)$. Two useful metrics that characterize this profile are the ratio of the net fluorescence intensity at the center of the contact area relative to the average, $f_{SS}(0)/f_{avg,SS}$, and the average fluorescence normalized by the extent of probe binding, $f_{avg,SS}/p_{ss}$. Analytical expressions for these quantities are given in Appendix A, and our analysis of these equations is shown in Figure 2.3a&b.

With base parameter assumptions ($\alpha = \gamma = 1$, $\nu = 0$; Fig. 2.3a), the steady state fluorescence profile is determined by *Da*, the Damköhler number that compares the rates of lipid consumption and diffusion, and σ, the fluorescence gain parameter. Hence, from given values of $f_{ss}(0)$ and $f_{avg,SS}$, conservative upper and lower limits on the value of *Da* are imposed. The maximum *Da* is given by the value of $f_{SS}(0)/f_{avg,SS}$ in the limit of very large σ, while the minimum value is set by $f_{avg,SS}/p_{ss} = f_{avg,SS}$. For example, consider a cell with $f_{SS}(0)/f_{avg,SS} = 0.60$ and $f_{avg,SS} = 2.0$. With base parameter assumptions, the range of possible *Da* values is from 2.61 – 4.43, and the lower limit on σ is 13.2. Varying the parameters α, γ, and ν, which relate the consumption rate constants, diffusion coefficients, and steady state generation rates in the two domains, respectively, shifts the $f_{SS}(0)/f_{avg,SS}$ and $f_{avg,SS}/p_{ss}$ curves (Fig. 2.3b). Most significantly, increasing ν requires a higher value of *Da* to achieve the same fluorescence profile, whereas the corresponding value of σ changes very little. Variation of γ, the dimensionless diffusion coefficient in the top domain, has the opposite effect: the required value of *Da* changes little, whereas the value of σ decreases as γ increases. In other words, enhancing the 3' PI flux from the top of the cell into the contact area can be offset simply by decreasing the fluorescence gain σ. Reducing the consumption rate constant in the top membrane domain, by lowering α, has the same effect (not shown).

Additional insights are gained through an analysis of the simulated association kinetics in response to a large dose of PDGF. As depicted in Fig. 2.2, the most compelling

feature of these kinetics is a dip in the fluorescence at the center of the contact area, $f_{min}(0)$, caused at least in part by the recruitment of probe molecules from the cytosol to the top of the

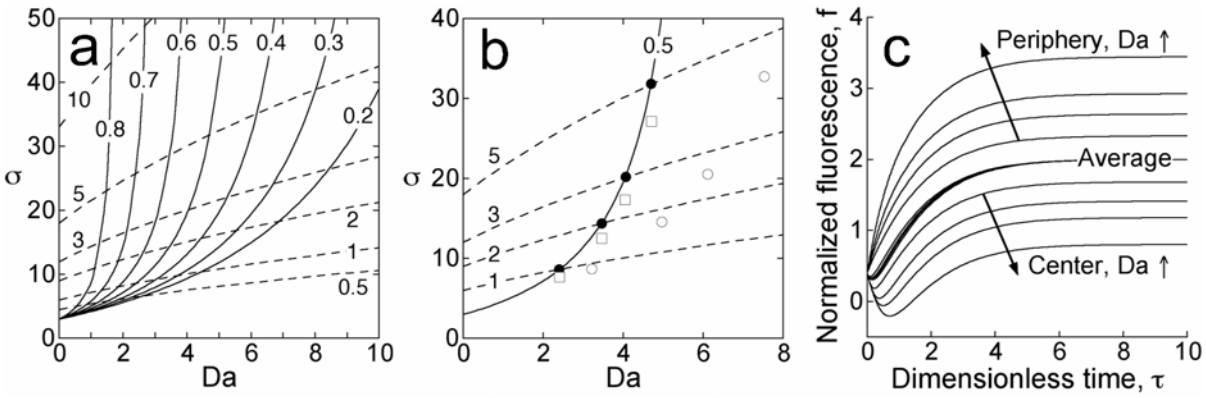

FIGURE 2.3 Effect of 3' PI diffusion on simulated association kinetics. (a & b) Steady state analysis. The curves map the values of the Damköhler number *Da* and gain parameter σ that yield the indicated steady state values of the minimum/average ratio $f_{SS}(0)/f_{avg,SS}$ (solid lines) and average fluorescence/probe binding ratio $f_{avg,SS}/p_{ss}$ (dashed lines), according to Equations A9 and A10, respectively (*Appendix A*). (a) Base case parameters: $\alpha = \gamma = 1$, $\nu = 0$. (b) Closed circles mark the intersections of $f_{SS}(0)/f_{avg,SS}$ and $f_{avg,SS}/p_{ss}$ curves for base case parameters; the open circles are the corresponding positions with $\alpha = \gamma = 1$, $\nu = 0.1$, and the open squares are the positions with $\alpha = 1$, $\gamma = 3$, $\nu = 0$. (c) Simulated association experiments. The following parameters were used: $\alpha = \gamma = 1$, $\nu = 0$, $p_{ss} = 0.75$, $\kappa = 0.3$. As *Da* was varied, the values of σ and x_0 were adjusted to maintain $f_0 = 0.4$ and $f_{avg,SS} = 2.0$, as in Fig. 2.2. Values of *Da* (σ, x_0) are 1 (13.2, 0.064), 2 (15.1, 0.053), 3 (16.8, 0.047), and 5 (19.9, 0.038).

cell. Thus, the fluorescence dip should be sensitive to the rate at which the 3' PIs are distributed between the two membrane domains, determined in the model by the value of *Da*. In Figure 2.3c, probe association was simulated with base parameters ($\alpha = \gamma = 1$, $\nu = 0$), and as *Da* was varied, the gain parameter σ and the basal lipid density x_0 were adjusted so that the initial fluorescence, f_0, and the average fluorescence at steady state, $f_{avg,SS}$, would be set to the same values of 0.4 and 2.0, respectively. In addition to affecting the steady state profile (as predicted from Fig. 2.3a), increasing the value of *Da* also affects the initial dip at the center of the contact area. As the rate of lipid diffusion is effectively reduced, lower values of $f_{min}(0)$ are achieved, and the minimum fluorescence occurs at later times.

2.4.2 Kinetic analyses varying the parameters α and γ: what can we say about the top of the cell?

The dimensionless constants α and γ are ratios of the consumption rate constants and diffusion coefficients in the two domains, respectively ($\alpha \equiv k_t/k_b$; $\gamma \equiv D_t/D_b$). Deviation from the base assumptions ($\alpha = \gamma = 1$) would thus accommodate spatially regulated lipid consumption activities or a reduced molecular mobility in the adherent contact area. As shown in the steady state analysis (Fig. 2.3b), these parameters affect the lipid flux from the top to the bottom of the cell, which influences the magnitude of the steady state 3' PI profile $x_{b,ss}(\rho)$ but not its shape; i.e., the same steady state fluorescence profile $f_{ss}(\rho)$ can be attained by adjusting the gain parameter σ. However, variation of these parameters may also affect the association and/or dissociation kinetics; indeed, at least for α, it would be surprising if this were not so.

Dissociation experiments focus on the kinetics of 3' PI consumption. Analysis of the model equations indicates that, during dissociation with $\alpha < 1$, the minimum/average ratio $f_{SS}(0)/f_{avg,SS}$ should approach a pseudo-steady state value that is also less than one. This is confirmed in Figure 2.4a&b. When α is less than one, the center, average, and periphery fluorescence curves clearly do not converge (Fig. 2.4a), and $f_{SS}(0)/f_{avg,SS}$ does not approach unity (Fig. 2.4b). We conclude that the assumption $\alpha = 1$ can be accepted when fluorescence profiles consistently become homogeneous during the dissociation time course. Varying γ, on the other hand, does not significantly alter the kinetics of association or dissociation once the σ and x_0 values are adjusted to match the values of f_0 and $f_{avg,SS}$ (Fig. 2.4c and results not shown). Therefore, the model is not uniquely sensitive to and cannot be used to evaluate D_t. It is heartening, however, that the variation of γ by as much as a factor of 3 affects the estimation of σ and x_0 only modestly and does not influence the estimation of the other parameters. Based on the considerations above, we will assume that both α and γ are equal to one for the remainder of this work.

2.4.3 The dip in fluorescence at the center of the contact area is sensitive to characteristics of the intracellular probe

Motivated by the prominence of the transient dip in fluorescence at the center of the contact area, $f_{min}(0)$, a full parametric analysis of this metric was performed. As in the previous sections, the parameters were adjusted to achieve the same values of f_0 and $f_{avg,SS}$ (0.40 and 2.00, respectively); the value of $f_{ss}(0)$ was also set here to 1.18, the value obtained with $Da = 3$ in Figs. 2.2-2.4. Two assumptions regarding the PI 3-kinase activity in the contact area were examined, corresponding to its disappearance or maintenance of the basal activity ($\nu = 0$ or $\nu = x_0$, respectively). With these constraints, and assuming $\alpha = \gamma = 1$, the specification of any two model parameters, among Da, σ, x_0, p_{ss}, and κ (μ can be substituted for either p_{ss} or κ), yields the values of the remaining three. With all of the dimensionless parameters in hand, the value of $f_{min}(0)$ follows.

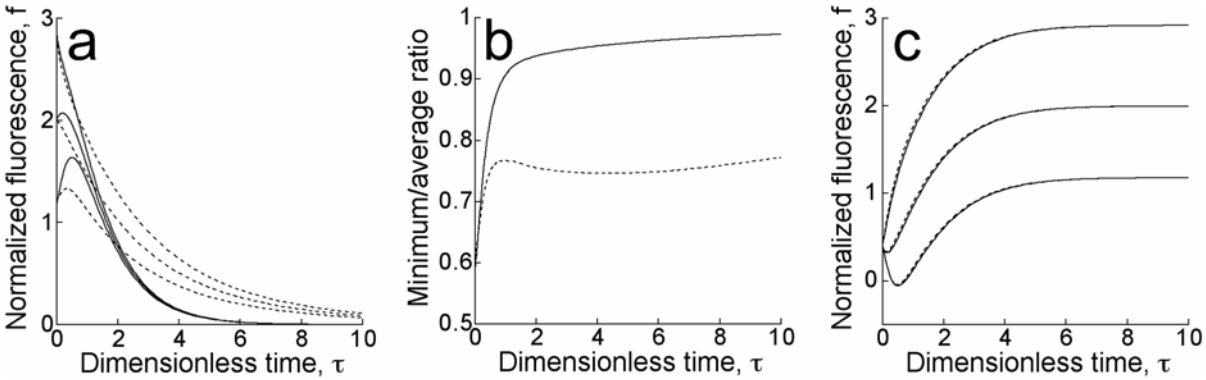

FIGURE 2.4 Consumption and diffusion of 3' PIs in the top and bottom domains. Unless otherwise noted, the following parameters were used: $Da = 3$, $\alpha = \gamma = 1$, $\nu = 0$, $p_{ss} = 0.75$, $\kappa = 0.3$. The values of σ and x_0 were adjusted to maintain $f_0 = 0.4$ and $f_{avg,SS} = 2.0$, as in Figs. 2.2 & 2.3. (a) Calculated dissociation time courses with $\alpha = 1$, $\sigma = 16.8$ (solid lines) or $\alpha = 0.3$, $\sigma = 20.0$ (dashed lines). (b) The minimum/average ratio, calculated from the data in (a), does not approach unity when $\alpha \neq 1$. (c) Calculated association time courses with $\gamma = 1$, $\sigma = 16.8$, $x_0 = 0.047$ (solid lines) or $\gamma = 3$, $\sigma = 14.7$, $x_0 = 0.055$ (dashed lines).

The dependence of $f_{min}(0)$ on the extent of probe binding p_{ss} with various values of κ, μ, or x_0 is shown in Figure 2.5, yielding a number of conclusions. As expected, lower $f_{min}(0)$ values are achieved when more of the probe is recruited from the cytosol (higher p_{ss}). For a given value of p_{ss}, lower $f_{min}(0)$ values are achieved with higher κ; with the extent of binding

fixed and a lower probe affinity, the 3' PI lipids must increasingly outnumber probe molecules, allowing more of the probe to be recruited to the top of the cell before diffusion can redistribute the lipid (also seen with higher μ). Also, comparison of Fig. 2.5a&b shows that a significantly lower value of $f_{min}(0)$ is achieved when the basal PI 3-kinase activity disappears from the contact area (ν = 0). The sudden loss of PI 3-kinase activity from the bottom of the cell, in concert with the increase in PI 3-kinase activity at the top, exacerbates the initial decrease in fluorescence at the center of the contact area.

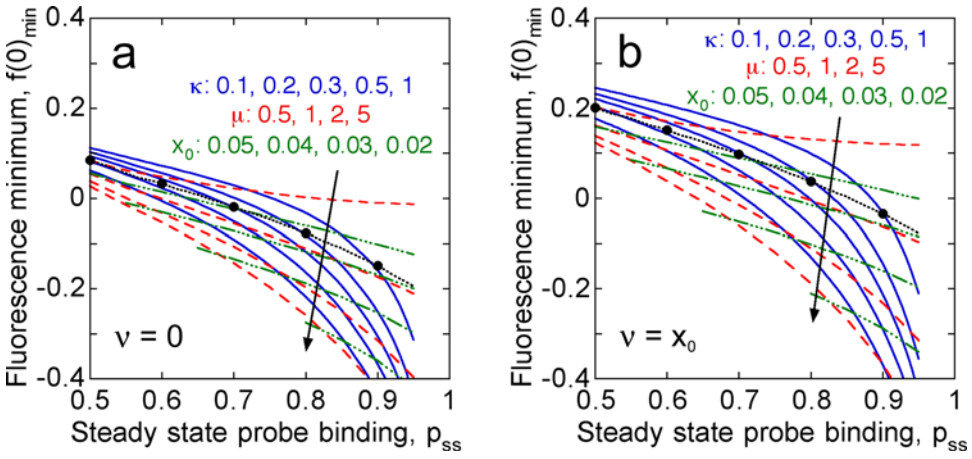

FIGURE 2.5 Parametric analysis of the dip in center fluorescence. The minimum fluorescence at the center of the contact area, $f_{min}(0)$, was calculated for various values of p_{ss} with ν = 0 (a) or ν = x_0 (b), and other parameters chosen to maintain $f_0 = 0.40$, $f_{avg,SS} = 2.00$, and $f_{ss}(0) = 1.18$. Curves are for constant values of κ (0.1, 0.2, 0.3, 0.5, or 1; blue), μ (0.5, 1, 2, or 5; red), or x_0 (0.02, 0.03, 0.04, or 0.05; green). The black curves satisfy κ = 1 – p_{ss}.

2.4.4 Fluorescence measurements can be used to identify bounds on the relative rates of 3' phosphoinositide consumption versus diffusion and other dimensionless groups

The constraints-based approach presented in Figure 2.5 also delineates limiting behavior, which is important for the analysis of experiments. For example, there exists a minimum p_{ss} required to achieve a given $f_{min}(0)$, evaluated in the limit of very large κ or μ (the μ = 5 curves in Fig. 2.5a&b suffice here). In this limit, it is ensured that the free lipid is always in great excess over bound probe. For a given $f_{min}(0)$, there also exists an upper limit on p_{ss}, evaluated in the limit of vanishing κ. In this limit, the probe affinity is high enough that the amount of bound probe is approximately equal to the total number of 3' PI or probe

molecules, whichever is smaller. An intermediate condition, then, would be a parameter set for which half of the lipid is bound by probe at steady state, satisfied by $\kappa = 1 - p_{ss}$ (marked by the black curves in Fig. 2.5a&b). The corresponding values of x_0 in those limits can also be discerned from Figure 2.5a&b. One may thus identify those parameter sets that yield certain values of $f_{min}(0)$ as well as f_0, $f_{avg,SS}$, and $f_{ss}(0)$, e.g., as observed in an experiment. Taken together, the large μ limit, the low κ limit, and the assumption that ν is no greater than x_0 define useful parameter ranges, as shown in Table 2 with $f_0 = 0.40$, $f_{avg,SS} = 2.00$, $f_{ss}(0) = 1.18$, and $f_{min}(0) = 0.00$.

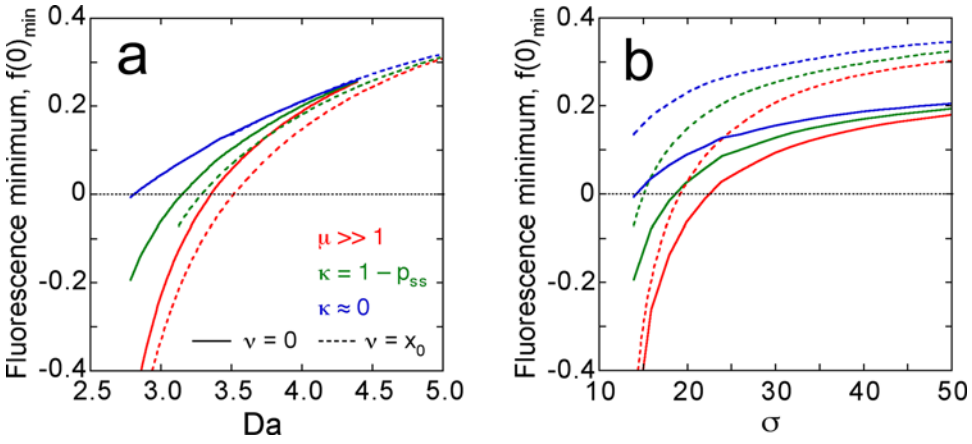

FIGURE 2.6 Identification of upper and lower bounds on the dimensionless parameters. Relationships between the value of *Da* (a) or σ (b) and the $f_{min}(0)$ achieved, with other parameters chosen to set $f_0 = 0.40$, $f_{avg,SS} = 2.00$, and $f_{ss}(0) = 1.18$ as in Fig. 2.5. Solid lines are with $\nu = 0$; dashed lines are with $\nu = x_0$. Colors signify the high-affinity limit ($\kappa = 10^{-3}$; blue), the excess-lipid limit ($\mu = 5$; red), or the intermediate condition ($\kappa = 1 - p_{ss}$; green). The global *Da* and σ minima (evaluated at $\nu = 0$, $p_{ss} = 1$) are 2.73 and 13.4, respectively.

Indeed, the limits on *Da* in particular can be relatively narrow, as explored further in Figure 2.6a for a wide range of $f_{min}(0)$ values. With $f_{min}(0) = 0.00$, the upper and lower limits on *Da* are 2.81 and 3.52, respectively (Table 2.2), a difference of 22%. As shown in Fig. 2.6a, it is often the case that one or more of the limiting cases is unable to yield the specified fluorescence values; the inclusion of the intermediate case, $\kappa = 1 - p_{ss}$, is therefore a compromise to define more of the allowable parameter space. Thus, with the fluorescence values given it is apparent that the range of *Da* values would be even narrower for $f_{min}(0)$ values above or below 0.00 (Fig. 2.6a). Figure 2.6b shows the corresponding limits on the

value of σ. Of note here is the insensitivity of $f_{min}(0)$ to the value of σ when the dip in fluorescence is relatively shallow, which can lead to arbitrarily high estimates of σ for certain values of $f_{min}(0)$.

With the four values f_0, $f_{avg,SS}$, $f_{ss}(0)$, and $f_{min}(0)$ specified, is it possible to distinguish different parameter sets based on other aspects of the association and/or dissociation kinetics? This is addressed in Figure 2.7 by comparing the kinetics simulated with the five sets of parameters listed in Table 2.2. It is apparent that, with the data features fixed in this manner, there is relatively little difference among the association time courses for these parameter sets. However, in the dissociation kinetics there is significant variation in the onset of fluorescence decay. The decay is delayed when most of the probe is bound yet free

TABLE 2.2 Parameter sets that yield f_0 = 0.40, $f_{avg,SS}$= 2.00, $f_{ss}(0)$ = 1.18, and $f_{min}(0)$ = 0.00 *

	Set 1 $\nu = 0$, $\mu = 5$	***Set 2*** $\nu = 0$, $\kappa = 1 - p_{ss}$	***Set 3*** $\nu = 0$, $\kappa = 10^{-3}$	***Set 4*** $\nu = x_0$, $\mu = 5$	***Set 5*** $\nu = x_0$, $\kappa = 1 - p_{ss}$	***Set 6*** $\nu = x_0$, $\kappa = 10^{-3}$
p_{ss}	**0.533**	0.664	**0.927**	0.641	0.861	none [#]
Da	3.36	3.15	**2.81**	**3.52**	3.29	
σ	**22.6**	18.7	**14.2**	19.3	15.1	
x_0	0.0403	0.0524	**0.0760**	**0.0332**	0.0453	

* Parameter extremes for these fluorescence characteristics are highlighted in bold.
[#] The specified fluorescence characteristics cannot be achieved with these constraints.

3' PI molecules are abundant, and the deviation from single exponential decay can be assessed using the ratio of the rate of decrease in p over its value, $(-dp/d\tau)/p = -d(\ln p)/d\tau$ with pure single exponential decay, this quantity is equal to one. In the initial decay from the steady state, we find that

$$-\left.\frac{d(\ln p)}{d\tau}\right|_{\tau=0} = \frac{1+\kappa(1-p_{SS})^{-1}}{1+\kappa(1-p_{SS})^{-2}} \qquad (2.5).$$

For comparison, the values of $-d(\ln p)/d\tau$ at the beginning of the dissociation runs for parameter sets 1 through 5 in Fig. 2.7 are 0.48, 0.50, 0.85, 0.37, and 0.24 respectively.

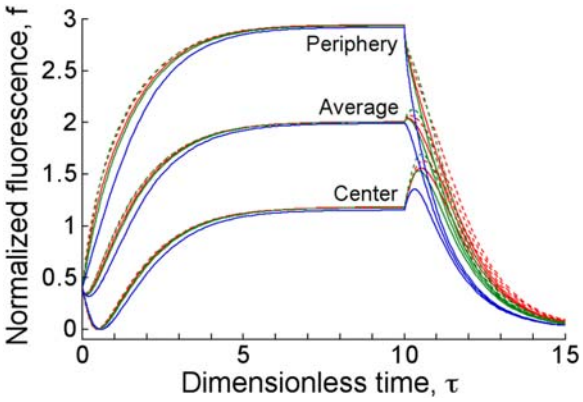

FIGURE 2.7 Simulated association-dissociation kinetics with extreme parameter sets. The five extreme parameter sets listed in Table 2.2, satisfying $f_0 = 0.40$, $f_{avg,SS} = 2.00$, $f_{ss}(0) = 1.18$, and $f_{min}(0) = 0.00$ in various limits, were used to simulate association-dissociation experiments in dimensionless time. Solid lines are with $\nu = 0$; dashed lines are with $\nu = x_0$. Colors signify the high-affinity limit ($\kappa = 10^{-3}$; blue), the excess-lipid limit ($\mu = 5$; red), or the intermediate condition ($\kappa = 1 - p_{ss}$; green).

2.5 DISCUSSION

Live-cell fluorescence experiments have yielded significant insights into the regulation of intracellular signaling events (Weijer, 2003). Unlike biochemical methods, the use of specific fluorescent probes gives us direct spatial information, but a shortcoming of this approach is that image analysis introduces a significant bottleneck. The fact that cells, as individuals, behave in various ways means that a large and tedious effort is generally required to characterize spatially regulated signaling processes, and a compromise must be made between spatial resolution and the number of cells observed in each experiment (Teruel and Meyer, 2002). We have formulated a generalized mathematical model that can be directly compared with total internal reflection fluorescence (TIRF) microscopy experiments, and a methodology was devised for extracting ranges of dimensionless parameter values from only four well-defined fluorescence intensity measurements: the initial fluorescence, the minimum fluorescence at the center of the contact area, and two features of the steady state fluorescence profile. From an image analysis point of view, this approach is simple enough that it could be automated, and thus the characterization of individual cell parameters might be accelerated.

In terms of the 3' PI dynamics, the key dimensionless group is *Da*, which relates the effective rates of 3' PI turnover and diffusion. We have demonstrated that this parameter can be estimated with adequate precision, with typical differences between the minimum and maximum *Da* values of ~ 20% or less. Our robust parameter estimation method achieves this precision without regression fitting, although it would be necessary then to fit or otherwise compare points in time in order to obtain the dimensional values of the effective 3' PI diffusion coefficient, *D*, and turnover rate constant, *k*. Indeed, this is the approach taken as this methodology was applied to the analysis of actual experiments (described in Chapter 3).

A simplification in the model was the choice of an idealized yet reasonable cellular geometry, in which the contact area is circular. A square contact area (which has the same area/perimeter ratio as a circle inscribed within it) yielded almost identical results, while rectangular areas with large aspect ratios require a *Da* value almost 2 times lower to achieve a similar profile (results not shown). As cells are analyzed, then, the variability of the

contact area geometry should be acknowledged or accounted for (as will be described in Chapter 4). The shape of the top domain is less critical, however, because the 3' PI distribution in the nonadherent membrane simply provides the boundary flux into the contact area. The major determinant of the flux is the relative surface area of the top membrane domain; i.e., the top domain contains two-thirds of the membrane area for a hemispherical cell, compared with one-half for a 'pancake' morphology. Such differences can be artificially offset by adjusting the value of the TIRF gain parameter, σ, as shown for changes in the ratio of diffusion coefficients, γ (Fig. 2.4c).

Another issue related to the morphology of fibroblasts and other anchorage-dependent cells is the presence of thin structures, such as filopodia and the trailing uropod, radiating from the adhesion zone, which are expected to exhibit 3' PI profiles that are different from the body of the contact area. In such a structure, 3' PIs are expected to diffuse across its width before significant turnover can occur; thus, for the same rate of 3' PI production in the nonadherent membrane, the thinner structures would appear brighter when excited by TIRF. This is indeed what has been generally observed in filopodia-like structures, but not uropods, of our cells (Haugh et al., 2000). The question thus arises whether or not the 3' PI production rate is differentially regulated in such structures so as to further enhance or abrogate the accumulation of 3' PIs. This question is addressed in Chapter 4, when we examine the underlying kinetics of these regions. In any case, the dependence of the 3' PI level on cell morphology is a direct outcome of the restriction of PDGF-stimulated 3' PI production to the nonadherent portion of the cell, and it is intriguing that 3' PIs in turn control cell morphology through the regulation of cell spreading and motility.

A second simplification in our analysis was the assumption that PDGF stimulation induces step changes in the PI 3-kinase activities associated with the two domains, which is justified when the concentration of PDGF is sufficiently high. This assumption is not necessary however, because the generalized model can accommodate any kinetics. Indeed, we are currently working to incorporate a recently developed kinetic model of PDGF receptor phosphorylation and PI 3-kinase recruitment (Park et al., 2003). Although the inclusion of receptor-mediated processes comes with an increase in the number of model parameters, it would allow the application of the model to a much wider range of

experimental conditions. Clearly, adding complexity to any model of intracellular signaling in a judicious manner requires a significant amount of quantitative experimental data, and in this respect fluorescence imaging of individual cells and biochemical measurements of cell populations are expected to complement each other.

2.6 REFERENCES

Asthagiri AR, Lauffenburger DA. 2000. Bioengineering models of cell signaling. Annu. Rev. Biomed. Eng. 2: 31-53.

Axelrod D. 2001. Total internal reflection fluorescence microscopy in cell biology. Traffic 2: 764-774.

Botelho RJ, Teruel M, Dierckman R, Anderson R, Wells A, York JD, Meyer T, Grinstein S. 2000. Localized biphasic changes in phosphatidylinositol-4,5-bisphosphate at sites of phagocytosis. J. Cell Biol. 151: 1353-1367.

Deen WM. 1998. Analysis of transport phenomena. Oxford University Press.

Fink CC, Slepchenko B, Moraru II, Schaff J, Watras J, Loew LM. 1999. Morphological control of inositol-1,4,5-trisphosphate-dependent signals. J. Cell Biol. 147: 929-935.

Harriague J, Bismuth G. 2002. Imaging antigen-induced PI3K activation in T cells. Nat. Immunol. 3: 1090-1096.

Haugh JM. 2002. A unified model for signal transduction reactions in cellular membranes. Biophys. J. 82: 591-604.

Haugh JM, Codazzi F, Teruel M, Meyer T. 2000. Spatial sensing in fibroblasts mediated by 3' phosphoinositides. J. Cell Biol. 151: 1269-1279.

Haugh JM, Lauffenburger DA. 1998. Analysis of receptor internalization as a mechanism for modulating signal transduction. J. Theor. Biol. 195: 187-218.

Hunter T. 2000. Signaling– 2000 and beyond. Cell 100: 113-127.

Levchenko A, Iglesias PA. 2002. Models of eukaryotic gradient sensing: application to chemotaxis of amoebae and neutrophils. Biophys. J. 82: 50-63.

Marshall JG, Booth JW, Stambolic V, Mak T, Balla T, Schreiber AD, Meyer T, Grinstein S. 2001. Restricted accumulation of phosphatidylinositol 3-kinase products in a plasmalemmal subdomain during Fc gamma receptor-mediated phagocytosis. J. Cell Biol. 153: 1369-1380.

Narang A, Subramanian KK, Lauffenburger DA. 2001. A mathematical model for chemoattractant gradient sensing based on receptor-regulated membrane phospholipid signaling dynamics. Ann. Biomed. Eng. 29: 677-691.

Parent CA, Devreotes PN. 1999. A cell's sense of direction. Science 284: 765-770.

Park CS, Schneider IC, Haugh JM. 2003. Kinetic analysis of platelet-derived growth factor receptor/phosphoinositide 3-kinase/Akt signaling in fibroblasts. J. Biol. Chem. 278: 37064-37072.

Postma M, Van Haastert PJM. 2001. A diffusion-translocation model for gradient sensing by chemotactic cells. Biophys. J. 81: 1314-1323.

Pribyl M, Muratov CB, Shvartsman SY. 2003. Long-range signal transmission in autocrine relays. Biophys. J. 84: 883-896.

Rameh LE, Cantley LC. 1999. The role of phosphoinositide 3-kinase lipid products in cell function. J. Biol. Chem. 274: 8347-8350.

Schaff J, Fink CC, Slepchenko B, Carson JH, Loew LM. 1997. A general computational framework for modeling cellular structure and function. Biophys. J. 73: 1135-1146.

Shea LD, Omann GM, Linderman JJ. 1997. Calculation of diffusion-limited kinetics for the reactions in collision coupling and receptor cross-linking. Biophys. J. 73: 2949-2959.

Steyer JA, Almers W. 2001. A real-time view of life within 100 nm of the plasma membrane. Nat. Rev. Mol. Cell Biol. 2: 268-275.

Swaminathan R, Hoang CP, Verkman AS. 1997. Photobleaching recovery and anisotropy decay of green fluorescent protein GFP-S65T in solution and cells: cytoplasmic viscosity probed by green fluorescent protein translational and rotational diffusion. Biophys. J. 72: 1900-1907.

Teruel MN, Meyer T. 2002. Parallel single-cell monitoring of receptor-triggered membrane translocation of a calcium-sensing protein module. Science 295: 1910-1912.

Toomre D, Manstein DJ. 2001. Lighting up the cell surface with evanescent wave microscopy. Trends Cell Biol. 11: 298-303.

Vanhaesebroeck B, Leevers SJ, Ahmadi K, Timms J, Katso R, Driscoll PC, Woscholski R, Parker PJ, Waterfield MD. 2001. Synthesis and function of 3-phosphorylated inositol lipids. Annu. Rev. Biochem. 70: 535-602.

Wang F, Herzmark P, Weiner OD, Srinivasan S, Servant G, Bourne HR. 2002. Lipid products of PI(3)Ks maintain persistent cell polarity and directed motility in neutrophils. Nat. Cell Biol. 4: 513-518.
Weijer CJ. 2003. Visualizing signals moving in cells. Science 300: 96-100.
Weiner OD. 2002. Regulation of cell polarity during eukaryotic chemotaxis: the chemotactic compass. Curr. Opin. Cell Biol. 14: 196-202.
Weng G, Bhalla US, Iyengar R. 1999. Complexity in biological signaling systems. Science 284: 92-96.
Xu C, Watras J, Loew LM. 2003. Kinetic analysis of receptor-activated phosphoinositide turnover. J. Cell Biol. 161: 779-791.
Yokoe H, Meyer T. 1996. Spatial dynamics of GFP-tagged proteins investigated by local fluorescence enhancement. Nature Biotech. 14: 1252-1256.

Chapter 3

Spatial Analysis of 3' Phosphoinositide Signaling in Living Fibroblasts: II. Parameter Estimates for Individual Cells from Experiments

Adapted from Schneider and Haugh, Biophys. J., 86: 599-608 (2004)

3.1 ABSTRACT

Fibroblast migration is directed by gradients of platelet-derived growth factor (PDGF) during wound healing. As in other chemotactic systems, it has been shown recently that localized stimulation of intracellular phosphoinositide (PI) 3-kinase activity and production of 3' PI lipids in the plasma membrane are important events in the signaling of spatially biased motility processes. In turn, 3' PI localization depends on the effective diffusion coefficient, D, and turnover rate constant, k, of these lipids. Here we present a systematic and direct comparison of mathematical model calculations and experimental measurements to estimate the values of the effective 3' PI diffusion coefficient, D, turnover rate constant, k, and other parameters in individual fibroblasts stimulated uniformly with PDGF. In the context of our uniform stimulation model, the values of D and k in each cell were typically estimated within 10-20% or less, and the mean values across all of the cells analyzed were $D = 0.37 \pm 0.25$ $\mu m^2/s$ and $k = 1.18 \pm 0.54$ min^{-1}. In addition, we report that 3' PI turnover is not affected by PDGF receptor signaling in our cells, allowing us to focus our attention on the regulation of 3' PI production as this system is studied further.

3.2 INTRODUCTION

Fibroblasts in tissue respond to a host of growth factors, including forms of platelet-derived growth factor (PDGF), fibroblast growth factor, insulin-like growth factor, and heparin-binding epidermal growth factor. These factors act through specific cell surface receptors of the receptor tyrosine kinase family, which activate a common set of intracellular signal transduction pathways to elicit cell proliferation (van der Geer et al., 1994; Schlessinger, 2000). PDGF is also a chemoattractant, stimulating directed migration (chemotaxis) of fibroblasts and other cell types towards a PDGF gradient (Heldin and Westermark, 1999). Such gradients are formed in tissue during wound healing, through secretion of PDGF by activated platelets, and are important for recruitment of fibroblasts as well as macrophages to the wound site (Martin, 1997).

One requirement for stimulating directed cell motility is the coupling of receptor signaling to regulation of the actin cytoskeleton, and in this respect the PDGF receptor-mediated chemotactic pathway has largely been elucidated. Activated PDGF receptors recruit type IA phosphoinositide (PI) 3-kinases to the inner leaflet of the plasma membrane, where these enzymes phosphorylate the lipid substrate phosphatidylinositol (4,5)-bisphosphate (PtdIns(4,5)P2), producing the 3' PI lipid second messenger PtdIns(3,4,5)P3 (Vanhaesebroeck and Waterfield, 1999). Another 3' PI, PtdIns(3,4)P2, is subsequently formed from PtdIns(3,4,5)P3 (Hawkins et al., 1992). 3' PIs and other phosphoinositides function by recruiting signaling proteins to the plasma membrane through interactions with pleckstrin homology (PH) domains and other protein motifs (Cullen et al., 2001; McLaughlin et al., 2002). The importance of 3' PI-dependent signaling pathways in PDGF-stimulated chemotaxis was established in a number of studies, in which blocking PI 3-kinase recruitment or activity abolished cell migration towards PDGF (Kundra et al., 1994; Wennström et al., 1994a; Wennström et al., 1994b; Wymann and Arcaro, 1994). One of the important molecular players that couple PDGF-stimulated 3' PI production to actin rearrangements and cell movement is the small GTPase Rac, which mediates membrane ruffling and formation of the lammellipod, the leading membrane edge in a migrating cell (Ridley et al., 1992; Hawkins et al., 1995; Hooshmand-Rad et al., 1997).

Eukaryotic cells respond to chemoattractant gradients by distinguishing the levels of receptor-ligand binding in different cellular locations, a process called spatial sensing. Thus, another aspect of chemotactic signaling is the polarized spatial localization of the pathway components, which biases membrane protrusion in the direction of the chemoattractant gradient (Weiner, 2002). Indeed, it has been shown recently that intracellular gradients of 3' PIs are generated in the plasma membranes of fibroblasts exposed to a PDGF gradient (Haugh et al., 2000). Interestingly, fibroblasts uniformly stimulated with PDGF also showed intracellular 3' PI membrane gradients, increasing radially from the center to the periphery of the contact area. The radial gradients were consistent with a restriction of PDGF receptor-mediated 3' PI production to the top of the cell, and the evolution of the gradient in a representative cell was used in conjunction with a mathematical model to give rough estimates of the 3' PI diffusion coefficient and turnover rate constant (Haugh et al., 2000). The ratio of these two parameters defines the spatial range of a second messenger, providing a biophysical basis for the ability of an intracellular molecule to transduce a localized signal for spatial sensing and chemotaxis.

Although many of the molecular requirements in PDGF-stimulated cell motility have been established, the PI 3-kinase-mediated spatial sensing mechanism is still in the process of being characterized. Lingering questions surround the ability of the mechanism to be robust yet sensitive to shallow gradients (Weiner, 2002). It is also unclear to what extent spatial sensing mechanisms are conserved across cell and receptor types. We are working towards a unified model that explains the 3' PI signaling responses of fibroblasts to both uniform and gradient PDGF stimulation. In such a model, it is important to establish which processes depend on the mode of PDGF presentation and which do not. For those processes not regulated by receptor signaling, parameter values obtained under uniform stimulation conditions, which are easier to implement, analyze, and reproduce, are expected to translate to the more complicated gradient stimulation case. Whereas it is established that production of 3' PIs is regulated through PDGF receptor modulation of PI 3-kinase activity, the possible regulation of 3' PI turnover, through the action of PI 3-phosphatase activities, has not been studied in detail.

In Chapter 2, a generalized uniform stimulation model was presented, and it was shown that fluorescence measurements could be used to delineate constraints on the parameter values. In this chapter, a systematic series of experiments were performed, and the model was found to be generally suitable for capturing the observed 3' PI dynamics in individual fibroblasts. An important qualitative finding is that 3' PI turnover is not regulated by PDGF receptor signaling, suggesting fundamental differences in the spatial sensing mechanisms utilized by different classes of chemoattractant receptors. Quantitative results include rigorous estimates of the effective 3' PI diffusion coefficient, D, the 3' PI turnover rate constant, k, and other parameters in individual cells. Our approach allowed the precision of these single-cell parameter estimates as well as the cell-to-cell variability of the parameter values to be evaluated. The minimum and maximum estimated values of D and k in each cell typically showed a difference of less than 20%, while the values from cell to cell were typically within a factor of 2 of the mean.

3.3 MATERIALS AND METHODS

3.3.1 cDNA constructs, cell culture, and transfection

The GFP-AktPH construct consists of the PH domain of mouse Akt-1 attached with a short linker to the C-terminus of enhanced green fluorescent protein, made by cloning into BamHI/XbaI of pEGFP-C1 (Clontech). This insert was also cloned into the same sites of pEYFP-C1 and pECFP-C1, yielding YFP-AktPH and CFP-AktPH, respectively. Membrane-targeted lyn-CFP contains the palmitoylation sequence from Lyn (Teruel et al., 1999) cloned into pECFP-N1. Unless otherwise noted, all tissue culture reagents were from Invitrogen or Sigma. NIH 3T3 fibroblasts (American Type Culture Collection) were subcultured in 10 cm tissue culture dishes with DMEM medium containing 10% fetal bovine serum, 2 mM L-glutamine, and the antibiotics penicillin and streptomycin. Cells were seeded onto 25 mm square glass cover slips, pre-coated with poly-D-lysine, and were later transfected with the vector(s) indicated using Lipofectamine Plus (Invitrogen). After 24 hours, transfected cells were incubated in serum-free DMEM medium with 2 mM L-glutamine, penicillin and streptomycin, and 1 mg/ml fatty acid-free bovine serum albumin (BSA) for four hours prior to imaging.

3.3.2 Total internal reflection fluorescence (TIRF) microscopy

TIRF microscopy was performed essentially as described (Haugh et al., 2000). In this technique, an evanescent wave is produced with energy that decays exponentially with distance into the sample (characteristic space constant ~100 nm), selectively exciting fluorophores in close proximity to the membrane-substratum contact area (Axelrod, 2001; Steyer and Almers, 2001; Toomre and Manstein, 2001). Our TIRF excitation source was from a Melles Griot tunable wavelength laser head, emitting lines of 457 nm (ECFP, 15 mW), 488 nm (EGFP, 60 mW), or 514 nm (EYFP, 60 mW); each line was used at maximum power. A shutter with controller was from Vincent Associates. Other components included a base stand and water immersion objectives (Zeiss), emission filter wheel with controller (Ludl), and band pass emission filters (480/30 nm for ECFP, 515/30 nm for EGFP, 535/30 nm for EYFP; Chroma). Digital images were acquired using a Hamamatsu ORCA ER cooled CCD and later analyzed with Metamorph software (Universal Imaging). The imaging

buffer was composed of 20 mM HEPES pH 7.4, 125 mM NaCl, 5 mM KCl, 1.5 mM MgCl2, 1.5 mM CaCl2, 10 mM glucose, and 2 mg/ml fatty acid-free BSA. Fields of cells were visualized at a combined magnification of 25x over a 20 minute time course, acquiring TIRF images with 2x2 binning every 10 seconds, with each image integrated over an exposure time of ca. 500 ms.

3.3.3 Association-dissociation experiments and analysis of radial fluorescence profiles

Our time course experiments consisted of two distinct phases, as shown in Figure 3.1. After recording the basal, unstimulated fluorescence for one minute, cells were first stimulated with a uniform concentration of human recombinant PDGF-BB (Peprotech) to activate generation of 3' PIs and recruitment of GFP-AktPH. In the second phase of the time course, a high concentration of wortmannin (5 μM; Sigma) was added to halt 3' PI production, allowing the kinetics of 3' PI consumption to be isolated. To signify these two treatments and the changes they elicit, such time courses are termed *association-dissociation* experiments (Fig. 3.1a).

The spatial fluorescence profile for each cell was processed in the following manner. A line was drawn through the shortest distance across the contact area, to include the center (which exhibits the lowest intensity once the radial gradient is established), and at each time point the pixel intensities along this line were imported into Excel (Fig. 3.1b). The background intensity, averaged over several pixels in acellular areas adjacent to the cell, was subtracted from each value. The fluorescence intensities at the center of the contact area and each of the two endpoints at the contact area periphery (exhibiting the maximum intensities in the radial gradient) were each averaged with their two adjacent pixel values, and the two resulting periphery values were then averaged. The fluorescence intensity averaged over the length of the line scan was calculated by taking sums over all pixels *i* between and including the endpoints:

$$\overline{F} = \sum_i F_i \times r_i \Big/ \sum_i r_i \qquad (3.1),$$

where F_i and r_i are the fluorescence intensity and absolute distance from the center, respectively, for pixel i. Thus, the line is effectively extrapolated to a circular area, over which the average is taken. Finally, the center, periphery, and average intensities were normalized using the cytosolic fluorescence intensity, F_{cyt}, taken as the mean of the intensities at the last 6 time points (after the wortmannin treatment has dissociated all GFP-AktPH molecules from the membrane); the normalized intensity, f, is defined as

$$F = \frac{F - F_{cyt}}{F_{cyt}} \qquad (3.2).$$

By plotting as a function of time the normalized fluorescence at the center of, at the periphery of, and averaged over a line scan through the contact area, one can effectively visualize the kinetics of 3' PI accumulation as well as the development of a radial 3' PI gradient in the contact area (Fig. 3.1c).

The intensity of TIRF emission is a function of distance from the glass-buffer interface as well as the fluorophore concentration. Therefore it is important to ensure that the separation distance of the cell does not change significantly during the time course. This was confirmed in a number of control experiments, each subjected to the association-dissociation procedure (results not shown). These involved cells transfected with soluble GFP variants and membrane targeted lyn-CFP, untransfected cells with FITC-labeled dextran added to the medium, and cells co-transfected with YFP-AktPH and lyn-CFP. In all cases, neither PDGF nor wortmannin prompted significant changes in the apparent membrane-substratum separation distance. These experiments also allowed us to rule out the influence of significant photobleaching, as did a series of experiments in which the duration of PDGF stimulation, prior to wortmannin addition, was varied. Finally, the dissociation responses were carried out with various doses of wortmannin to address the specificity of this treatment. Concentrations of 100 nM and above brought the fluorescence to similar values relative to the unstimulated level. However, a dose above 1 μM was required to block PI 3-kinase most rapidly; i.e., lower concentrations yielded fluorescence decay rates limited by the rate of wortmannin interaction with PI 3-kinase. Another PI 3-kinase inhibitor, LY294002,

yielded similar kinetics and extent of fluorescence decrease when added at high concentration (250 μM; data not shown).

3.4 RESULTS

3.4.1 Fibroblasts exhibit distinct spatiotemporal features in association-dissociation experiments

As exemplified in Figure 3.1c, GFP-AktPH-transfected cells consistently showed a number of reproducible characteristics in our *association-dissociation* experiments. Each displayed a detectable 3' PI level prior to stimulation, as judged by the offset between the fluorescence intensities at the beginning and end of the experiment, defined as f_0. In response to stimulation with PDGF-BB concentrations above ~ 0.01 nM, a fluorescence increase was detected with a radial gradient from the center to the periphery of the contact area. Finally, in the dissociation phase of the time course, the fluorescence intensities at the center and periphery rapidly merged and decayed exponentially. When PI 3-kinase was activated maximally, as in Figure 3.1 with PDGF-BB at 0.5 nM or above, the association kinetics were generally marked by two other features. First, the normalized fluorescence at the center exhibits a transient dip, passing through a minimum defined as $f_{min}(0)$; based on the definition of f (Equation 3.2), this value can be negative if a significant amount of cytosolic GFP-AktPH is recruited to the top of the cell before significant diffusion of 3' PIs to the bottom domain can occur. Second, the fluorescence profile approaches a steady state within 5 minutes, characterized by center, periphery, and average fluorescence values denoted $f_{ss}(0)$, $f_{ss}(1)$, and $f_{avg,SS}$, respectively.

3.4.2 Consumption of 3' phosphoinositides is not modulated by PDGF receptor signaling

The dissociation phase in our experiments allowed us to focus on the processes that consume 3' PIs in the plasma membrane. Given the apparent prelocalization of GFP-AktPH prior to stimulation in our cells, we were thus able to address whether 3' PI consumption is under control of the PDGF receptor (Figure 3.2). Thus, in 97 experiments performed on 20 different days, the concentration of PDGF-BB added during the association phase was systematically varied over a range of 0 – 10 nM. Even in the absence of PDGF stimulation, the consumption of the basal 3' PI level could be detected after addition of wortmannin (Fig. 3.2a).

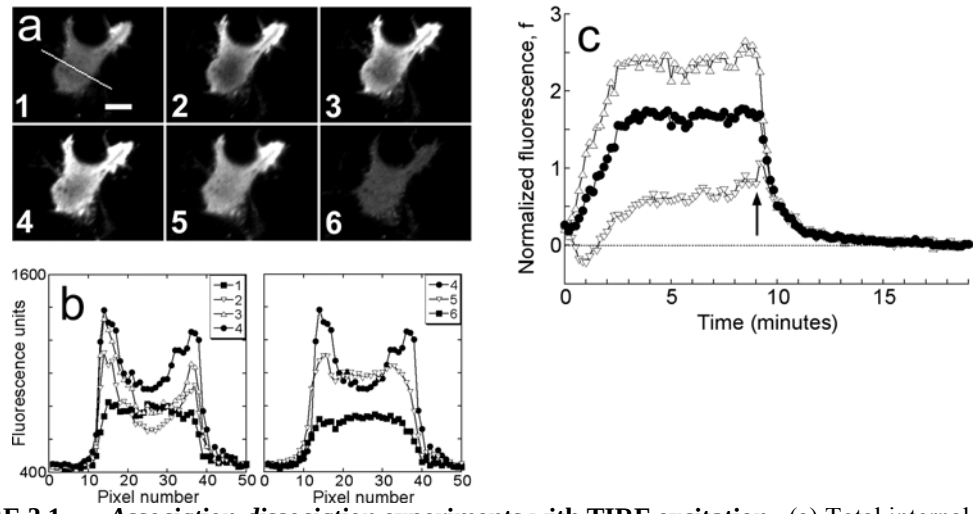

FIGURE 3.1 ***Association-dissociation*** **experiments with TIRF excitation.** (a) Total internal reflection fluorescence (TIRF) images of a representative GFP-AktPH-transfected NIH 3T3 fibroblast. Panel 1 shows the cell prior to treatment (scale bar = 10 μm); the line scan used to generate the data is also shown. Panels 2, 3, and 4 were acquired 1, 2, and 7 minutes after addition of 10 nM PDGF-BB, over which time the fluorescence profile achieved a steady state. Panels 5 and 6 were acquired 0.5 and 10 minutes after addition of wortmannin, which rapidly blocks 3' PI production. (b) Raw fluorescence profiles across the line scan are shown for each of the 6 images in (a). (c) The line scan profiles at all time points, acquired every 10 seconds, were converted into normalized kinetic traces as described under *Materials and Methods*: open triangles, contact area periphery $f(1,t)$; open inverted triangles, contact area center $f(0,t)$; closed circles, contact area average $f_{avg}(t)$. Time zero corresponds to the addition of PDGF, and the arrow signifies the addition of wortmannin.

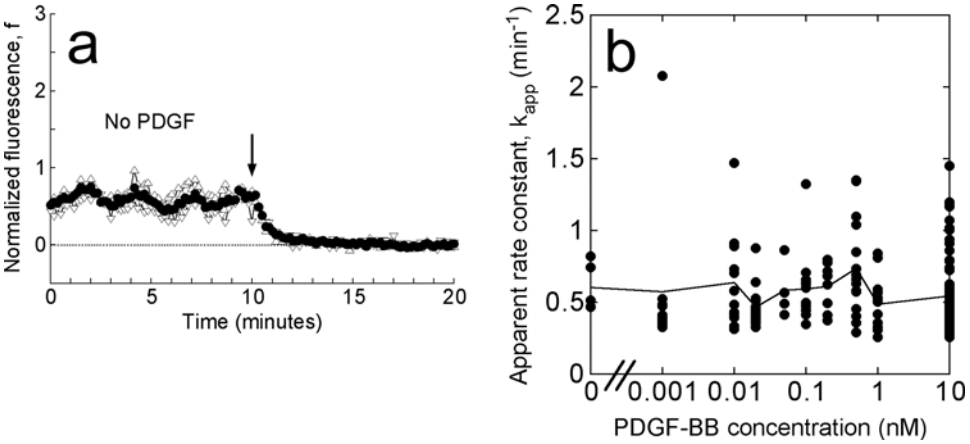

FIGURE 3.2 **The apparent 3' PI turnover rate constant is not altered by PDGF signaling.** (a) Representative association-dissociation experiment with no PDGF added during the association phase, demonstrating that the decay of the basal 3' PI level could be detected in our assay. Symbols are as in Fig. 1c, and the arrow signifies the addition of wortmannin. (b) For each of 197 cells stimulated with various concentrations of PDGF-BB, the time course of the average fluorescence was fit to Equation 3.3, and the apparent 3' PI turnover rate constant, k_{app}, was accepted if the fit exhibited a R^2 value exceeding 0.95. Circle symbols are k_{app} values for 168 individual cells, plotted as a function of the PDGF-BB concentration used in the association phase. The solid line connects the means at each PDGF-BB dose.

Kinetic traces were analyzed for all fluorescent regions of interest that met the following objective criteria: 1) a continuous contact area greater than 300 μm^2, completely in the field of view and not obscured by other fluorescent cells; 2) an average fluorescence 150 intensity units above the acellular background at the end of the dissociation; and 3) fluorescence below the saturation level of the CCD at all times. A significant fraction of the regions of interest were too dim to satisfy the second criterion, and such cells tended to exhibit noisy kinetic traces in the normalized data. Thus, applying these criteria to a total of over 700 regions of interest yielded 197 cells for further analysis.

The average fluorescence for each of these cells was fit to a single exponential:

$$f_{avg}(t) = A\exp(-k_{app}t) \qquad (3.3).$$

Cells were judged to have adequately fit this simple expression with R^2 values exceeding 0.95; 168 out of 197 cells, or 85%, met this standard. Figure 3.2b shows the values of the apparent 3' PI turnover rate constant, k_{app}, as a function of the PDGF concentration during the association period, for each of the 168 cells. The mean value at each concentration, representing multiple fields and days of experiments, is also shown. Cell-to-cell variability was observed as expected, but 89% of the cells exhibited k_{app} values within a factor of 2 of the overall average (0.57 ± 0.29 min^{-1}, mean ± s.d.). Importantly, no significant trend is apparent as the PDGF dose is increased from zero to a saturating dose of 10 nM, indicating that the consumption of 3' PIs is not modulated positively or negatively by the level of PDGF receptor signaling. The 3' PI level stimulated by PDGF is apparently regulated through activation of PI 3-kinases only, and 3' PI consumption may be described mathematically with a pseudo-first order rate constant.

3.4.3 Direct comparison of normalized fluorescence traces and the uniform stimulation model

It has been shown in Chapter 2 that TIRF measurements can be used to calculate ranges of the dimensionless parameters in our uniform stimulation model. Here we wish to apply this strategy to experimental data and obtain the dimensional values of the effective 3'

PI diffusion coefficient and turnover rate constant. When the concentration of PDGF-BB is 0.5 nM or above, neither the magnitude nor the kinetics of the GFP-AktPH association response is sensitive to PDGF concentration ((Haugh et al., 2000) and results not shown). This suggests that PI 3-kinase is rapidly activated under these conditions, such that the model assumption of a step increase in 3' PI production rate is justified. Of the 168 cells discussed in the previous section, 98 saw sufficiently high concentrations of PDGF. To objectively select the best of these cells with which to perform a direct comparison to the uniform stimulation model, additional criteria were imposed. First, a more stringent fluorescence above background cut-off was used (250 intensity units). Of the 71 cells that met that standard, 5 cells were classified as non-responders (with $f_{avg,SS}$ not greater than f_0), and others exhibited no detectable gradient ($f_{ss}(0)$ not less than $f_{avg,SS}$, 9 cells) and/or no dip in the center ($f_{min}(0)$ not less than both f_0 and $f_{ss}(0)$, 27 cells; 6 of these were also among the no gradient cells). With these cells eliminated, 36 cells were identified for the full analysis, of which 32 cells successfully yielded parameter estimates consistent with the uniform stimulation model.

These cells exhibited a range of responses with respect to the depth of the radial gradient that developed during the association phase, as shown in Figure 3.3. In the context of our uniform stimulation model, the depth of the gradient is a strong function of the dimensionless parameter *Da*, which compares the rates of 3' PI consumption and diffusion:

$$Da \equiv kR^2/D\,, \qquad (3.4),$$

where D and k are the effective diffusion coefficient and turnover rate constant of 3' PIs, and R is the radius of the contact area; thus, the depth of the gradient should be sensitive to contact area size. Indeed, the cells with shallower gradients in our experiments (higher $f_{SS}(0)/f_{avg,SS}$) tended to have the smaller effective contact areas and vice-versa (Fig. 3.3a). In the model, the value of *Da* also affects the initial dip in fluorescence at the center of the contact area, and indeed a positive correlation between the values of $f_{SS}(0)/f_{avg,SS}$ and $f_{min}(0)$ was observed in our cells (Fig. 3.3b).

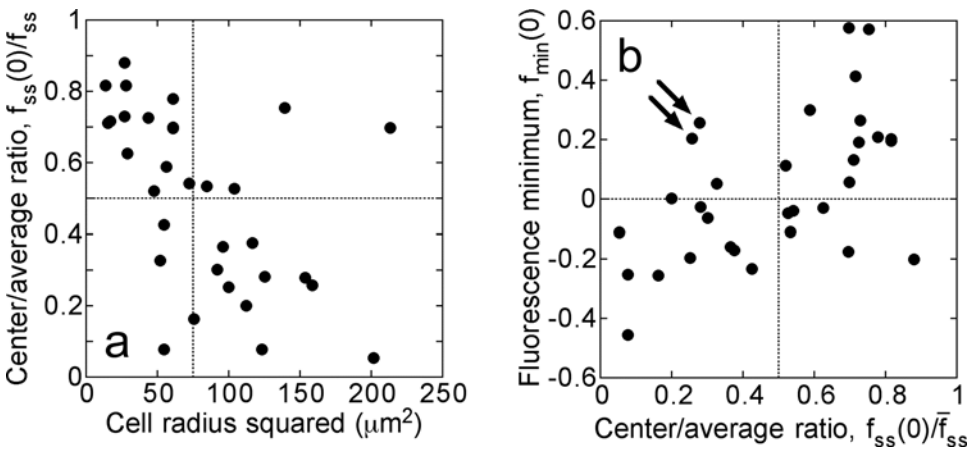

FIGURE 3.3 Fluorescence characteristics of individual cells subjected to the full model analysis. Of the cells imaged in association-dissociation experiments, 32 satisfied all criteria for comparison with model calculations. (a) The gradient depth of each cell, assessed through the steady state center/average fluorescence ratio, $f_{SS}(0)/f_{avg,SS}$, is a function of cell size, measured as the radius of the line scan squared. (b) Correlation of the fluorescence dip at the center of the contact area, $f_{min}(0)$ (y-axis), and the steady state center/average fluorescence ratio, $f_{SS}(0)/f_{avg,SS}$ (x-axis). Two cells with relatively low $f_{SS}(0)/f_{avg,SS}$ yet high $f_{min}(0)$ are indicated with arrows; these are referred to again in Fig. 3.5.

The model was fit to a cell's fluorescence tracks using the following procedure. First, the values of f_0, $f_{min}(0)$, $f_{avg,SS}$, and $f_{ss}(0)$ were estimated from the data. With this information alone, sets of dimensionless parameters (Da, σ, x_0, and p_{ss}) that yield the observed fluorescence characteristics in up to six limiting cases of the uniform stimulation model were identified, as described in Chapter 2. This approach constrains the parameter space and thus delineates the precision of the parameter estimates. Each of the six limiting cases, listed in Table 3.1, was satisfied in a fraction of the cells, and typically a cell satisfied at least three of the cases (Fig. 3.4a); however, as mentioned above, 4 out of the 36 cells selected failed to satisfy any of the cases. With the dimensionless parameters specified, the uniform stimulation model was used to simulate the corresponding association-dissociation experiment for each limiting case in dimensionless time, $\tau = k^*t$. Finally, the simulated kinetics for each case were optimally mapped to real time by least-squares regression of the kinetic traces associated with the center and average fluorescence. Here we allowed the 3' PI production to lag behind the addition of PDGF, and thus the fit yields two parameter values:

the 3' PI consumption rate constant k and the lag time t_{lag}. The sum of the squared residuals, χ^2, divided by the number of data points considered, n, serves as a measure of the quality of

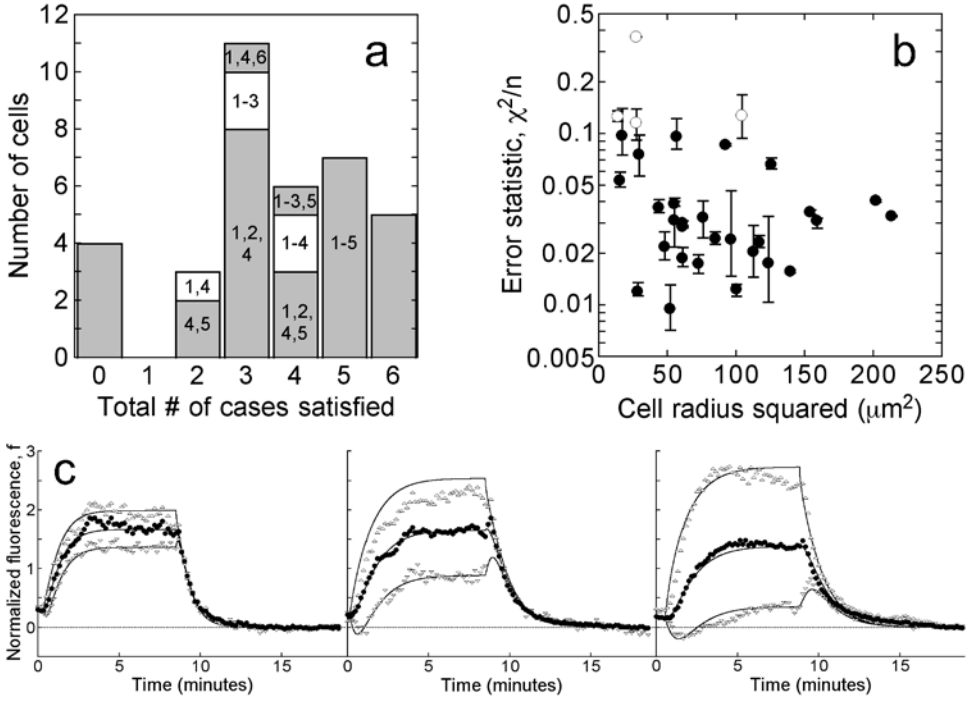

FIGURE 3.4 Model fits to individual cell fluorescence tracks. (a) Limiting cases of the model were used to constrain the parameter space. A histogram for the number of cases (up to 6) satisfied is shown, and the identities of the cases are indicated (see also Table 3.1). (b) The quantity χ^2/n is used to assess quality of fit, where n is the number of data points considered. The χ^2/n value for each cell, averaged over the applicable limiting cases, is plotted *versus* cell size, taken as the square of the line scan radius (μm^2); the error bars signify the range of χ^2/n values obtained. The 4 cells indicated with open symbols yielded the least ideal model fits, with average $\chi^2/n > 0.10$, (c) Representative cell tracks exhibiting radial gradients of varying depth. The values of $f_{SS}(0)/f_{avg,SS}$ are (left) 0.82; (middle) 0.53; and (right) 0.25. Symbols signify fluorescence measurements as in Fig. 3.1c, and solid curves are the best-fit model calculations.

TABLE 3.1 Limiting cases of the uniform stimulation model

Case	*Description* *	*Cells*	*Score* #
1	No 3' PI production in contact area, 3' PI in excess	30	0.96
2	No 3' PI production in contact area, moderate affinity	28	1
3	No 3' PI production in contact area, high affinity	17	0.73
4	Basal 3' PI production in contact area, 3' PI in excess	29	0.83
5	Basal 3' PI production in contact area, moderate affinity	18	0.74
6	Basal 3' PI production in contact area, high affinity	6	0.32

* In terms of the model parameters, no 3' PI production in the contact area means that $\nu = 0$; basal 3' PI production in the contact area means that $\nu = x_0$. 3' PI in excess over the probe refers to $\mu = 5$; moderate or high probe affinity refers to $\kappa = 1 - p_{ss}$ or $\kappa = 10^{-3}$, respectively.

The relative score is calculated by summing $(\chi^2/n)^{-1}$ values of the model fits for that limiting case, and then normalizing by the maximum score (case 2). This score thus rewards a case for the number of cells in which a parameter set was obtained as well as for quality of fit.

fit. The fluorescence at the periphery of the contact area was not included in the fit because small but not insignificant differences between the values at the endpoints of the line scan were typically observed (as in Fig. 3.1b), perhaps suggesting that the periphery is susceptible to subtle edge effects. All but 4 of the 32 cells exhibited average χ^2/n values less than 0.10, and over two-thirds gave average χ^2/n values less than 0.05 (Fig. 3.4b). Although cells with the smallest contact areas were among those giving the poorest fits, the uniform stimulation model performed well on cells exhibiting various depths of the 3' PI gradient (Fig. 3.4c). With k determined by this method for each limiting case, the 3' PI diffusion coefficient D ($\mu m^2/s$) was estimated from the associated value of Da (Equation 3.4), taking the half-width of the line scan as the effective radius of the contact area.

An implicit assumption here is that the effective diffusion coefficient and turnover rate constant in the nonadherent portion of the membrane are the same as in the contact area. The observation that the fluorescence values at the center and periphery of the contact area rapidly merge during the dissociation phase (Fig. 3.1c) indicates that the turnover rate constants in the two domains must indeed be approximately equal as shown in Chapter 2.

3.4.4 Model analysis defines narrow ranges for the 3' PI diffusion coefficient, turnover rate constant, and other parameters in individual cells

Whereas the depth of the radial 3' PI gradient is apparently sensitive to the width of the contact area (Fig. 3.3a), the estimated value of the diffusion coefficient, *D*, is expected to be independent of the contact area size. This was confirmed by plotting the *D* value for each of the 32 cells as a function of the line scan radius squared in Figure 3.5a; each value is reported as the average of the *D* values obtained for the applicable limiting cases of the model, and the range of possible *D* values for each cell and the overall mean (0.37 $\mu m^2/s$) are also indicated on the plot. No apparent correlation was observed over the range of cell sizes. As expected, some cell-to-cell variability in the estimated value of *D* was observed, yet approximately 80% of the cells were within a factor of 2 of the overall mean (Fig. 3.5a). One factor that could influence the degree of variability in the apparent *D* values is deviation of actual contact area morphologies from that of the model; if a cell is long and slender, its *D* value estimated by our method would tend to be underestimated, by as much as a factor of 2 or so. However, the fluorescence pattern emanating from the center of the contact area was reasonably symmetrical in most cells, and the apparent *D* values did not correlate with morphometric quantities such as shape factor or elliptical form factor (results not shown).

Figure 3.5b shows the estimated average value and range of the 3' PI consumption rate constant, *k*, in each of the 32 cells, as correlated with the apparent value of this rate constant, k_{app}, estimated from the single exponential fit (Equation 3.3). The single exponential fit is strongly indicative of the rate constant determined from the more refined model analysis; i.e., low k_{app} values correspond to low *k* values and vice-versa. However, k_{app} was always significantly lower than *k* (Fig. 3.5b). This relationship was also observed when simulated dissociation kinetics, rather than experimental data, were fit to Equation 3.3 (results not shown), and it is attributed to two distinct factors. First, Equation 3.3 assumes a homogeneous 3' PI profile in the contact area, i.e., that the gradient rapidly disappears; this is only approximately true. More significantly, the decay in fluorescence is slower than the decay in 3' PI level when the bound fraction of the probe is appreciable. The fit is affected most by the higher fluorescence values, corresponding to higher fractions of bound probe.

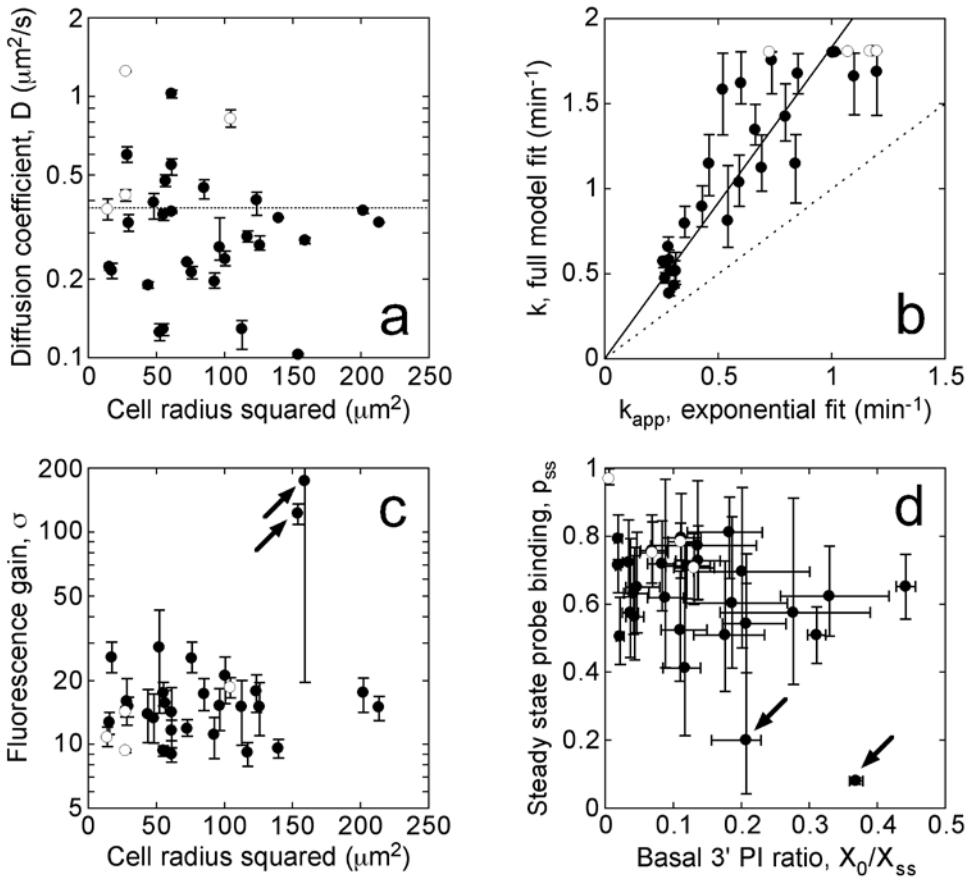

FIGURE 3.5 Estimates of the 3' PI diffusion coefficient, turnover rate constant, and other parameters in individual cells. Circle symbols mark the mean parameter value averaged over the limiting model fits, and the error bars signify the range of parameter values for each cell. Open symbols signify the 4 cells that yielded less ideal model fits as described under Fig. 3.4. (a) The estimated diffusion coefficient D ($\mu m^2/s$) in each cell is plotted *versus* the square of the line scan radius (μm^2), demonstrating that the apparent lipid mobility is independent of cell size. The dotted line indicates the mean of the 32 cells (0.374 $\mu m^2/s$). (b) The average turnover rate constant, k, is correlated *versus* the associated k_{app}, from a fit to Equation 3.3, for each cell. The solid line is the best fit of the data to $y = m*x$, with $m = 1.75$; the dashed line is the $y = x$ line. (c) The fluorescence gain, σ, the ratio of the cytosolic volume to the effective volume of TIRF excitation, is plotted *versus* the square of the line scan radius (μm^2). (d) The estimated values of basal/steady state 3' PI ratio, X_0/X_{ss} (x-axis), and the steady state probe-binding fraction, p_{ss} (y-axis), are shown.

Another parameter is the fluorescence gain σ, which characterizes the physics of TIRF microscopy; its inverse is the fraction of a cell's volume excited by TIRF. Although 2 of the 32 cells exhibited very high apparent σ values (above 100), the remaining cells showed a relatively narrow distribution (15 ± 5, mean ± s.d.) (Fig. 3.5c). As explained in Chapter 2, an arbitrarily high σ value can be obtained when the steady state gradient is moderately steep yet the $f_{min}(0)$ is shallow, and indeed this was the case for the two outlier cells (Fig. 3.3b). A

method for estimating σ independently was also devised, as described in the Appendix C. Applying this method yielded an estimated σ value of 17.5 ± 5.5 (mean ± s.d.), in approximate agreement with the range of values estimated from our model analysis.

The two remaining parameters are X_0/X_{ss}, the basal 3' PI level relative to the maximum, steady state level (in the context of the model, $X_0/X_{ss} = 3x_0/(2 + \nu)$), and p_{ss}, the fraction of GFP-AktPH associated with the membrane at steady state (Fig. 3.5d). The value of X_0/X_{ss} was relatively difficult to determine precisely in each cell, and its estimated value varied widely among cells (0.14 ± 0.11). With that said, the values of X_0/X_{ss} are in rough agreement with biochemical measurements with PDGF-stimulated Swiss 3T3 fibroblasts, in which the levels of PtdIns(3,4,5)P_3 and PtdIns(3,4)P_2 were found to increase approximately 8-fold and 4-fold, respectively (Jackson et al., 1992). The value of p_{ss} was also difficult to estimate precisely, yet the analysis consistently predicted that at least 40% of the probe was recruited to the membrane at steady state (Fig. 3.5d). The two exceptions were the cells that also yielded the arbitrarily high σ values (Fig. 3.5c). The estimated parameter values from the model analysis are summarized in Table 3.2. Each parameter showed varying degrees of cell-to-cell variability, as assessed by the standard deviation of the value, and precision, as judged by the % difference between the minimum and maximum values estimated for each cell (reported as the median of all cells).

TABLE 3.2 Summary of parameter values estimated from model analysis

Parameter	*Description*	*Value **	*% Difference* [#]
D	3' PI diffusion coefficient	0.37 ± 0.25 $\mu m^2/s$	11%
K	3' PI turnover rate constant	1.18 ± 0.54 min^{-1}	18%
t_{lag}	Lag in PI 3-kinase activation	42 ± 35 s	47%
X_0/X_{ss}	Basal/steady state 3' PI ratio	0.14 ± 0.11	53%
σ	Fluorescence gain parameter	15.3 ± 5.0 [&]	30% [&]
p_{ss}	Fraction of probe bound	0.67 ± 0.12 [&]	37% [&]

* Parameter values obtained with the applicable limiting constraints (up to six) for each cell were averaged, and the value reported is the average over all cells analyzed (mean ± s.d.). The standard deviation of this value is thus a measure of cell-to-cell variability.

[#] The % difference between the maximum and minimum parameter values obtained from the applicable limiting cases was calculated for each cell. Given is the median % difference for the cells analyzed, a measure of the precision in the parameter value.

[&] 2 out of 32 cells, yielding both arbitrarily high average σ values (175 and 123) and arbitrarily low p_{ss} values (0.20 and 0.082), were excluded from these statistics; the next highest average σ value was 29, and the next lowest average p_{ss} was 0.41.

3.5 DISCUSSION

The use of green fluorescent protein fusion constructs to probe the spatial regulation and kinetics of intracellular processes is now commonplace (Lippincott-Schwartz et al., 2001; Tavaré et al., 2001; Wouters et al., 2001; Meyer and Teruel, 2003; Weijer, 2003). Quantitative modeling can be applied to directly interpret such experiments and evaluate the roles of various intracellular processes (Slepchenko et al., 2002), and here we have presented a systematic modeling and experimental approach to the analysis of radial 3' PI gradients, typically observed in response to PDGF stimulation of GFP-AktPH-transfected NIH 3T3 fibroblasts (Haugh et al., 2000). Why is the modeling component so important? One major reason is that the fluorescence intensity at a location, indicative of the number of probe-target molecule complexes, very rarely changes in direct proportion to the total number of target molecules. Such proportionality is approximately true only when the fraction of probe molecules bound is small, in which case changes in probe recruitment would be difficult to measure. Indeed, in the majority of the cells we analyzed, it was estimated that greater than 50% of the GFP-AktPH was recruited from the cytosol at steady state (Fig. 3.5d). The model was successful in identifying narrow ranges for the 3' PI diffusion coefficient (D) and turnover rate constant (k); had a simpler analysis been performed, e.g. using a single exponential fit to estimate k, and obtaining Da directly from the depth of the steady state gradient (assuming infinite σ), both k and D would have been grossly underestimated.

Other parameters such as X_0/X_{ss} and p_{ss} were difficult to evaluate precisely in each cell, as their estimated values depend greatly on the limiting case of the model. We observed that cases 1 & 2 outperformed the others based on their applicability and quality of fit (Table 3.1); these cases assume that the PI 3-kinase activity acting at the contact area vanishes upon maximal PDGF stimulation, and that at least half of the 3' PI is not bound by the GFP-AktPH probe. These assumptions are plausible on two grounds. First, 3' PI production is maximal at 0.5 nM PDGF-BB, yet this concentration elicits only half-maximal PDGF receptor phosphorylation in our cells; this suggests that PI 3-kinase molecules are limiting (Park et al., 2003). Second, if a significant fraction of the 3' PI was bound by the probe, one would expect the probe to exert a dominant-negative effect on 3' PI-dependent processes. We presume then that the probe would be toxic to cells expressing very high levels of GFP-

AktPH. Indeed, the brightest cells we observed tended to exhibit altered contact area morphology (results not shown), although we cannot say conclusively that this is caused by 3' PI buffering. When the individual cell parameter estimates were restricted to cases 1 & 2, the range for each parameter value was predictably much smaller (median of 20% difference or less for all parameters), while the means and standard deviations of the parameter values were not grossly altered from those listed in Table 3.2.

An intriguing although not unexpected finding from our quantitative analysis is that individual cells can vary significantly with respect to their estimated parameter values. Insofar as these parameters affect the ability of a cell to sense a PDGF gradient and engage in biased migration, certain cells in the population may be more sensitive than others to gradient stimulation. Variability in the values of D, k, and X_0/X_{ss} may reflect intrinsic differences in the apparent membrane fluidity of cells as well as their relative expression levels of PDGF receptors, PI 3-kinases, and PI 3-phosphatases. The size and morphology of the cell contact area, relative to the orientation of the gradient, also affects the ability of a cell to localize 3' PIs, but this situation can change dynamically on the time scale of minutes as cells actively spread in response to PDGF. It is therefore tempting to speculate that individual fibroblasts may be selectively screened to determine which are recruited to sites of PDGF secretion, such as clotted wounds.

Recently, the spatial sensing problem has been the subject of a number of elegant theoretical investigations (Meinhardt, 1999; Narang et al., 2001; Postma and Van Haastert, 2001; Levchenko and Iglesias, 2002), in which it has been important to compare the cellular responses to uniform and gradient stimulation. However, it should be noted that these modeling studies were not based on a direct comparison with experiment. Our work is a departure from those studies in another major way: the previous models have sought to explain specific phenomenological features of spatial sensing mediated by certain G protein-coupled receptors, as classically observed in neutrophils and in the slime mold *Dictyostelium discoideum* (Devreotes and Zigmond, 1988). In those systems, as in PDGF-stimulated fibroblasts, it is now well-established that 3' PIs are responsible for coupling the presence of an extracellular gradient to polarized cytoskeletal activity (Chung et al., 2001; Wang et al.,

2002; Weiner, 2002), but it would be premature to expect all aspects of spatial sensing mechanisms to be conserved.

Whereas gradient stimulation elicits persistently localized 3' PI production in all cases, the cell responses to uniform stimulation with PDGF and chemoattractants that act through G protein-coupled receptors are markedly different. The latter stimulate very rapid, transient responses with nearly complete adaptation (Stephens et al., 1991; Parent et al., 1998; Servant et al., 2000). In contrast, biochemical measurements have shown that both PtdIns(3,4,5)P_3 and PtdIns(3,4)P_2 levels in PDGF-stimulated fibroblasts achieve a steady state that is maintained for several minutes (Hawkins et al., 1992; Jackson et al., 1992), in accord with our fluorescence measurements. A proposed mechanism that can simultaneously account for the desensitization of the uniform response and the persistence of the gradient response in neutrophils and *D. discoideum* is the parallel receptor-mediated activation of both 3' PI production and consumption (Levchenko and Iglesias, 2002). In apparent support of the regulation of 3' PI consumption, at least in *D. discoideum*, it was recently shown that localization of the PI 3-phosphatase PTEN is altered in response to gradient versus uniform stimulation (Funamoto et al., 2002; Iijima and Devreotes, 2002).

If this localization indeed signifies receptor regulation of 3' PI consumption rates, then in this respect the PDGF sensing mechanism differs. By applying a sensitive fluorescence technique we detected, for the first time, the consumption of the basal 3' PI level in response to PI 3-kinase inhibition. The apparent turnover rate constant exhibited the same range of values regardless of the concentration of PDGF in our association-dissociation experiments, indicating that 3' PI turnover is not regulated by PDGF receptor signaling (Fig. 3.2). The values obtained were similar to the rate constant previously obtained in a PDGF-stimulated fibroblast line by biochemical measurements (Whiteford et al., 1996). Based on our observation that the radial gradient rapidly disappears following PI 3-kinase inhibition, we may also conclude that the 3' PIs in the nonadherent portion of the membrane also experience the same turnover rate constant. Together with the lack of rapid adaptation in response to uniform PDGF stimulation, this suggests that the spatial regulation of 3' PI distribution in our cells is governed simply by the modulation of PI 3-kinase activity. Thus, as we now characterize the response to gradient PDGF stimulation, we do not necessarily

expect the same mechanisms and assumptions that have been attributed to spatial sensing in other systems to hold.

3.6 REFERENCES

Axelrod D. 2001. Total internal reflection fluorescence microscopy in cell biology. Traffic 2: 764-774.

Chung CY, Funamoto S, Firtel RA. 2001. Signaling pathways controlling cell polarity and chemotaxis. Trends Biochem. Sci. 26: 557-566.

Cullen PJ, Cozier GE, Banting G, Mellor H. 2001. Modular phosphoinositide-binding domains: their role in signalling and membrane trafficking. Curr. Biol. 11: R882-R893.

Devreotes PN, Zigmond SH. 1988. Chemotaxis in eukaryotic cells: a focus on leukocytes and Dictyostelium. Annu. Rev. Cell Biol. 4: 649-686.

Funamoto S, Meili R, Lee S, Parry L, Firtel RA. 2002. Spatial and temporal regulation of 3-phosphoinositides by PI 3-kinase and PTEN mediates chemotaxis. Cell 109: 611-623.

Haugh JM, Codazzi F, Teruel M, Meyer T. 2000. Spatial sensing in fibroblasts mediated by 3' phosphoinositides. J. Cell Biol. 151: 1269-1279.

Hawkins PT, Eguinoa A, Qiu RG, Stokoe D, Cooke FT, Walters R, Wennstrom S, Claesson-Welsh L, Evans T, Symons M, Stephens L. 1995. PDGF stimulates an increase in GTP-Rac via activation of phosphoinositide 3-kinase. Curr. Biol. 5: 393-403.

Hawkins PT, Jackson TR, Stephens LR. 1992. Platelet-derived growth factor stimulates synthesis of PtdIns(3,4,5)P3 by activating a PtdIns(4,5)P2 3-OH kinase. Nature 358: 157-159.

Heldin CH, Westermark B. 1999. Mechanism of action and in vivo role of platelet-derived growth factor. Physiol. Rev. 79: 1283-1316.

Hooshmand-Rad R, Claesson-Welsh L, Wennström S, Yokote K, Siegbahn A, Heldin CH. 1997. Involvement of phosphatidylinositide 3'-kinase and Rac in platelet-derived growth factor-induced actin reorganization and chemotaxis. Exp. Cell Res. 234: 434-441.

Iijima M, Devreotes P. 2002. Tumor suppressor PTEN mediates sensing of chemoattractant gradients. Cell 109: 599-610.

Jackson TR, Stephens LR, Hawkins PT. 1992. Receptor specificity of growth factor-stimulated synthesis of 3-phosphorylated inositol lipids in Swiss 3T3 cells. J. Biol. Chem. 267: 16627-16636.

Kundra V, Escobedo JA, Kazlauskas A, Kim HK, Rhee SG, Williams LT, Zetter BR. 1994. Regulation of chemotaxis by the platelet-derived growth factor receptor-b. Nature 367: 474-476.

Levchenko A, Iglesias PA. 2002. Models of eukaryotic gradient sensing: application to chemotaxis of amoebae and neutrophils. Biophys. J. 82: 50-63.

Lippincott-Schwartz J, Snapp E, Kenworthy A. 2001. Studying protein dynamics in living cells. Nat. Rev. Mol. Cell Biol. 2: 444-456.

Martin P. 1997. Wound healing- aiming for perfect skin regeneration. Science 276: 75-81.

McLaughlin S, Wang JY, Gambhir A, Murray D. 2002. PIP2 and proteins: interactions, organization, and information flow. Annu. Rev. Biophys. Biomolec. Struct. 31: 151-175.

Meinhardt H. 1999. Orientation of chemotactic cells and growth cones: models and mechanisms. J. Cell Sci. 112: 2867-2874.

Meyer T, Teruel MN. 2003. Fluorescence imaging of signaling networks. Trends Cell Biol. 13: 101-106.

Narang A, Subramanian KK, Lauffenburger DA. 2001. A mathematical model for chemoattractant gradient sensing based on receptor-regulated membrane phospholipid signaling dynamics. Ann. Biomed. Eng. 29: 677-691.

Parent CA, Blacklock BJ, Froehlich WM, Murphy DB, Devreotes PN. 1998. G protein signaling events are activated at the leading edge of chemotactic cells. Cell 95: 81-91.

Park CS, Schneider IC, Haugh JM. 2003. Kinetic analysis of platelet-derived growth factor receptor/phosphoinositide 3-kinase/Akt signaling in fibroblasts. J. Biol. Chem. 278: 37064-37072.

Postma M, Van Haastert PJM. 2001. A diffusion-translocation model for gradient sensing by chemotactic cells. Biophys. J. 81: 1314-1323.

Ridley AJ, Paterson HF, Johnston CL, Diekmann D, Hall A. 1992. The small GTP-binding protein rac regulates growth factor-induced membrane ruffling. Cell 70: 401-410.

Schlessinger J. 2000. Cell signaling by receptor tyrosine kinases. Cell 103: 211-225.

Servant G, Weiner OD, Herzmark P, Balla T, Sedat JW, Bourne HR. 2000. Polarization of chemoattractant receptor signaling during neutrophil chemotaxis. Science 287: 1037-1040.

Slepchenko BM, Schaff JC, Carson JH, Loew LM. 2002. Computational cell biology: spatiotemporal simulation of cellular events. Annu. Rev. Biophys. Biomolec. Struct. 31: 423-441.
Stephens LR, Hughes KT, Irvine RF. 1991. Pathway of phosphatidylinositol(3,4,5)-trisphosphate synthesis in activated neutrophils. Nature 351: 33-39.
Steyer JA, Almers W. 2001. A real-time view of life within 100 nm of the plasma membrane. Nat. Rev. Mol. Cell Biol. 2: 268-275.
Tavaré JM, Fletcher LM, Welsh GI. 2001. Using green fluorescent protein to study intracellular signalling. J. Endocrinol. 170: 297-306.
Teruel MN, Blanpied TA, Shen K, Augustine GJ, Meyer T. 1999. A versatile microporation technique for the transfection of cultured CNS neurons. J. Neurosci. Methods 93: 37-48.
Toomre D, Manstein DJ. 2001. Lighting up the cell surface with evanescent wave microscopy. Trends Cell Biol. 11: 298-303.
van der Geer P, Hunter T, Lindberg RA. 1994. Receptor protein-tyrosine kinases and their signal transduction pathways. Annu. Rev. Cell Biol. 10: 251-337.
Vanhaesebroeck B, Waterfield MD. 1999. Signaling by distinct classes of phosphoinositide 3-kinases. Exp. Cell Res. 253: 239-254.
Wang F, Herzmark P, Weiner OD, Srinivasan S, Servant G, Bourne HR. 2002. Lipid products of PI(3)Ks maintain persistent cell polarity and directed motility in neutrophils. Nat. Cell Biol. 4: 513-518.
Weijer CJ. 2003. Visualizing signals moving in cells. Science 300: 96-100.
Weiner OD. 2002. Regulation of cell polarity during eukaryotic chemotaxis: the chemotactic compass. Curr. Opin. Cell Biol. 14: 196-202.
Wennström S, Hawkins P, Cooke F, Hara K, Yonezawa K, Kasuga M, Jackson T, Claesson-Welsh L, Stephens L. 1994a. Activation of phosphoinositide 3-kinase is required for PDGF-stimulated membrane ruffling. Curr. Biol. 4: 385-393.
Wennström S, Siegbahn A, Yokote K, Arvidsson A, Heldin CH, Mori S, Claesson-Welsh L. 1994b. Membrane ruffling and chemotaxis transduced by the PDGF b-receptor require the binding site for phosphatidylinositol 3' kinase. Oncogene 9: 651-660.
Whiteford CC, Best C, Kazlauskas A, Ulug ET. 1996. D-3 phosphoinositide metabolism in cells treated with platelet-derived growth factor. Biochem. J. 319: 851-860.
Wouters FS, Verveer PJ, Bastiaens PIH. 2001. Imaging biochemistry inside cells. Trends Cell Biol. 11: 203-211.
Wymann M, Arcaro A. 1994. Platelet-derived growth factor-induced phosphatidylinositol 3-kinase activation mediates actin rearrangements in fibroblasts. Biochem. J. 298: 517-520.

Chapter 4

Spatial Analysis of 3' Phosphoinositide Signaling in Living Fibroblasts: III. Influence of Cell Morphology and Morphological Polarity

Adapted from Schneider et al., Biophys. J., 89: 1420-1430 (2005)

4.1 ABSTRACT

Activation of phosphoinositide (PI) 3-kinase is a required signaling pathway in fibroblast migration directed by platelet-derived growth factor (PDGF). The pattern of 3' PI lipids in the plasma membrane, integrating local PI 3-kinase activity as well as 3' PI diffusion and turnover, influences the spatiotemporal regulation of the cytoskeleton. In fibroblasts stimulated uniformly with PDGF, visualized using total internal reflection fluorescence (TIRF) microscopy, we consistently observed localized regions with significantly higher or lower 3' PI levels than adjacent regions (hot and cold spots, respectively). A typical cell contained multiple hot spots, coinciding with apparent leading edge structures, and at most one cold spot at the rear. Using a framework for finite-element modeling with actual cell contact area geometries, we find that although the 3' PI pattern is affected by irregular contact area shape, cell morphology alone cannot explain the presence of hot or cold spots. Our results and analysis instead suggest that these regions reflect different local 3' PI dynamics, specifically through a combination of mechanisms: enhanced PI 3-kinase activity, reduced 3' PI turnover, and possibly slow/constrained 3' PI diffusion. The morphological polarity of the cell may thus bias 3' PI signaling to promote persistent migration in fibroblasts.

4.2 INTRODUCTION

Directed cell migration, or taxis, is an important phenomenon encountered in the innate immune response, wound healing, and other physiological and pathological processes. In wound healing, invasion of fibroblasts into the fibrin clot is significantly accelerated through their ability to sense and migrate towards gradients of soluble platelet-derived growth factor (PDGF), produced by platelets, macrophages, and other cell types in the clot (1,2). PDGF isoforms bind and induce dimerization of specific cell surface receptors, members of the receptor tyrosine kinase family. Dimerized PDGF receptors recruit and activate a host of cytoplasmic signaling proteins and protein complexes (3,4). One such complex, the heterodimeric phosphoinositide (PI) 3-kinase, is robustly activated by PDGF receptors and is an established requirement for membrane motility processes in fibroblasts and other cell/receptor systems (5-10).

Type I PI 3-kinases phosphorylate phosphatidylinositol (PtdIns) (4,5)-bisphosphate [PtdIns(4,5)P2], a lipid found in the inner leaflet of the plasma membrane, on the 3' position of the inositol ring (11,12). The product, PtdIns(3,4,5)P_3, and its derivative PtdIns(3,4)P_2 (collectively referred to as 3' PIs) interact with specific signaling proteins and mediate pathways known to be responsible for modulation of the cytoskeleton, such as activation of the Rho family GTPases Rac and Cdc42 (13,14). Moreover, external chemoattractant gradients elicit polarized 3' PI patterns in numerous cell types, including fibroblasts (8,15,16). Hence, a conceptual model has emerged in which gradient sensing in eukaryotes is based on the spatially localized activation of cell surface receptors and PI 3-kinase and production of 3' PI lipid second messengers (17-19). A prerequisite for spatial gradient sensing is that the range of the second messenger, defined by its relative diffusion and turnover rates, must be sufficiently small relative to cellular dimensions (8,20). To estimate these and other parameters quantitatively for many cells, we previously analyzed the kinetics and pattern of 3' PIs in mouse fibroblasts stimulated uniformly with PDGF (21,22). The restriction of PDGF-stimulated PI 3-kinase activity to the nonadherent portion of the plasma membrane in our cells produces a spatial 3' PI pattern, and the spatiotemporal response was characterized through direct comparison of results obtained from mathematical modeling and

live-cell total internal reflection fluorescence (TIRF) microscopy experiments. The model equations were calculated on a hemispherical surface approximating the cell membrane.

Although this model gave good agreement with measured fluorescence profiles across the center of the contact area, it was anticipated that certain local regions of the membrane might exhibit 3' PI levels that deviate from the model (21). This conjecture was based on our observation that certain localized regions of the contact area show significantly higher or lower fluorescence intensities relative to adjacent regions; such regions are referred to here as *hot spots* or *cold spots*, respectively. It was further recognized that a more realistic model of the cell geometry would be needed to account for the effect of cell shape on the 3' PI pattern in the contact area.

How might such hot and cold spots arise? It is clear that the cytoskeleton is not only a target for receptor-mediated signaling, but also a signaling mediator in its own right. Morphological polarization is a general characteristic of migrating cells and is seen dramatically at the free edges of "wounded" fibroblast monolayers. An actin-rich leading edge is formed, with one or more protruding lamellipodia and long, thin filopodia, accompanied by translocation of the microtubule organizing center and orientation of microtubules towards the leading edge (14,23,24). Fibroblast polarization also enriches 3' PI lipids at the leading edge, in the absence of external stimuli (8). In other cell systems, the cytoskeleton apparently amplifies 3' PI gradients in cells undergoing chemotaxis (25-27). These observations indicate that there is an intrinsic spatial bias, at the level of 3' PI signaling, associated with cell morphological polarity and leading edge dynamics. Indeed, it has been suggested that positive feedback loops, involving PI 3-kinase, Rac/Cdc42, and/or the leading edge cytoskeleton, can give rise to spontaneous polarization (28-32).

In this paper, we address the effects of cell morphology and morphological polarity on the 3' PI pattern observed in PDGF-stimulated fibroblasts and shed light on the mechanisms that give rise to hot and cold spots. First, we describe improvements to our previous analytical approach that allow the numerical solution of model equations in cell contact area morphologies imported from image analysis software. This led to refined estimates of the model parameters, in particular the relative rates of 3' PI turnover and diffusion. Second, in characterizing the hot and cold spots observed in TIRF experiments,

we report that our cells typically exhibit multiple hot spots, associated with leading edge structures, while cold spots are less prevalent and found at the rear of the contact area. Although morphological polarity thus influences the 3' PI pattern, we found that the local morphology of the contact area alone does not explain the presence of hot or cold spots, suggesting that these regions reflect local differences in 3' PI production and/or turnover kinetics. Finally, we present an analysis of the 3' PI accumulation and decay kinetics in hot spots. We find that their apparent kinetics are consistent with a combination of enhanced PI 3-kinase activation, regulation of 3' PI turnover, and/or slow or constrained 3' PI diffusion, suggesting mechanisms by which local 3' PI levels are governed in leading edge structures.

4.3 MATERIALS AND METHODS

4.3.1 cDNA constructs, cell culture, and transfection

The GFP-AktPH construct consists of the specific 3' PI-binding, pleckstrin homology domain of mouse Akt1 attached with a short linker to the C-terminus of enhanced green fluorescent protein (EGFP), made by cloning into BamHI/XbaI of pEGFP-C1 (Clontech, Palo Alto, CA). This insert was also cloned into the same sites of pEYFP-C1 and pECFP-C1 to produce yellow- and cyan-emitting probes, respectively. Membrane-targeted Lyn-CFP contains the palmitoylation sequence from Lyn (33) cloned into pECFP-N1. NIH 3T3 fibroblasts (American Type Culture Collection, Manassas, VA) were subcultured in 10 cm tissue culture dishes using Dulbecco's modified Eagle's medium with 10% fetal bovine serum, 2mM L-glutamine, and the antibiotics penicillin and streptomycin as the growth medium. Unless otherwise noted, all tissue culture reagents were from Invitrogen (Carlsbad, CA). Cells were seeded in growth medium onto 25 mm square glass cover slips, pre-coated with poly-D-lysine, and later transfected with 1-2 μg of the vector(s) indicated using Lipofectamine Plus (Invitrogen). After 24 h, transfected cells were incubated in serum-free Dulbecco's modified Eagle's medium with 2mM L-glutamine, the antibiotics penicillin and streptomycin, and 1 mg/ml fatty acid-free bovine serum albumin (Sigma, St. Louis, MO) for 3-5 h before imaging.

4.3.2 Total internal reflection fluorescence microscopy

Total internal reflection fluorescence (TIRF) microscopy is a mode of live-cell imaging whereby fluorophores in close proximity to the cell-substratum contact area are selectively excited by an evanescent wave, which penetrates a characteristic distance of ~ 100 nm into the cell (34-36). Our prism-based TIRF microscope was described in detail previously (22). Briefly, two laser heads from Melles Griot (Irvine, CA) were used: a tunable wavelength Ar ion laser head, emitting lines of 488 nm (EGFP, 60 mW) or 514 nm (EYFP, 60 mW), and a HeCd laser head, emitting a 442 nm line (ECFP, 120 mW). All lines were used at maximum power, and the measured incidence angle of the reflected beam ranged from 68-69° across experiments. Band-pass emission filters (Chroma, Rockingham, VT) were 480/30 nm for ECFP, 515/30 nm for EGFP, and 535/30 nm for EYFP. Digital

images were acquired using an ORCA ER cooled CCD (Hamamatsu, Bridgewater, NJ) and Metamorph software (Universal Imaging, West Chester, PA). The imaging buffer was composed of 20 mM HEPES pH 7.4, 125 mM NaCl, 5 mM KCl, 1.5 mM MgCl2, 1.5 mM CaCl2, 10 mM glucose, and 2 mg/ml fatty acid-free bovine serum albumin. Fields of cells were visualized at a combined magnification of 25 x or 12.5 x, and TIRF images were acquired with 2 x 2 binning every 10-20 seconds over a 20-30 minute time course. The exposure time x gain setting was fixed at ca. 400 ms for EGFP and EYFP constructs and ca. 2400 ms for ECFP constructs.

4.3.3 Association-dissociation experiments and analysis of fluorescence profiles in cell contact area geometries

In *association-dissociation* experiments, cells transfected with GFP-AktPH or its spectral variants are stimulated with a maximal dose of PDGF-BB (Peprotech, Rocky Hill, NJ) for about 10 minutes, during which an increase in TIRF fluorescence is observed (association). Thereafter, a high concentration of wortmannin (Sigma) or LY294002 (Calbiochem, San Diego, CA) is added to rapidly block the PI 3-kinase activity, isolating the degradation of 3' PI lipids (dissociation). Experiments and image processing were performed as described previously (22).

The normalized fluorescence data from such experiments can be directly compared with a mathematical model that accounts for 3' PI insertion, diffusion, and turnover in the adherent (bottom) and nonadherent (top) portions of the plasma membrane, as well as the binding of the GFP-AktPH probe (see Appendix D). In our previous analytical approach (21), the dimensionless model parameters Da, σ, p_{ss}, and x_0 were estimated directly from four fluorescence metrics: the initial fluorescence (f_0), the extent of the "dip" in fluorescence in the center of the contact area (f_{min}), the steady-state fluorescence value at the center ($f_{ss}(0)$), and the average fluorescence value at steady state ($f_{ave,SS}$). This procedure was previously carried out for six limiting cases of the model that considered the extremes of lipid-probe interaction parameters and top-bottom polarity of 3' PI insertion; the model calculations, assuming a hemispherical cell, were finally fit to the real-time data using two additional parameters: a lag time, t_{lag}, and the degradation rate constant, k (21).

In this work, a two-step approach was adopted. We first assumed a flat, two-sided disk (pancake) morphology for the model cell, for which a closed-form analytical solution was derived (see the Appendix D). The dimensionless parameters (Da, σ, p_{ss}, x_0) determined for the disk model served as initial guesses for the second step, in which model calculations were performed using the actual contact area geometry of each cell. To achieve this, the outline of each cell was imported from a thresholded image into the finite-element modeling package, FEMLAB (Comsol, Burlington, MA). As in the disk model, the nonadherent plasma membrane was assumed to be flat, with the same shape as the contact area, and the 3' PI concentrations and fluxes were matched at all corresponding points along the peripheries of the two domains in FEMLAB. The two-sided disk model was used to confirm the accuracy of the finite-element calculations. It was also confirmed that the mesh, automatically generated by FEMLAB, was sufficiently refined. Model calculations were used to generate stacks of simulated images for sequential association and dissociation kinetics. Identical line scans were taken from both the model and experimental stacks and directly compared; an interpolation macro was written in MATLAB (MathWorks, Natick, MA) to estimate the normalized fluorescence values at the same pixel locations as in the experimental line scan. Finally, the values of Da, σ and x_0 were adjusted in an iterative fashion to match the initial and steady-state fluorescence profiles observed in the association phase of the experiment.

4.3.4 Modeling of hot and cold spot regions

Hot and cold spots were modeled in FEMLAB as small regions at the periphery of the cell (mirrored in both the top and bottom domains) with different properties from the rest of the membrane. The governing equations were solved in dimensionless form, and so the parameter values in these regions are defined relative to their corresponding values in the "bulk" membrane. To be consistent with experimental observations, only the bottom domain of the cell contributes to the average fluorescence value reported for the hot/cold spot.

4.4 RESULTS

4.4.1 Contact area morphology affects the radial pattern of 3' PI lipids in response to PDGF

To assess the effect of cell shape on the calculated 3' PI and fluorescence profiles in our model, we developed protocols for performing finite-element calculations with contact area geometries imported from image analysis software (Figure 4.1). In the previous model, the plasma membrane was approximated as the surface of a hemisphere, with matching boundary conditions at the circular interface joining the adherent and nonadherent membrane domains (21). Another ideal geometry, perhaps more applicable to thinly spread fibroblasts, is the two-sided disk (Fig. 4.1 a). For a circular contact area, these represent two extremes, with the nonadherent membrane comprising two thirds and one half of the total membrane area, respectively. It was postulated, and later confirmed, that this difference does not affect the quality of fit to experimental fluorescence profiles or the estimated values of the two main parameters of interest, the 3' PI diffusion coefficient D and turnover rate constant k (results not shown). Our current model, like the two-sided disk, assumes that the cell is flat but uses the true shape of each cell's contact area (Fig. 4.1 a).

The same cohort of cells analyzed previously (22), for which fluorescence data were already processed, were reanalyzed using the two-sided disk model and the true contact area protocol. For simplicity, the most broadly applicable limiting case (Case 1, with 3' PIs in excess and no 3' PI production in the contact area) was assumed in all calculations. Thus, 33 out of 36 cells yielded dimensionless parameters from both models. A representative comparison of measured and calculated responses to uniform PDGF stimulation, followed by PI 3-kinase inhibition (*association-dissociation* experiment), is shown in Fig. 4.1 b. The two models give comparable fits to the fluorescence profile taken through the center of the contact area, once the dimensionless parameters are adjusted for the true contact area model (Fig. 4.1 c). From these adjustments, we infer the effect of contact area geometry on the parameter estimation.

Of particular interest is the value of the Damköhler number,

$$Da \equiv kL^2/D, \qquad (4.1)$$

where L is the half-width of the contact area where the measured line scan was taken; its value characterizes the spatial range of locally produced 3' PIs (Figure 4.2). When a cell is

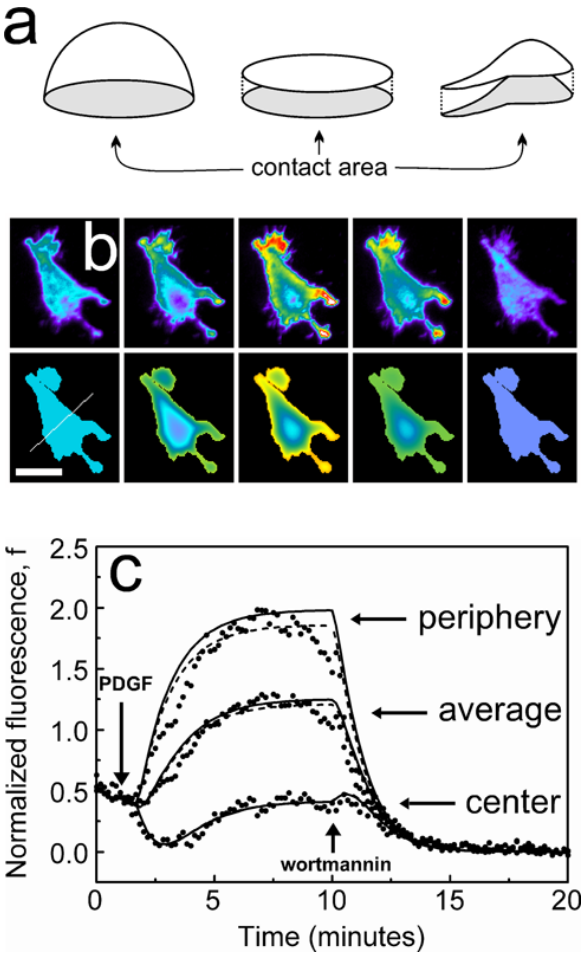

FIGURE 4.1 Calculated 3' PI lipid profiles in response to PDGF stimulation using true contact area geometries. (*a*) Cell geometries considered in our past and present models. From left to right: hemisphere; two-sided disk; true contact area. (*b*) The top row of the montage shows TIRF images of a representative GFP-AktPH-transfected fibroblast in an *association-dissociation* experiment, while the bottom row shows virtual images assembled from corresponding finite-element modeling calculations. The images were taken, from left to right: before stimulation; 2 min. after PDGF addition; 7 min. after PDGF addition (steady state); 0.5 min. after subsequent PI 3-kinase inhibition (5 μM wortmannin); and 10 min. after inhibition (cytosolic fluorescence only). The line in the bottom left panel indicates the fluorescence profile used for model fitting. Scale bar = 20 μm. (*c*) Fit of the two-sided disk model (dashed curves) and true contact area model (solid curves) for the cell depicted in *b*. Dimensionless model parameters Da, σ, x_0, and p_{ss} were estimated for the disk model (7.30, 19.3, 0.0668, and 0.270, respectively) from four fluorescence metrics associated with the center and average fluorescence, taken from the line scan as described under *Materials and Methods*. Based on previous experience, it was assumed that 3' PI is in excess ($\mu = 5$) and that PI 3-kinase is completely recruited to the top of the cell ($\nu = 0$). Da, σ, and x_0 were adjusted to give adequate agreement for the true contact area model (Da = 6.25, $\sigma = 21.5$, $x_0 = 0.0591$). For illustrative purposes, the fit to the entire time course is shown, with a 3' PI turnover rate constant of k = 0.72 min^{-1} in the association phase and a lag time of $t_{lag} = 40$ s.

elongated, the value of Da required to achieve a given gradient depth across the width (short axis) of the cell is lower than that of a circular cell. As expected then, the true contact area model nearly always yielded a lower estimate of Da than the two-sided disk (Fig. 4.2 a), with greater differences at lower Da (shallow gradients). The span of Da values among cells is

largely attributed to variation in cell width. The spatial range, defined as the mean distance traveled by 3' PIs during their lifetime,

$$Range(\mu m) = (4D/k)^{1/2}, \qquad (4.2)$$

varied among cells but over a smaller relative span (Fig. 4.2 b), with a mean ± SD of 12.0 ± 3.7 μm for the true contact area geometry compared with 9.2 ± 3.0 μm for the disk model.

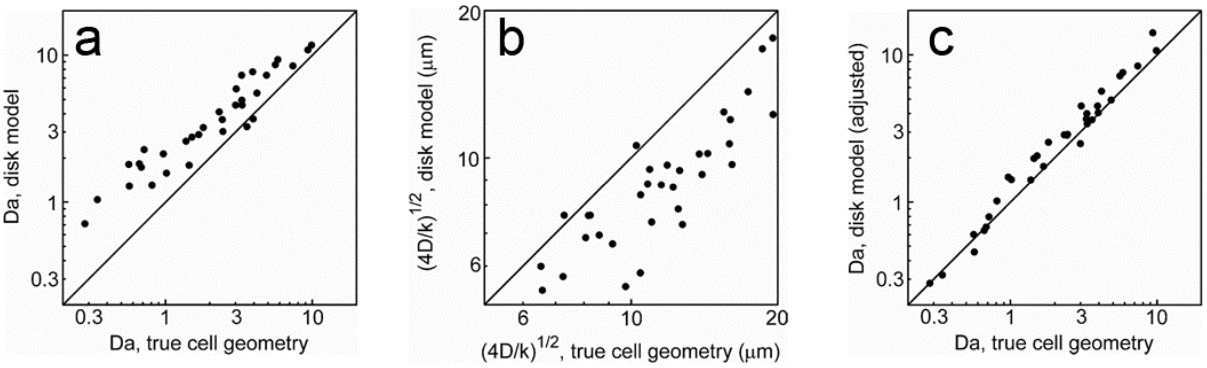

FIGURE 4.2 The assumed geometry of the contact area affects the estimation of *Da*, which compares the rates of 3' PI turnover and diffusion. (*a*) Estimated values of *Da* (Eq. 4.1), from fits to the two-sided disk and true contact area models, are correlated for 33 cells. (*b*) The corresponding correlation of the estimated spatial ranges (Eq. 4.2) from the two models is also shown. (*c*) The *Da* values estimated using the disk model may be adjusted, using 2 x area/perimeter as the relevant length scale, to closely approximate the true contact area model estimate. In each plot, the solid line is $y = x$.

Curious to see if the change in the *Da* estimation could be predicted using a metric that describes the shape of the cell, we adapted the analysis commonly used for estimating diffusion resistance in the rate of reaction observed in porous catalyst particles. For particles of arbitrary shape, the reduction in observed rate is approximately defined by a single parameter, the Thiele modulus $\phi = (V_p/A_p)(k/D)^{1/2}$, where V_p and A_p are the volume and surface area of the particle, respectively (37). In two dimensions, we substitute V_p/A_p with the area/perimeter ratio, which is $R/2$ for a disk. Hence, the *Da* value estimated from the disk model was adjusted by replacing L with 2 x the actual area/perimeter ratio of each contact area, determined from a hand-traced outline of the cell body (excluding thin protrusions). This approach was successful in approximating the *Da* found using the true contact area (Fig. 4.2 c). Consequently, the shape of the cell affects the 3' PI lipid profile, but to a certain degree this change can be predicted using a simple geometric analysis.

4.4.2 Hot and cold spots of 3' PI signaling

From the *association-dissociation* experiments it was apparent that certain contact area regions are significantly more or less fluorescent (by roughly a factor of 2) than neighboring regions. These localized regions of high and low fluorescence, identified by inspection of TIRF images, are termed *hot spots* and *cold spots*, respectively. In all cases, these differences in fluorescence disappeared by the end of the dissociation phase (after PI 3-kinase inhibition). In control experiments with cells expressing soluble ECFP/EYFP or membrane-targeted lyn-CFP, regions with higher or lower fluorescence were seen much less frequently and differed in intensity by ~ 25% or less; the same trends were observed in cells co-transfected with YFP-AktPH/lyn-CFP, YFP-AktPH/ECFP, or CFP-AktPH/EYFP, in which there were no correlations between the two fluorescence channels (data not shown). We conclude that regions of significantly higher or lower GFP-AktPH fluorescence report local differences in the density of 3' PI lipids.

A total of 49 cells transfected with GFP-AktPH were analyzed and found to contain a total of 129 hot spots and 39 cold spots. Fig. 4.3 a, a histogram of the number of hot and cold spots per cell, illustrates that hot spots were much more abundant than cold spots. The vast majority of the cells exhibited at least two hot spots and either zero or one cold spot. Hot spots were generally found around the periphery of the cell (92%) and specifically in areas such as the tips of protruding structures and at leading edges. Nearly half (47%) of the hot spots exhibited noticeably higher than average intensity before the addition of PDGF, and nearly all (97%) maintained a higher fluorescence throughout the PDGF stimulation. Although cold spots were also found around the periphery, there were two distinct types. Most (59%) persisted throughout PDGF stimulation and occurred at the tips of extensions that might be trailing uropodia; these cold spots typically showed minimal response to PDGF during the association-dissociation protocol, but only 17% (n = 4) of them were noticeably cold before stimulation. In the other population (41%), the cold spots were not cold initially or at steady state, but lagged behind the rest of the cell for a certain period following PDGF addition; we refer to this population as transient cold spots.

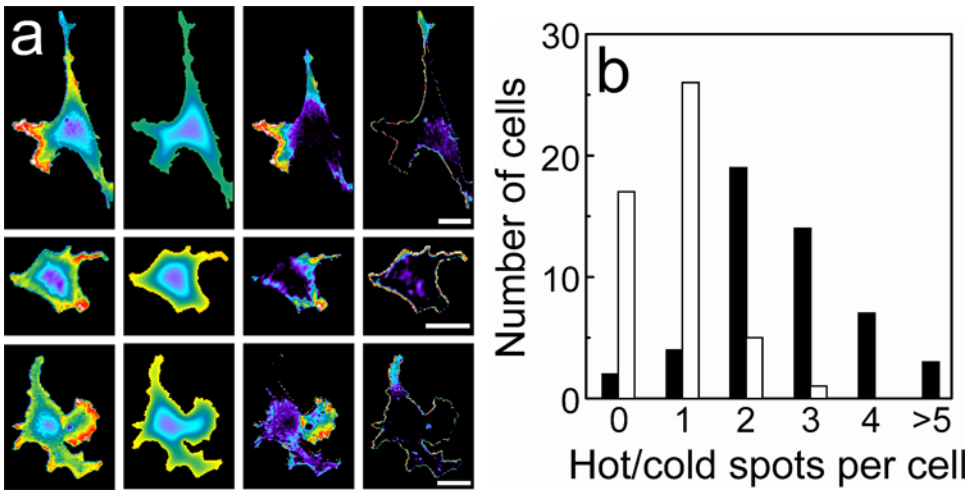

FIGURE 4.3 ***Hot* and *cold spots* of 3' PI signaling.** Hot/cold spots are defined as localized regions in the contact area of a GFP-AktPH-transfected cell with noticeably higher/lower fluorescence than adjacent regions. (*a*) Histogram of the number of hot (black bars) and cold (white bars) spots per cell, recorded for 49 cells. (*b*) Contact area morphology alone cannot account for hot or cold spots. Each row of the montage depicts the steady-state response to PDGF stimulation of a different representative cell. The first column shows the TIRF image, averaged over the time interval used to calculate the steady-state metrics, and the second column shows the virtual image obtained from model calculations as described under Fig. 4.1; these images use the same pseudo-color scale. The third column is the result of subtracting the virtual image from the TIRF image, and the fourth column is the result of subtracting the TIRF image from the virtual image. Scale bars are 20 μm.

Given the effect of contact area morphology on the calculated 3' PI pattern (Fig. 4.1) and the prevalence of hot and cold spots in membrane extensions, we asked whether or not cell shape could explain the presence of apparent hot or cold spots. This possibility was ruled out through a simple analysis. As proven in Appendix D, the uniform stimulation model predicts the same 3' PI level at all points along the cell periphery, regardless of contact area shape. Consequently, higher fluorescence in a thin extension cannot be attributed to geometric effects. Curvature of the nonadherent membrane also cannot explain significant differences in 3' PI level; at steady state, the maximum difference between periphery 3' PI levels in the disk and hemisphere models is ≈ 30% (1/2 versus 2/3); if anything, this would yield slightly lower fluorescence intensities in flat extensions compared to the periphery of the cell body. To illustrate this conclusion, TIRF images and finite-element calculations were compared after maximal PDGF stimulation (Fig. 4.3 b). Subtracting the steady-state model prediction from the TIRF image or vice versa, it is clear that hot and cold spots identified from TIRF images have significantly higher or lower

fluorescence intensities, respectively, than those predicted by the uniform stimulation model. We conclude that hot and cold spots arise from local differences in 3' PI production, turnover, and/or diffusion.

4.4.3 Hot and cold spots exhibit distinct kinetics in association-dissociation experiments

The kinetics of the hot and cold spot responses to the association-dissociation protocol were also characterized (Figure 4.4). A predominant characteristic of hot spots in this regard was a sluggish response compared with the rest of the cell (Fig. 4.4 a & c). Specifically, in the association phase of the experiment, such a hot spot exhibits a slower approach to the steady state; its fluorescence intensity continues to increase after the fluorescence profile in the cell body has apparently settled upon a pseudo- steady state. Further, during the dissociation phase, while the fluorescence profile in the cell body rapidly becomes homogeneous as it decays (22), the fluorescence intensity of the hot spot fails to converge with that of the cell body until all of the 3' PI is consumed (Fig. 4.4 a & c).

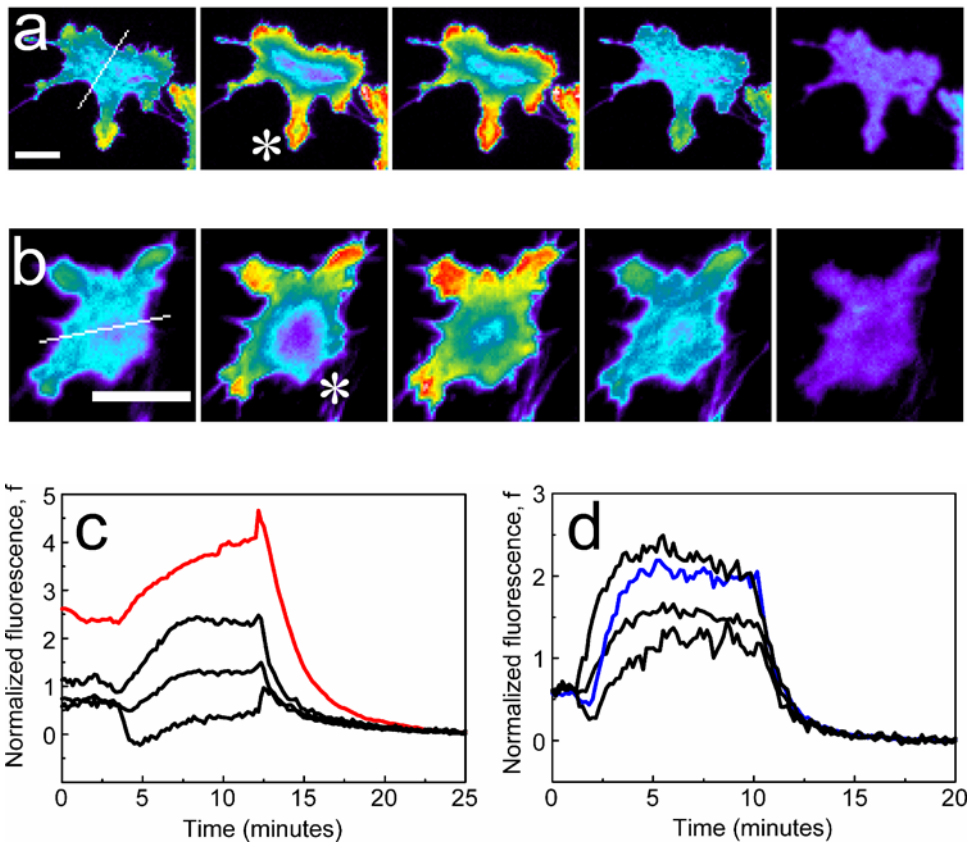

FIGURE 4.4 Characteristic response kinetics of *hot* and transient *cold spots*. TIRF images and time courses of representative hot (*a* & *c*) and cold (*b* & *d*) spots (denoted by the asterisks in *a* & *b*) in association-dissociation experiments. (*a*) The images were taken, from left to right: before PDGF addition; after PDGF stimulation, with the cell body at pseudo-steady state but the hot spot still increasing in intensity; at steady-state; after wortmannin addition, with the cell body more or less uniform but the hot spot decay lagging; and after complete fluorescence decay. Scale bar = 20 μm. (*b*) The images were taken, from left to right: before PDGF addition; after stimulation, when the cold spot is apparent; at steady state; after wortmannin addition, with the cold spot and the rest of the cell body uniform; and after complete fluorescence decay. Scale bar = 20 μm. (*c*) Hot spot kinetics. The center, average, and periphery fluorescence, associated with the line scan in *a*, are shown as a function of time (black curves) as in Fig. 4.1, along with the fluorescence time course of the hot spot (red curve). (*d*) Transient cold spot kinetics. The center, average, and periphery fluorescence, associated with the line scan in *b*, are shown as a function of time (black curves) as in Fig. 4.1, along with the fluorescence time course of the cold spot (blue curve).

Cold spots came in two varieties, persistent and transient, as noted in the previous section. Whereas persistent cold spots tended to show very little response and thus no discernable kinetic signature, a representative example of the kinetics seen in the transient cold spot population is shown in Fig. 4.4 b & d. Initially, such cold spots appear no less bright than other peripheral regions of the cell body (excluding the obvious hot spots), but shortly after PDGF addition the cold spot is much dimmer than other peripheral areas and in

fact dimmer than it was initially (Fig. 4.4 b). The fluorescence eventually merges with the rest of the cell body at steady state, and in the dissociation phase these regions do not differ from neighboring regions (Fig. 4.4 d). Taken together, we conclude that the kinetic features of certain hot and cold spot responses are different and thus reflect different mechanisms.

Motivated by the prevalence of hot spots in our cells and their unique kinetic features in both phases of the experiment, hot spot responses were further characterized through the following quantitative analysis (Figure 4.5). For each cell, a region at the periphery of the cell body was chosen as a reference. Its decay in normalized fluorescence during the dissociation phase was fit to an appropriate function (which assumes exponential decay of 3' PI concentration and pseudo-equilibrium with the GFP-AktPH probe),

$$f(t) = \frac{d_1 \exp(-t/d_2)}{1 + d_3 \exp(-t/d_2)}, \qquad (4.3)$$

in order to estimate the time $t_{1/2}$ at which the fluorescence had fallen to half of its initial value (in terms of the decay fit parameters, $t_{1/2} = d_2 \ln(2 + d_3)$). At this time, the normalized fluorescence values and rates of fluorescence decay for the reference region and all peripheral hot spots in that cell were estimated by linear regression over a one-minute interval. The value ratio is defined as the normalized fluorescence of a particular hot spot divided by that of the reference region. A value ratio significantly greater than one indicates that the hot spot fluorescence had not yet merged with that of the cell body at $t_{1/2}$. The decay ratio is defined as the specific rate of decay (–slope/value) of the hot spot divided by that of the reference region. A decay ratio equal to or less than one, together with a value ratio significantly greater than one, indicates that the hot spot and reference fluorescence intensities have neither converged nor are in the process of doing so. Based on these criteria, with a reasonable value ratio cutoff of 1.2, 61% of the hot spots failed to converge with the reference region (Fig. 4.5). Further, 48% of these hot spots (or 29% total) decayed at a significantly slower relative rate (decay ratio less than 0.8) than the reference region; this observation will be significant in our subsequent modeling analysis.

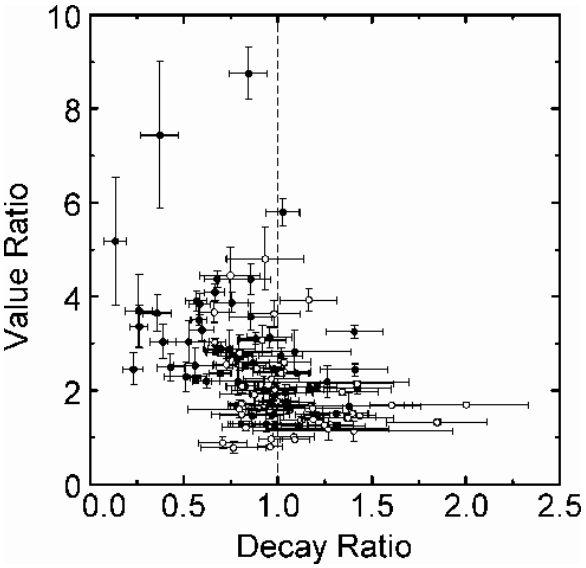

FIGURE 4.5 Quantitative analysis of *hot spot* kinetics. This plot shows quantitative metrics that characterize the fluorescence decay during the dissociation phase in each of the periphery hot spots analyzed (n = 119). In each cell, a reference region at the periphery of the cell body contact area (not a hot or cold spot) was chosen, and the time at which its fluorescence had decayed by 50% ($t_{1/2}$) was estimated (Eq. 4.3). At this time, the normalized fluorescence value and rate of decay for the reference region and all hot spots in that cell were estimated by linear regression over a one-minute interval spanning the $t_{1/2}$ (7 time points, with the midpoint time being the closest to $t_{1/2}$). A hot spot's *value ratio* is defined as its fluorescence at the $t_{1/2}$ divided by that of the reference region, while its *decay ratio* is defined as the specific rate of decay (– slope/value) of the hot spot divided by that of the reference region. A decay ratio equal to or less than one, together with a value ratio significantly greater than one, indicates that the hot spot and reference fluorescence intensities have neither converged nor are in the process of doing so. The error bars were determined by propagation of standard errors. The closed circles indicate hot spots that displayed at least a 20% slower (higher) time constant in the association phase, whereas the open circles indicate hot spots that did not meet this criterion.

The response during the association phase was quantitatively assessed by fitting hot spot and reference region kinetics to single exponentials ($f - f_0 = a_1[1 - \exp(-t/a_2)]$, with t adjusted for the apparent lag time following PDGF addition). 58% of the peripheral hot spots showed slower kinetics in the association phase, as judged by a time constant a_2 at least 20% higher than the corresponding reference region, and the hot spots that showed slower decay ratios in the dissociation phase were much more likely to satisfy this criterion (Fig. 4.5).

4.4.4 Hot spot responses are consistent with a combination of mechanisms: enhanced PI 3-kinase activation, reduced 3' PI turnover, and/or slow or constrained 3' PI diffusion

Given that hot spots arise from local differences in 3' PI production, turnover, and/or diffusion, we sought to elucidate which of these mechanisms are at play. Hot spots consistently showed distinct kinetics in both phases of the experiment, which is significant

because differences found during the dissociation phase can only be attributed to differing rates of 3' PI turnover and/or diffusion. When the turnover rate constant *k* and diffusion coefficient *D* are the same throughout the plasma membrane, the 3' PI density at all points along the contact area periphery decays according to a single exponential (see the Appendix D):

$$x(t) = x(0)e^{-kt}. \qquad (4.4)$$

The 3' PI density at the center of the contact area apparently decays slower because of the net diffusion of lipid from the periphery, until the 3' PI profile in the cell body converges as described in the previous section. Likewise, a region with higher local 3' PI density initially would tend to decay faster as the profile converges. One concludes that the sluggish dissociation responses exhibited by most hot spots reflect a non-homogeneous *k* and/or *D*.

We proceeded to model hot spots simply as defined subcompartments of the membrane with their own values of the model parameters, and analysis of the model led to a number of conclusions (Figure 4.6). First, in hot spots with enhanced PI 3-kinase activity alone (Fig. 4.6 a & d), we expect that the fluorescence intensity would rapidly merge with that of the cell body during the dissociation phase; this is illustrated in Fig. 4.6 d. Second, if enhanced PI 3-kinase activity is coupled with very slow or constrained diffusion in the hot spot, (Fig. 4.6 b & e), its 3' PI density is effectively isolated from the rest of the membrane and thus decays according to Eq. 4.4 during the dissociation phase, at the same relative rate as the rest of the periphery. Thus, in this case the hot spot 3' PI density does not converge with that of the cell body (Fig. 4.6 e). Finally, the 3' PI density also fails to converge in hot spots with normal PI 3-kinase activation and 3' PI diffusion but reduced 3' PI turnover (Fig. 4.6 c & f). Such hot spots would also tend to exhibit a higher local 3' PI density prior to stimulation and a slower approach to the steady state during the association

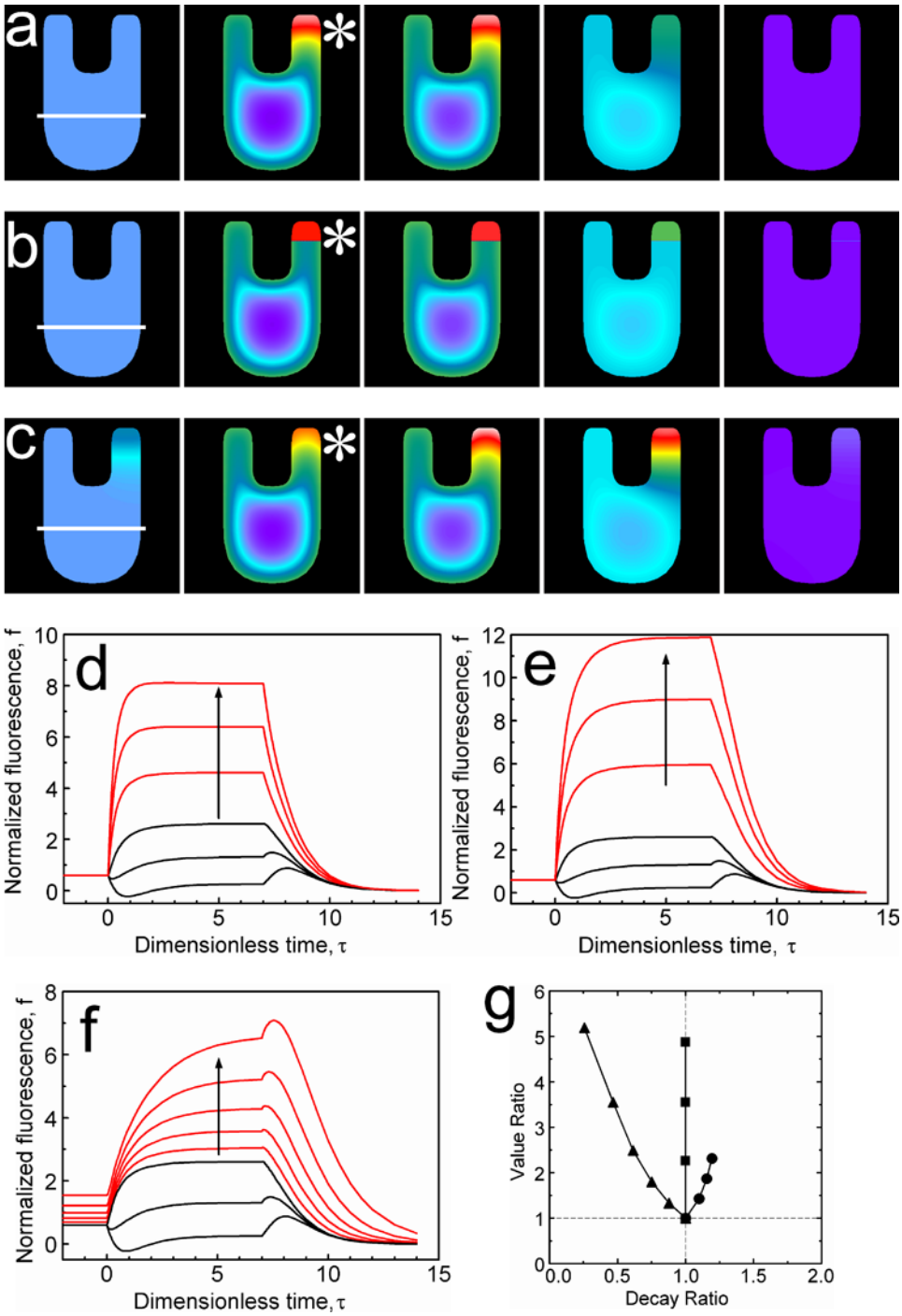

FIGURE 4.6 Analysis of mechanisms that give rise to *hot spots*. (*a* – *c*) The images depict model calculations of a hypothetical association-dissociation experiment and correspond to roughly the same times depicted in Fig. 4.4 *a*, with $\tau = kt = 0$, 2, 7 (just before PI 3-kinase inhibition), 8, and 14 from left to right. Model parameters in the cell body are $Da = 6$, $\sigma = 10$, $x_0 = 0.05$, $\nu = 0$, $\kappa = 2$, $\mu = 5$. For simplicity, a single hot spot with different kinetic properties was placed at the tip of the right pseudopod (in both the contact area and nonadherent membrane), representing approximately 4% of the total membrane area (asterisk). In *a*, the hot spot has enhanced PI 3-kinase activation ($\upsilon_b = \upsilon_t = 1.5$). The hot spot in *b* has enhanced PI 3-kinase activation

($\upsilon_b = \upsilon_t = 1$) and no 3' PI flux between the hot spot and the rest of the membrane (constrained diffusion). In *c*, the 3' PI turnover rate in the hot spot was reduced to zero, but otherwise the region is normal. (*d – f*) The center, average, and periphery fluorescence for the line scans in *a – c* are shown as a function of time (black curves), along with the hot spot fluorescence assuming different parameters (red curves). In *d* & *e*, the hot spot has different 3' PI insertion rates relative to the top of the cell body (1, 1.5, 2 in the direction of the arrows); in *e*, the hot spot is also subject to constrained diffusion as in *b*. In *f*, the hot spot has a different 3' PI turnover rate constant relative to the cell body (0.8, 0.6, 0.4, 0.2, and 0 in the direction of the arrow). (*g*) The hot spots depicted in *d* (enhanced PI 3-kinase, circles), *e* (enhanced PI 3-kinase with constrained diffusion, squares), and *f* (slow turnover, triangles) were subjected to the same analysis as in Fig. 4.5 for comparison.

phase, consistent with the characteristics of a significant fraction of hot spots (Fig. 4.6 f). Of course, these effects would also arise if one assumes local differences in basal PI 3-kinase activity and the kinetics of receptor-stimulated PI 3-kinase activation.

To illustrate the effects of various mechanisms on the quantitative characteristics of fluorescence decay during the dissociation phase, we subjected the model kinetics shown in Fig. 4.6 d–f to the same analysis used in Fig. 4.5 to characterize the experimentally observed kinetics (Fig. 4.6 g). The hot spots with enhanced PI 3-kinase alone have value and decay ratios that are both greater than one by a modest amount, indicative of merging fluorescence values. Either slow/constrained diffusion or reduced turnover is required to produce hot spot decay that fails to merge with the cell body during the dissociation phase (value ratio greater than one and decay ratio less than or equal to one), but a key difference is that these two mechanisms tend to give different relative rates of decay. Slow or constrained diffusion keeps the value ratio high and brings the decay ratio very close to one; as outlined above, the 3' PI level in a hot spot with slow/constrained diffusion and normal turnover decays at the same relative rate (% decrease per unit time) as regions at the periphery of the cell body. Reduced turnover produces a decay ratio significantly less than one and is unique in this respect (Fig. 4.6 g).

In Fig. 4.5, we noted that a significant fraction of hot spots exhibited value ratios greater than 1.2 and decay ratios less than 0.8, an indication of significant reduction in turnover. The fact that these hot spots also showed sluggish association kinetics is consistent with this view. From the spectrum of decay ratios observed, we conclude that hot spots arise from enhanced PI 3-kinase activation as well as reduced 3' PI turnover, perhaps influenced by slow or constrained 3' PI diffusion, although individual hot spots likely differ with respect to the dominant mechanism(s).

4.5 DISCUSSION

Numerous mathematical models have been developed and updated recently to describe eukaryotic spatial sensing phenomena (e.g., 38,39), and quantitative data are being used to inform such models (27). Direct comparison of experiments and models is a critical step towards understanding the signaling mechanisms that govern gradient perception and other intracellular signaling systems (40). We now have a suitable modeling framework that describes uniform PDGF stimulation in fibroblasts, such that its extension to PDGF gradient sensing will be straightforward. By incorporating actual cell morphologies into this model, we have gained insights relevant to both the model implementation as well as the biology of the spatially regulated PI 3-kinase response.

We first employed this framework to more accurately estimate model parameters. Use of idealized, circular contact area geometry is adequate for estimating the spatial range of 3' PIs (Eq. 4.2) within a factor of 2 or so, but it consistently underestimates this quantity. A good compromise for parameter estimation was found in the application of the Thiele modulus, commonly used to analyze diffusion-reaction coupling in heterogeneous catalysis. Although lateral 3' PI diffusion is important for interactions between 3' PI-bound proteins and other membrane-associated components, not to mention its potential role in smoothing out stochastic fluctuations, in this context it is detrimental to the maintenance of long-range 3' PI gradients. As we now apply the finite-element modeling approach to characterize cells responding to PDGF gradients, in which cells vary with respect to their morphology and orientation relative to the PDGF source (Chapter 5), use of the true cell geometry and accurate parameter estimates are vital.

The second motivation for more realistic modeling of contact area geometry was to shed light on the mechanisms that give rise to localized regions with significantly higher or lower fluorescence intensity (hot and cold spots, respectively), observed in peripheral membrane structures that correlated strongly with the cell's morphological polarity. With geometric effects accounted for, we analyzed the hypothetical influences of local differences in PI 3-kinase activation and 3' PI turnover and compared these effects with the kinetics typically observed in response to PDGF. Hot spots, typically found in numerous regions

coinciding with (possibly competing) leading edge structures, were characterized by slower kinetics, exemplified by a dramatic time shift in the fluorescence decay kinetics following PI 3-kinase inhibition. From a quantitative analysis of these kinetics together with model calculations, we concluded that one of the mechanisms contributing to the higher 3' PI densities in hot spots is a local reduction in the rate of 3' PI turnover. Therefore, while pathways and feedback loops affecting PI 3-kinase activity at the leading edge have received considerable attention, we must also consider the local regulation of PI 3-phosphatases or other 3' PI consumption pathways.

A PI 3-phosphatase studied actively in recent years is phosphatase and tensin homologue deleted on chromosome 10 (PTEN). In *Dictyostelium discoideum*, PTEN is localized at the plasma membrane in a reciprocal fashion with respect to PI 3-kinase; i.e., it is membrane-associated prior to stimulation, dissociates transiently in response to uniform chemoattractant stimulation, and is persistently membrane-localized at the rear and sides during chemotaxis (27,41,42). The localization and activity of mammalian PTEN, however, are subject to additional regulatory mechanisms, as implicated by its different domain structure (43). It remains possible, then, that the membrane binding and/or activity of mammalian PTEN or other 3' PI phosphatases may be altered in a highly localized fashion, although the signaling determinants involved are presently uncertain. In our cells, we established previously that 3' PI turnover is not globally regulated in response to PDGF (22), yet such enzymes do appear to be less active in or excluded from certain leading edge locations.

Although hot spots are apparently affected by regulation of 3' PI turnover, we found that enhanced PI 3-kinase activation was also required to explain the degree of 3' PI enrichment in many hot spots. Locally restricted 3' PI diffusion may also be important, as has been implicated in PI 3-kinase-dependent signaling processes driving phagocytosis (44). Incidentally, the less abundant cold spots apparently arise from a lack of PDGF-stimulated PI 3-kinase activation in these regions, or in the case of transient cold spots, a delay in the PI 3-kinase activation kinetics (analysis not shown). Together, these effects are consistent with the notion that leading and trailing edges of the membrane exhibit unique signaling activities and/or present different environments for signaling to take place there.

We have analyzed the apparent relationship between morphological polarity and 3' PI signaling, in the context of both unstimulated and PDGF-stimulated fibroblasts. This relationship leads us to speculate that cell polarity yields an intrinsic bias for directed migration, at the level of the 3' PI pattern, which would either reinforce or antagonize the external bias of a PDGF gradient oriented in a certain direction. This concept is consistent with a model forwarded recently, based on the correlation of spontaneous 3' PI "pulses" at the leading edge with cell turning behavior during random and directed cell migration (45). Obviously, we present here only a snapshot of signaling that occurs during cell movement, which must be integrated with the control of cell polarity, membrane protrusion, and cell adhesiveness.

4.6 REFERENCES

1. Seppä, H., G. Grotendorst, S. Seppä, E. Schiffmann, and G. R. Martin. 1982. Platelet-derived growth factor is chemotactic for fibroblasts. J. Cell Biol. 92:584-588.
2. Pierce, G. F., T. A. Mustoe, B. W. Altrock, T. F. Deuel, and A. Thomason. 1991. Role of platelet-derived growth factor in wound healing. J. Cell. Biochem. 45:319-326.
3. Claesson-Welsh, L. 1994. Platelet-derived growth factor receptor signals. J. Biol. Chem. 269:32023-32026.
4. Heldin, C.-H. and B. Westermark. 1999. Mechanism of action and in vivo role of platelet-derived growth factor. Physiol. Rev. 79:1283-1316.
5. Wennström, S., P. Hawkins, F. Cooke, K. Hara, K. Yonezawa, M. Kasuga, T. Jackson, L. Claesson-Welsh, and L. Stephens. 1994. Activation of phosphoinositide 3-kinase is required for PDGF-stimulated membrane ruffling. Curr. Biol. 4:385-393.
6. Wennström, S., A. Siegbahn, K. Yokote, A. Arvidsson, C.-H. Heldin, S. Mori, and L. Claesson-Welsh. 1994. Membrane ruffling and chemotaxis transduced by the PDGF b-receptor require the binding site for phosphatidylinositol 3' kinase. Oncogene 9:651-660.
7. Kundra, V., J. A. Escobedo, A. Kazlauskas, H. K. Kim, S. G. Rhee, L. T. Williams, and B. R. Zetter. 1994. Regulation of chemotaxis by the platelet-derived growth factor receptor-b. Nature 367:474-476.
8. Haugh, J. M., F. Codazzi, M. Teruel, and T. Meyer. 2000. Spatial sensing in fibroblasts mediated by 3' phosphoinositides. J. Cell Biol. 151:1269-1279.
9. Ridley, A. J. 2001. Rho proteins, PI 3-kinases, and monocyte/macrophage motility. FEBS Lett. 498:168-171.
10. Rameh, L. E. and L. C. Cantley. 1999. The role of phosphoinositide 3-kinase lipid products in cell function. J. Biol. Chem. 274:8347-8350.
11. Fruman, D. A., R. E. Meyers, and L. C. Cantley. 1998. Phosphoinositide kinases. Annu. Rev. Biochem. 67:481-507.
12. Vanhaesebroeck, B., S. J. Leevers, K. Ahmadi, J. Timms, R. Katso, P. C. Driscoll, R. Woscholski, P. J. Parker, and M. D. Waterfield. 2001. Synthesis and function of 3-phosphorylated inositol lipids. Annu. Rev. Biochem. 70:535-602.
13. Nobes, C. D. and A. Hall. 1999. Rho GTPases control polarity, protrusion, and adhesion during cell movement. J. Cell Biol. 144:1235-1244.
14. Ridley, A. J., M. A. Schwartz, K. Burridge, R. A. Firtel, M. H. Ginsberg, G. Borisy, T. J. Parsons, and A. R. Horwitz. 2003. Cell migration: integrating signals from front to back. Science 302:1704-1709.
15. Servant, G., O. D. Weiner, P. Herzmark, T. Balla, J. W. Sedat, and H. R. Bourne. 2000. Polarization of chemoattractant receptor signaling during neutrophil chemotaxis. Science 287:1037-1040.
16. Parent, C. A., B. J. Blacklock, W. M. Froehlich, D. B. Murphy, and P. N. Devreotes. 1998. G protein signaling events are activated at the leading edge of chemotactic cells. Cell 95:81-91.
17. Parent, C. A. and P. N. Devreotes. 1999. A cell's sense of direction. Science 284:765-770.
18. Weiner, O. D. 2002. Regulation of cell polarity during eukaryotic chemotaxis: the chemotactic compass. Curr. Opin. Cell Biol. 14:196-202.
19. Merlot, S. and R. A. Firtel. 2003. Leading the way: directional sensing through phosphatidylinositol 3-kinase and other signaling pathways. J. Cell Sci. 116:3471-3478.
20. Postma, M. and P. J. M. Van Haastert. 2001. A diffusion-translocation model for gradient sensing by chemotactic cells. Biophys. J. 81:1314-1323.
21. Haugh, J. M. and I. C. Schneider. 2004. Spatial analysis of 3' phosphoinositide signaling in living fibroblasts: I. Uniform stimulation model and bounds on dimensionless groups. Biophys. J. 86:589-598.
22. Schneider, I. C. and J. M. Haugh. 2004. Spatial analysis of 3' phosphoinositide signaling in living fibroblasts: II. Parameter estimates for individual cells from experiments. Biophys. J. 86:599-608.
23. Pollard, T. D. and G. G. Borisy. 2003. Cellular motility driven by assembly and disassembly of actin filaments. Cell 112:453-465.
24. Etienne-Manneville, S. 2004. Cdc42 – the centre of polarity. J. Cell Sci. 117:1291-1300.

25. Wang, F., P. Herzmark, O. D. Weiner, S. Srinivasan, G. Servant, and H. R. Bourne. 2002. Lipid products of PI(3)Ks maintain persistent cell polarity and directed motility in neutrophils. Nat. Cell Biol. 4:513-518.
26. Weiner, O. D., G. Servant, M. D. Welch, T. J. Mitchison, J. W. Sedat, and H. R. Bourne. 1999. Spatial control of actin polymerization during neutrophil chemotaxis. Nature Cell Biol. 1:75-81.
27. Janetopoulos, C., L. Ma, P. N. Devreotes, and P. A. Iglesias. 2004. Chemoattractant-induced phosphatidylinositol 3,4,5-trisphosphate accumulation is spatially amplified and adapts, independent of the actin cytoskeleton. Proc. Natl. Acad. Sci. U.S.A. 101:8951-8956.
28. Weiner, O. D., P. O. Neilsen, G. D. Prestwich, M. W. Kirschner, L. C. Cantley, and H. R. Bourne. 2002. A PtdInsP3- and Rho GTPase-mediated positive feedback loop regulates neutrophil polarity. Nat. Cell Biol. 4:509-512.
29. Srinivasan, S., F. Wang, S. Glavas, A. Ott, F. Hofmann, K. Aktories, D. Kalman, and H. R. Bourne. 2003. Rac and Cdc42 play distinct roles in regulating PI(3,4,5)P3 and polarity during neutrophil chemotaxis. J. Cell Biol. 160:375-385.
30. Wedlich-Soldner, R., S. Altschuler, L. Wu, and R. Li. 2003. Spontaneous cell polarization through actomyosin-based delivery of the Cdc42 GTPase. Science 299:1231-1235.
31. Nalbant, P., L. Hodgson, V. Kraynov, A. Toutchkine, and K. M. Hahn. 2004. Activation of endogenous Cdc42 visualized in living cells. Science 305:1615-1619.
32. Postma, M., J. Roelofs, J. Goedhart, H. M. Loovers, A. J. Visser, and P. J. M. Van Haastert. 2004. Sensitization of Dictyostelium chemotaxis by phosphoinositide-3-kinase-mediated self-organizing signalling patches. J. Cell Sci. 117:2925-2035.
33. Teruel, M. N., T. A. Blanpied, K. Shen, G. J. Augustine, and T. Meyer. 1999. A versatile microporation technique for the transfection of cultured CNS neurons. J. Neurosci. Methods 93:37-48.
34. Axelrod, D. 2001. Total internal reflection fluorescence microscopy in cell biology. Traffic 2:764-774.
35. Steyer, J. A. and W. Almers. 2001. A real-time view of life within 100 nm of the plasma membrane. Nat. Rev. Mol. Cell Biol. 2:268-275.
36. Toomre, D. and D. J. Manstein. 2001. Lighting up the cell surface with evanescent wave microscopy. Trends Cell Biol. 11:298-303.
37. Aris, R. 1957. On shape factors for irregular particles — I. The steady state problem. Diffusion and reaction. Chem. Eng. Sci. 6:262-268.
38. Subramanian, K. K. and A. Narang. 2004. A mechanistic model for eukaryotic gradient sensing: spontaneous and induced phosphoinositide polarization. J. Theor. Biol.:49-67.
39. Ma, L., C. Janetopoulos, L. Yang, P. N. Devreotes, and P. A. Iglesias. 2004. Two complementary, local excitation, global inhibition mechanisms acting in parallel can explain the chemoattractant-induced regulation of PI(3,4,5)P3 response in Dictyostelium cells. Biophys. J. 87:3764-3774.
40. Slepchenko, B. M., J. C. Schaff, J. H. Carson, and L. M. Loew. 2002. Computational cell biology: spatiotemporal simulation of cellular events. Annu. Rev. Biophys. Biomolec. Struct. 31:423-441.
41. Iijima, M. and P. Devreotes. 2002. Tumor suppressor PTEN mediates sensing of chemoattractant gradients. Cell 109:599-610.
42. Funamoto, S., R. Meili, S. Lee, L. Parry, and R. A. Firtel. 2002. Spatial and temporal regulation of 3-phosphoinositides by PI 3-kinase and PTEN mediates chemotaxis. Cell 109:611-623.
43. Leslie, N. R. and C. P. Downes. 2004. PTEN function: how normal cells control it and tumour cells lose it. Biochem. J. 382:1-11.
44. Marshall, J. G., J. W. Booth, V. Stambolic, T. Mak, T. Balla, A. D. Schreiber, T. Meyer, and S. Grinstein. 2001. Restricted accumulation of phosphatidylinositol 3-kinase products in a plasmalemmal subdomain during Fc gamma receptor-mediated phagocytosis. J. Cell Biol. 153:1369-1380.
45. Arrieumerlou, C. and M. Meyer. 2005. A local coupling model and compass parameter for eukaryotic chemotaxis. Dev. Cell 8:215-227.

Chapter 5

Quantitative Elucidation of a Distinct Spatial Gradient Sensing Mechanism in Fibroblasts

5.1 ABSTRACT

Migration of eukaryotic cells towards a chemoattractant often relies on their ability to distinguish receptor-mediated signaling at different subcellular locations, a phenomenon known as spatial sensing. A prominent example, seen during wound healing, is fibroblast migration in platelet-derived growth factor (PDGF) gradients. As in the well-characterized chemotactic cells, *Dictyostelium discoideum* and neutrophils, signaling to the cytoskeleton via the phosphoinositide 3-kinase pathway in fibroblasts is spatially polarized by a PDGF gradient; however, the sensitivity of this process and how it is regulated are unknown. Through a quantitative analysis of mathematical models and live-cell total internal reflection fluorescence microscopy experiments, we demonstrate that PDGF detection is governed by mechanisms that are fundamentally distinct from those in *D. discoideum* and neutrophils. Robust PDGF sensing requires steeper gradients and a much narrower range of absolute chemoattractant concentration, consistent with a simpler system lacking the feedback loops that yield signal amplification and adaptation in amoeboid cells.

5.2 INTRODUCTION

Directed cell migration is a critical process in many diverse physiological and pathological settings, such as the immune response, embryogenesis, and tumor metastasis. Chemotaxis, migration biased towards a gradient of soluble chemoattractant, has been studied extensively in the context of two model cell types: neutrophils and the slime mold *Dictyostelium discoideum*[1]. Although these professional migrating cells respond to distinct stimuli, their chemotactic mechanisms exhibit several common features. Their respective chemoattractants bind and activate G-protein-coupled receptors (GPCRs), leading to signal transduction through phosphoinositide (PI) 3-kinase and production of 3' PI lipids in the plasma membrane, a pathway that modulates Rac and Cdc42 GTPases and thus actin-based cell motility[2-5]. In response to spatially uniform stimulation, both cell types exhibit accumulation of 3' PIs and desensitization of this response within seconds[6], often followed by spontaneous polarization of 3' PI signaling and cell motility in a random direction[7-9]. Such adaptation allows these cells to respond definitively to relative changes in chemoattractant concentration. Thus, in response to shallow chemoattractant gradients (~ 1% or greater across the cell), there is a dramatic and persistent spatial polarization of 3' PI signaling and membrane extension in the direction of the gradient[8,10,11], which is sensitive to the relative steepness of the chemoattractant gradient and far less so to its midpoint concentration[12]. These phenomena have in recent years prompted the analysis of these sensitive spatial sensing mechanisms using conceptual[13-15] as well as mathematical[16-21] models, which typically invoke locally activated positive feedback loops and long-range inhibition to simultaneously explain the responses to uniform and gradient stimulation. In the neutrophil system, a Rac-to-PI 3-kinase feedback loop has been identified as a core mechanism in the robust activation of PI 3-kinase and gradient sensing[5,8,22].

Another example of chemotactic sensing is that of dermal fibroblasts in wound healing[23]. Platelet-derived growth factor (PDGF), produced by platelets and macrophages, forms a gradient in the tissue and serves as a potent chemoattractant and mitogen, thus accelerating the rate of fibroblast invasion into the fibrin clot[24,25]. As with the cell types described above, fibroblast motility and PDGF-stimulated chemotaxis rely on the activation

of PI 3-kinase[26-29], and PDGF gradients elicit intracellular 3' PI gradients in the plasma membrane[30]; however, it is currently unknown whether or not there is a common signal transduction mechanism shared by all of these cell types in the regulation of 3' PI-mediated spatial gradient sensing. Indeed, there are indications that the PDGF sensing mechanism differs. Migration of fibroblasts is far slower than that of amoeboid cells and is driven as much by differential adhesion as by membrane protrusion[31], suggesting distinct requirements for gradient sensing. PDGF signals through members of the receptor tyrosine kinase family, which activate different PI 3-kinase isoforms from those activated by GPCRs[32]. Most significantly, it is well established that PI 3-kinase signaling in response to uniform PDGF stimulation is not marked by rapid adaptation; although subject to receptor downregulation on the time scale of hours, 3' PI levels achieve a quasi-steady state after ~ 5–10 min[30,33-35].

In this chapter, we present a quantitative analysis of PDGF gradient sensing in fibroblasts, using a combination of mathematical modeling and live-cell total internal reflection fluorescence (TIRF) imaging. Compared with the chemotactic responses of *D. discoideum* and neutrophils, we report that the PDGF gradient sensing mechanism in fibroblasts is less sensitive and strongly depends on both the relative PDGF gradient and its midpoint concentration. Optimal gradient sensing is observed in a narrow range of intermediate midpoint PDGF concentrations that yield near maximal PDGF receptor-mediated PI 3-kinase recruitment without saturating receptor occupancy. The model quantitatively matches the spatial pattern and kinetics of 3' PI signaling without including positive or negative feedback loops, and accordingly we show that Rho family GTPases are not required for PDGF-stimulated PI 3-kinase activation. These results indicate that although similar pathways are used across diverse cell/receptor systems, the regulatory mechanisms governing the sensitivity of PDGF gradient detection are fundamentally distinct from those characterized for classical, GPCR-mediated chemotactic systems.

5.3 METHODS

5.3.1 Reagents, cDNA constructs, and cell culture

The enhanced green fluorescent protein/Akt1 PH domain construct GFP-AktPH and its cyan and yellow-emitting variants CFP- and YFP-AktPH are as used previously[37,38]. Membrane-targeted Lyn-CFP contains the palmitoylation sequence from Lyn[44] cloned into pECFP-N1. NIH 3T3 fibroblasts (American Type Culture Collection, Manassas, VA) were subcultured, transfected, and serum starved as described[37]. In some cases, cells were treated with *C. difficile* toxin (10 ng/ml; List Biological Laboratories, Inc., Campell, CA) during serum starvation. The imaging buffer was composed of 20 mM HEPES pH 7.4, 125 mM NaCl, 5 mM KCl, 1.5 mM MgCl2, 1.5 mM CaCl2, 10 mM glucose, and 2 mg/ml fatty acid-free bovine serum albumin. Other reagents included PDGF-BB (Peprotech, Rocky Hill, NJ), Oregon Green (OG) 514-dextran (40 kDa; Molecular Probes, Eugene, OR), and wortmannin (Calbiochem, San Diego, CA).

5.3.2 Total internal reflection fluorescence (TIRF) microscopy

TIRF microscopy is a mode of live-cell imaging whereby fluorophores within ~ 100 nm of the membrane contact area are selectively excited[45-47]. Our prism-based TIRF microscope was described previously[37]. Briefly, this system was built around an Axioskop 2 FS (Zeiss, Thornwood, NY) with Achroplan water immersion objectives (20x, 0.5 NA or 40x, 0.8 NA) and a 0.63x camera mount. TIRF excitation was from two laser heads from Melles Griot (Irvine, CA): a tunable wavelength Ar ion laser head, emitting lines of 488 nm (GFP, 60 mW) or 514 nm (YFP/OG 514, 60 mW), and a HeCd laser head, emitting a 442 nm line (CFP, 120 mW). Band-pass emission filters (Chroma, Rockingham, VT) were 480/30 nm (CFP), 515/30 nm (GFP), and 535/30 nm (YFP and OG 514). Digital images were acquired using an ORCA ER cooled CCD (Hamamatsu, Bridgewater, NJ) and Metamorph software (Universal Imaging, West Chester, PA), with 2 x 2 binning and a fixed exposure time x gain setting of ~ 400 ms for GFP, YFP, and OG 514-dextran and ~ 2400 ms for CFP.

PDGF gradients were produced and imaged as follows. A micropipette, pulled to a diameter of ~50 μm and backfilled with a solution of 0-30 nM PDGF and 5μM OG 514-dextran in imaging buffer, was controlled using a syringe pump (World Precision

Instruments, Sarasota, FL) and micromanipulator (Applied Scientific Instrumentation, Eugene, OR). Once a suitable field of cells had been chosen, the pump was set to a flow rate of 30-80 nl/min, and sequential TIRF images of CFP-AktPH and the OG 514-dextran gradient were acquired every 20 seconds. Except where noted otherwise, all experiments were performed at room temperature (26–29 °C). Controls with no PDGF in the tip verified that cells were not stimulated by either the small flow or volume marker.

5.3.3 Gradient-association-dissociation experiments and analysis of fluorescence profiles

In the *gradient-association-dissociation* protocol, cells are stimulated with a PDGF gradient for 20 min, followed by a uniformly saturating PDGF dose (10 nM) for 10 min, after which a high dose of wortmannin (5 μM) is added to rapidly block PI 3-kinase activity. Extensive controls have been described previously[37,38]. The intracellular TIRF above background, F, was normalized by its value at the end of the fluorescence decay, F_{cyt}, to yield the normalized fluorescence, f, as a function of position and time[37]:

$$f = \left(F - F_{cyt}\right) / F_{cyt} . \qquad (5.1)$$

The fractional gradient response, Γ, relates the fluorescence observed after gradient stimulation to the initial, pre-stimulus value and the peak value observed after uniform stimulation (all averaged over 1 minute intervals):

$$\Gamma = \frac{f_{gradient} - f_{initial}}{f_{uniform} - f_{initial}} . \qquad (5.2)$$

Thus, a Γ value of zero indicates that gradient stimulation elicited no change from the initial fluorescence, while a value of one indicates that the fluorescence did not change after addition of 10 nM PDGF. The average response, $\langle\Gamma\rangle$, is defined using whole-cell-averaged f values, while the ability to sense the gradient is quantified as the difference in Γ values between "front" and "back" regions (~ 25 pixels) relative to the gradient ($\Delta\Gamma = \Gamma_f - \Gamma_b$).

The PDGF (ligand) concentration, $[L]$, as a function of position was estimated by assuming that the highest OG 514-dextran TIRF intensity above background, at the point nearest the pipette, corresponds to the concentration of PDGF loaded in the pipette; accordingly, this fluorescence value does not change when the flow rate is increased. At steady state, the relative gradient is insensitive to any (small) difference in diffusion

coefficient between PDGF and OG 514-dextran, and so the proportionality of the two concentrations was assumed at all locations. TIRF excitation of the volume marker is partially occluded by cells; hence, PDGF concentrations at the front and back regions of the cell, $[L]_f$ and $[L]_b$, were estimated as follows. A line scan was drawn through the two regions and extending outside of the cell contact area boundaries. The fluorescence values across this line scan were averaged over the same time interval used to calculate $f_{gradient}$, and PDGF concentrations were estimated by fitting the portions of the line scan outside the contact area to a polynomial (Fig. 5.2 b). The relative PDGF gradient, δ, is defined as

$$\delta = \frac{[L]_f - [L]_b}{[L]_{avg}}; \quad [L]_{avg} = \frac{[L]_f + [L]_b}{2}. \tag{5.3}$$

Cells were chosen for analysis based on the following criteria. At all times, the whole-cell value of F must be at least 250 fluorescence units above background, and the average OG 514-dextran fluorescence around the cell during gradient stimulation must be at least 100 fluorescence units above background. Finally, the cell must show a significant whole-cell response to the uniform stimulation ($f_{uniform} - f_{initial} > 0.3$).

5.3.4 Mathematical model formulation

Here we outline the basic modeling assumptions and methods, which build upon previous work[30,35,37-39]; a more complete description of the model equations and their derivation is provided in Appendix E.

We use two different models to describe activation of PDGF receptors. An experimentally validated kinetic model of PDGF receptor binding, dimerization, and endocytosis as a function of time was given previously[35], to which we have added receptor synthesis and basal turnover. The output of the model is the dimer fraction, d, calculated as a function of time using standard numerical integration. After ~ 5-10 min of PDGF stimulation, PI 3-kinase activation reaches a plateau, for which a simplified, quasi-steady state model is adequate, with

$$d = \frac{d_{\max} u^2}{1 + u + u^2}; \quad u = \frac{[L]}{L^*}. \tag{5.4}$$

The dimensionless PDGF concentration, *u*, is related to the actual PDGF concentration through the scaling constant *L**, the concentration of PDGF that yields one-third maximum receptor phosphorylation. Together, these models accurately and quantitatively describe the kinetics and cooperative dose-response behavior of PDGF receptor phosphorylation in our cells[35].

Receptor-mediated recruitment of PI 3-kinase activity to the plasma membrane depends on both the local and average density of activated receptors, because receptors draw upon a common cytosolic PI 3-kinase pool. Our model is simplified by assuming fast diffusion of PI 3-kinase in the cytosol and pseudo-equilibrium binding with activated receptors. The dimensionless PI 3-kinase (enzyme) recruitment as a function of position, e(ξ) is thus given by

$$e(\xi) = \alpha d(\xi)\left(\frac{1-\langle e\rangle}{\kappa_E + 1 - \langle e\rangle}\right); \qquad \langle e\rangle = \frac{1+\kappa_E+\alpha\langle d\rangle - \sqrt{\left(1+\kappa_E+\alpha\langle d\rangle\right)^2 - 4\alpha\langle d\rangle}}{2} \tag{5.5}$$

The relationship between *e* and *d* is defined by the relative receptor/PI 3-kinase expression ratio, α, and the dimensionless receptor/PI 3-kinase dissociation constant, κ_E; variables in elbow brackets signify spatial averages.

Production of 3' PIs in the membrane is produced locally by receptor-bound enzyme, and there is also a contribution from cytosolic PI 3-kinase, which defines the basal 3' PI level. 3' PI lipids are degraded by a constitutive, first-order mechanism as characterized previously[37].

Spatial modeling, in which the contact area geometry and lateral diffusion of 3' PIs are explicitly considered, was implemented using FEMLAB finite-element modeling software (Comsol, Burlington, MA). The pseudo-steady state receptor activation model (Eq. 5.4) was used in these calculations. The geometry of the cell was constructed as described previously[38], with PI 3-kinase activation in the nonadherent membrane only[30,37]. Normalized fluorescence is calculated by assuming pseudo-equilibrium binding of the GFP-AktPH probe[39]. Additional details are included in the Appendix E.

5.4 RESULTS

5.4.1 Model analysis predicts three concentration regimes of PDGF gradient sensitivity

Faced with the possibility that 3' PI-mediated spatial sensing of PDGF gradients in fibroblasts is governed by a distinct mechanism from those characterized in *D. discoideum* or neutrophils, we formulated a mathematical model based on the simplest possible mechanism (see Methods and Appendix E). Conceptually, our model allows for local activation of PI 3-kinase but not global regulation of PI 3-kinase or 3' PI-consuming enzymes. PI 3-kinase signaling at different locations only affect one another through depletion of a common, cytosolic PI 3-kinase pool and through lateral diffusion of 3' PI lipids, effects which our previous studies suggest are important; the recruitment of PI 3-kinase by PDGF receptors can be saturated at submaximal receptor occupancy[35,36], and the spatial range of 3' PI lipids in PDGF-stimulated fibroblasts (~ 10 μm) is significant compared to cellular dimensions[30,37,38].

From an analysis of the model equations, which relate the difference in PI 3-kinase recruitment between the front and back of the cell (Δe) to the corresponding difference in receptor activation (Δd) at quasi-steady state, one predicts three distinct regimes of gradient sensitivity (Fig. 5.1 a–c). At low midpoint concentrations of PDGF, gradient sensing is absolute:

$$\Delta e \propto \Delta d \qquad \text{(low PDGF)}. \tag{5.6}$$

Receptor dimerization is cooperative with respect to PDGF concentration[35], yielding a modest enhancement of the apparent sensitivity in this regime (less than two-fold). As the concentration of PDGF is increased, overall PI 3-kinase recruitment approaches saturation ($\langle e \rangle \approx 1$). In this regime, activated receptors compete for a limiting pool of PI 3-kinase, such that gradient sensing is relative:

$$\Delta e \approx \Delta d / \langle d \rangle \quad \text{(intermediate PDGF)}. \tag{5.7}$$

At extremely high PDGF concentrations, however, all receptors are saturated with ligand, and the cell is unable to sense the gradient:

$$\Delta e \approx 0 \qquad \text{(high PDGF)}. \tag{5.8}$$

A number of testable predictions emerge from this simple model (Fig. 5.1 a – c), which we will show to be valid in fibroblasts responding to PDGF gradients:

1. The gradient in PI 3-kinase signaling, Δe, is sensitive to both the relative PDGF gradient (defined as δ; Eq. 5.3) and its midpoint concentration, with the greatest sensitivity at intermediate midpoint concentrations.
2. Both the peak value of Δe and the range of midpoint PDGF concentrations that yield robust intracellular 3' PI gradients ($\Delta e > 0.1$, for example) are determined by the degree of PI 3-kinase saturation. Given parameter values consistent with the dose responses of receptor and PI 3-kinase activation measured in our cells[35], the peak $\Delta e \sim \delta$, and the effective range of midpoint PDGF concentrations spans roughly two logs.
3. At intermediate concentrations of PDGF, where the gradient sensitivity is greatest, PI 3-kinase activation at the front of the cell exceeds the level observed under receptor-saturating conditions. Hence, if gradient stimulation is followed by a high, uniform dose of PDGF, PI 3-kinase signaling at the front will be forced to decrease.

A more detailed model, accounting for the kinetics of PDGF receptor binding, dimerization, and internalization, was used to calculate 3' PI levels as a function of time in a typical cell stimulated with various gradients (assumed here to be established immediately at $t = 0$) (Fig. 5.1 d). After 20 min of gradient stimulation, the PDGF concentration is switched to a uniformly saturating value for a period of 10 min, followed finally by rapid inhibition of PI 3-kinase and decay of the 3' PI level. These conditions reflect the protocol used in our experiments, and the calculated kinetics support the predictions of the quasi-steady state model.

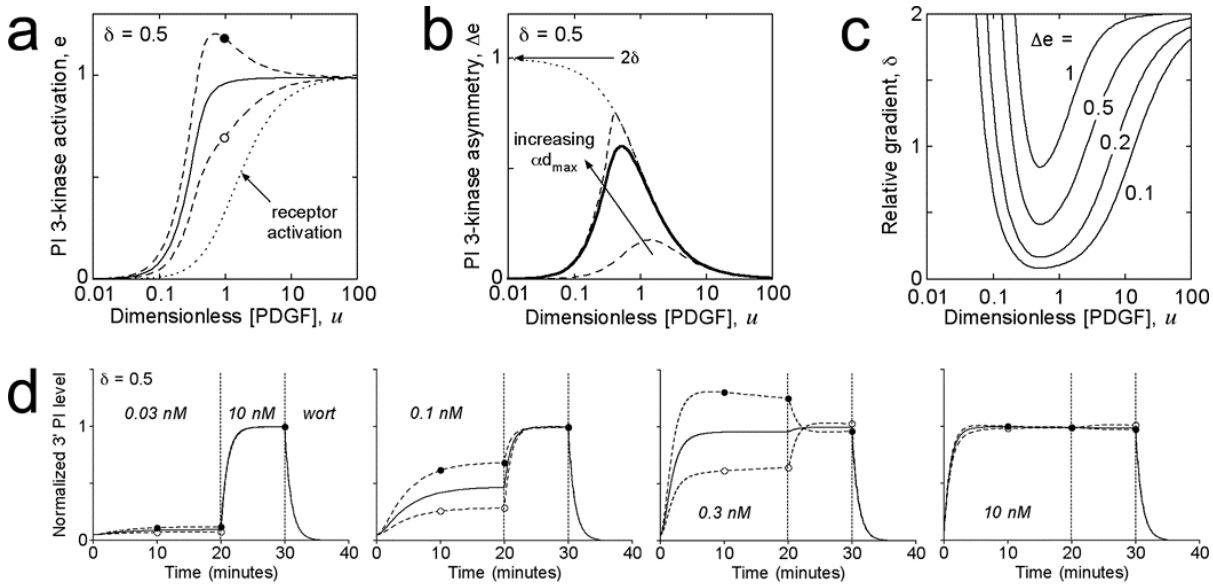

Figure 5.1 Sensitivity of the PDGF gradient sensing mechanism: mathematical modeling predictions. (*a* – *c*) Predictions based on the quasi-steady state model of receptor activation (Eq. 5.4) and pseudo-equilibrium binding of PI 3-kinase (Eq. 5.5). (*a*) Dimensionless PI 3-kinase recruitment, *e*, as a function of midpoint PDGF concentration with a 50% gradient across the cell, at the front (--●--) and back (--○--) relative to the gradient and averaged over the cell membrane (——); $\alpha d_{max} = 10$, $\kappa_E = 0.1$. The receptor activation level, $\langle\Gamma\rangle$, is also shown (·····). (*b*) Difference in *e* between the front and back, Δe, for the parameter values in *a* (solid curve). Also shown are results assuming stoichiometric binding ($\kappa_E = 0$) with αd_{max} values of 1 and 10 (-----), and in the limit of infinite αd_{max} (·····); the latter is equivalent to the relative receptor activation gradient, $\Delta d/\langle d\rangle$. (*c*) Values of the relative gradient, δ, and midpoint PDGF concentration that yield a given Δe; $\alpha d_{max} = 10$, $\kappa_E = 0.1$. (*d*) Front (--●--), back (--○--), and average (——) 3' PI levels were calculated as a function of time using a kinetic receptor activation model (see Appendix E), under conditions that mimic our experimental protocol. A 50% gradient of varying midpoint PDGF concentration, as indicated, was administered for 20 min, followed by a uniformly saturating dose (10 nM) for another 10 min. Thereafter, PI 3-kinase activity was turned off, as if inhibited by wortmannin (wort).

5.4.2 Gradient sensing in fibroblasts is optimized in a relatively narrow range of PDGF concentrations, consistent with saturation of PI 3-kinase recruitment

The CFP-tagged pleckstrin homology domain of Akt (CFP-AktPH) was used as a specific biosensor for 3' PI production at the plasma membrane. Using a micropipette co-loaded with PDGF and a fluorescent volume marker (Oregon green 514-dextran), CFP-AktPH-transfected fibroblasts were presented with gradients of PDGF, and the local marker concentration and intracellular CFP-AktPH translocation were monitored using TIRF microscopy (Fig. 5.2). By varying the concentration of PDGF in the pipette across different experiments and observing cells at different distances from the source, we systematically

analyzed responses to PDGF fields with varying midpoint concentration and gradient steepness. After 20 min of gradient stimulation, a high concentration of PDGF was added uniformly to normalize the response at each location; subsequently, a high concentration of wortmannin was added to rapidly block PI 3-kinase and thus to assess the degradation of 3' PI lipids and the contribution of cytosolic CFP-AktPH to the overall TIRF fluorescence[37,38].

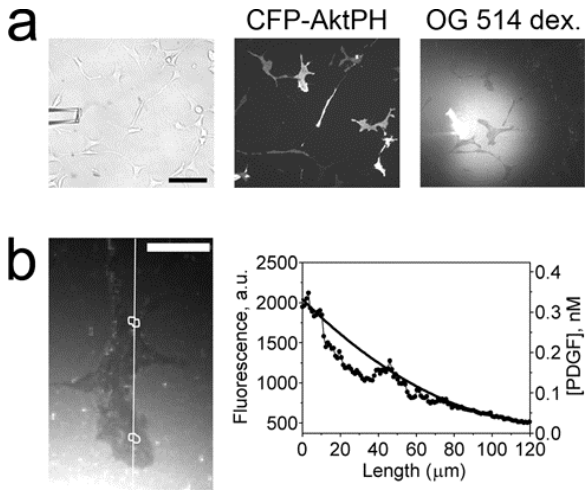

Figure 5.2 TIRF imaging of extracellular and intracellular gradients. (*a*) A micropipette was co-loaded with Oregon green (OG) 514-dextran and a prescribed concentration of PDGF, and PDGF gradients were presented to NIH 3T3 fibroblasts transfected with CFP-AktPH. Scale bar = 100 μm. (*b*) Although the TIRF excitation of the volume marker is partially occluded by the cells[48], the surrounding regions allow the estimation of the PDGF concentration profile across the cell, as described under Methods. Scale bar = 30 μm.

For each cell, regions that define its front and back with respect to the gradient were chosen, and their respective kinetics were assessed. It is important here to distinguish between the cell orientation relative to the gradient and the morphological polarity of the cell established prior to stimulation. Protruding membrane structures at the leading edges tend to be localized hot spots of PI 3-kinase signaling in our cells, with elevated 3' PI levels relative to neighboring regions, while cold spots with depressed 3' PI levels are sometimes observed at the trailing end of the cell. These regions, apparent after the uniformly saturating PDGF stimulation, have been characterized in detail elsewhere[38] and were intentionally avoided in this analysis.

PI 3-kinase signaling responses to PDGF gradients of varying midpoint concentration and steepness were consistent with model predictions (Fig. 5.3). Proper gradient sensing was apparent within a relatively narrow range of PDGF concentration, as PDGF gradients with low midpoint concentrations elicited little change in the TIRF profile, while cells exposed to gradients with very high midpoint concentrations showed little change after the uniform

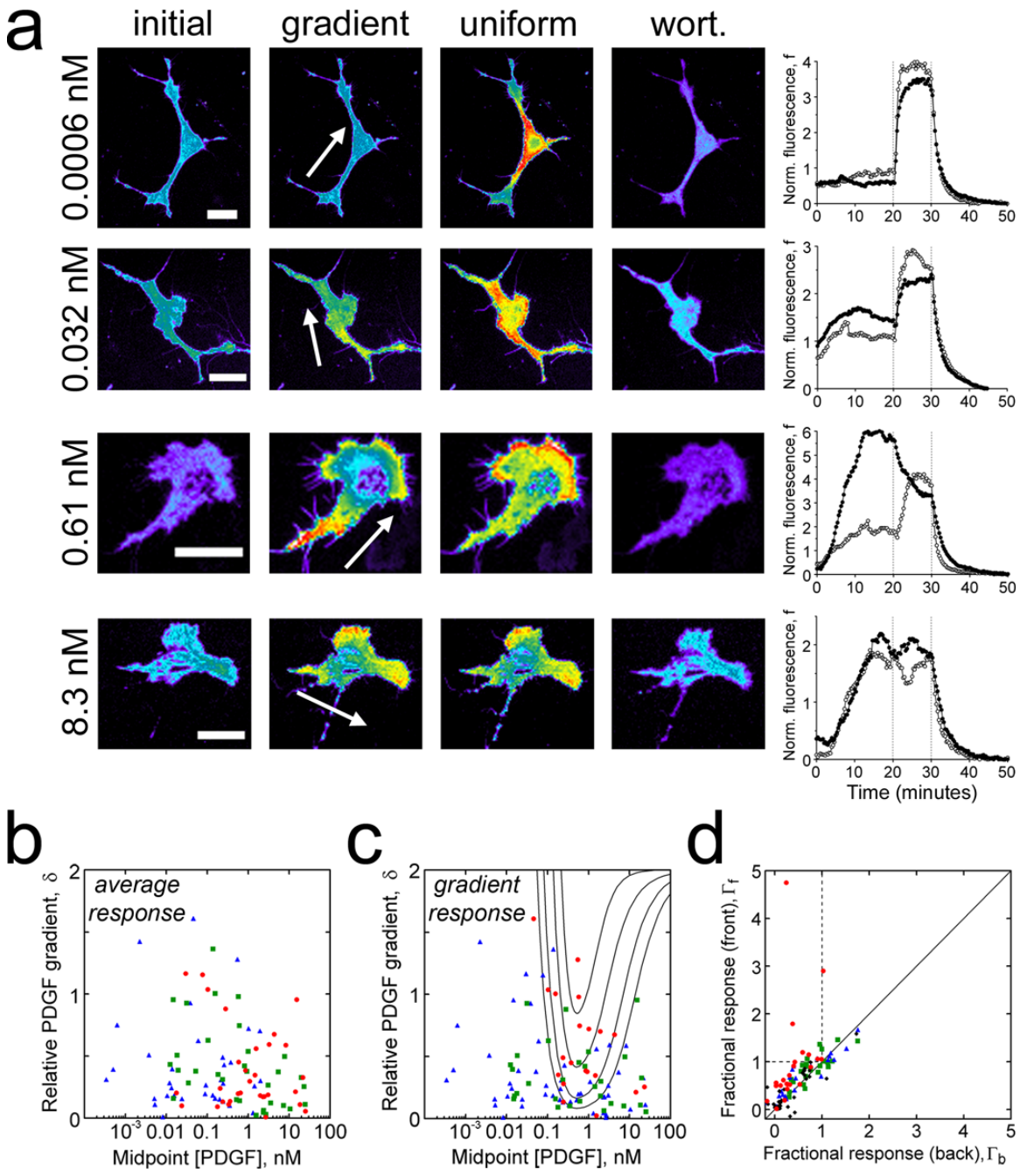

Figure 5.3 Sensitivity of the PDGF gradient sensing mechanism: experimental validation. (*a*) Representative cell responses to steep PDGF gradients with different midpoint concentrations. The montages shows TIRF images acquired pre-stimulus (initial), at the peak of the gradient response, after bolus addition of 10 nM PDGF (uniform), and after PI 3-kinase inhibition with wortmannin (wort). The arrows indicate PDGF gradient orientation from high to low, and the relative gradients δ across these four cells were 0.75, 0.63, 0.75, and 0.59 (from top to bottom). Scale bars = 30 μm. The normalized TIRF intensities at the front (●) and back (○) of each cell with respect to the gradient are shown as a function of time. (*b*) The average responses of individual cells to various gradients tend to increase with midpoint PDGF concentration and are not affected by gradient steepness. Values of ⟨Γ⟩ were classified as low (< 0.3, ▲), intermediate (0.3–0.7, ■), or high (> 0.7,

●). (*c*) The difference in response between the front and back is optimized at intermediate PDGF concentrations and depends on the gradient steepness. Values of ΔΓ were classified as low (< 0.1, ▲), intermediate (0.1–0.3, ■), or high (> 0.3, ●). The quasi-steady state model results from Fig. 5.1 *c*, with $L^* = 1$ nM, is overlaid for comparison. (*d*) Fractional responses at the front and back are plotted for the cells depicted in *b* and *c*, grouped according to the midpoint concentration and steepness of the PDGF gradient: ◆, < 0.1 nM PDGF; ▲, 0.1–2 nM PDGF, δ < 0.3; ●, 0.1–2 nM PDGF, δ > 0.3; ■, > 2 nM PDGF.

stimulus; optimal gradient sensing was often accompanied by a decrease in fluorescence at the front and a corresponding increase at the back following the uniformly saturating dose (Fig. 5.3 a). In all cases, the observed kinetics were consistent with those calculated in Fig. 5.1 d. It should be noted that these experiments were performed at room temperature to inhibit cell motility[30], so that the regions remained stationary during the experiment.

To analyze these responses more quantitatively, we defined the fractional gradient response, Γ, which compares the local TIRF intensity at the height of the gradient response to those recorded before stimulation and after uniform saturation (Eq. 5.2). The whole-cell-averaged response, (⟨Γ⟩), and the difference between front and back regions, ΔΓ, were assessed for a total of 99 cells (Fig. 5.3 b and c, respectively). As expected, higher PDGF concentrations tended to elicit higher average responses, with no apparent dependence on the gradient steepness, although significant cell-to-cell variability in the dose response was also noted (Fig. 5.3 b). In contrast, the greatest front-to-back asymmetry was seen in cells exposed to PDGF gradients with intermediate concentrations and appreciable steepness; an overlay of the results from Fig. 5.1 c shows good correspondence between model and experiment (Fig. 5.3 c). Another way to assess these responses is by plotting the Γ value of the front versus that of the back (Fig. 3 d). Cells exposed to gradients with intermediate concentrations and high steepness were much more likely to lie above the $y = x$ line on this plot, indicative of proper gradient sensing. Significantly, several of these cells populated the upper-left quadrant ($\Gamma_f > 1$, $\Gamma_b < 1$), meaning that the TIRF intensity at the front decreased, and the intensity at the back increased, following the uniform stimulation.

5.4.3 Spatial modeling of gradient responses and comparison with intracellular TIRF profiles

To refine our quasi-steady state model of PDGF gradient sensing, finite-element calculations were performed that allow us to directly compare the predicted fluorescence profile, *f* (Eq. 5.1), with the acquired TIRF images at each point in the contact area[38] (Fig. 5.4). The actual PDGF concentration field and irregular cell geometry are inputs to the model, which accounts for pseudo-steady state receptor and PI 3-kinase activation as well as lateral diffusion of 3' PI lipids and recruitment of the CFP-AktPH probe from the cytosol. Order-of-magnitude estimates of the model parameter values were assigned based on our previous experimental and modeling studies of fibroblast responses to uniform PDGF stimulation[35,37-39], and to approximately match the overall fluorescence intensities observed prior to stimulation and after uniform saturation. No parameters were fit to the gradient response.

The resulting TIRF profiles were compared with experimental images for one of the cells from Fig. 5.3 a exposed to steep PDGF gradients (Fig. 5.4 a–c). Two versions of the model were used; the second, depicted in Fig. 5.4 c, partially accounts for the aforementioned hot spots observed at the cell's pre-existing leading edge, which incidentally is at the "back" of the cell relative to the gradient. Hot spots are modeled simply as regions of the membrane with locally increased PI 3-kinase activity and slower 3' PI diffusion[38]. The hot spots may also respond to lower PDGF concentrations than the rest of the membrane; the average Γ value of the hot spot regions is 0.68, compared with 0.38 for the adjacent region defining the back of the cell. This effect was not included in this model, and consequently the hot spot fluorescence intensities observed in the gradient response are somewhat higher than those predicted by the model. Even with rough parameter estimates and a relatively crude model of the hot spot regions, the agreement between observed and simulated CFP-AktPH translocation patterns is quite close, and the model can readily produce the observed steepness of the intracellular TIRF gradient (Fig. 5.4 d).

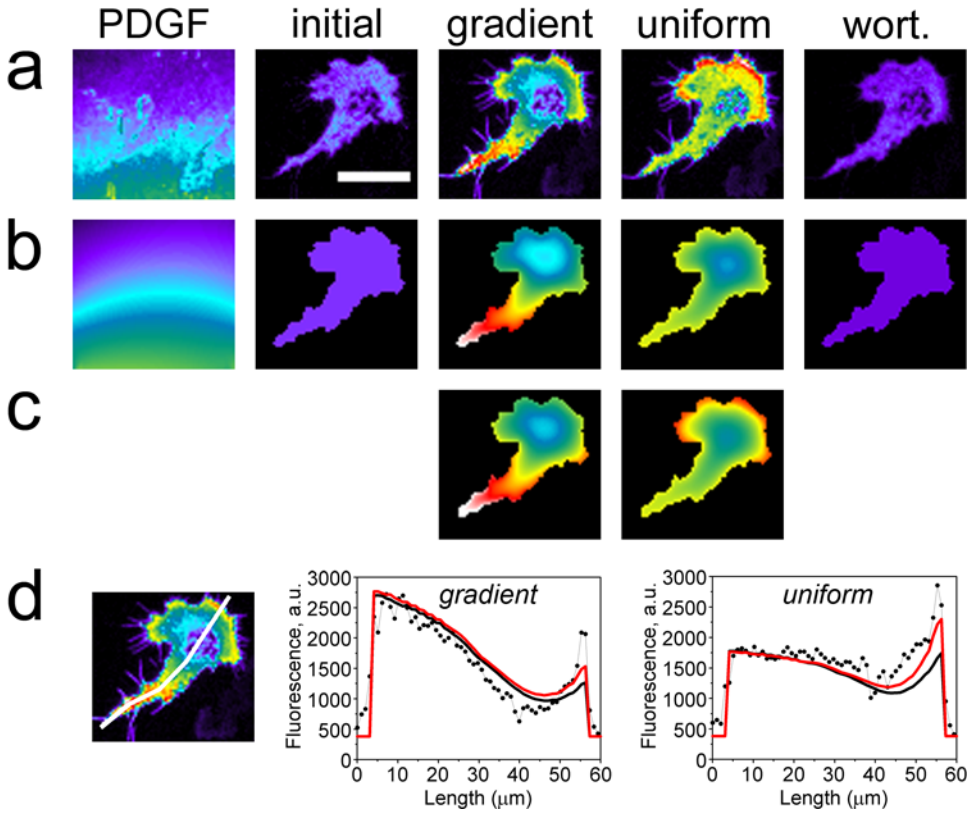

Figure 5.4 Spatial modeling of intracellular TIRF profiles. (*a*) TIRF images showing the extracellular OG 514-dextran profile (PDGF) and intracellular CFP-AktPH profiles as in Fig. 5.3 *a* (the cell is the same as in Fig. 5.3 *a*, with midpoint [PDGF] = 0.61 nM, $\delta = 0.75$). All CFP-AktPH images use the same absolute pseudo-color scale, and the OG 514 dextran image is scaled such that black is background and white is the TIRF intensity at the pipette tip. Scale bar = 30 μm. (*b*) Virtual images obtained from finite-element calculations (see Methods and Appendix E). Dimensionless parameter values describing 3' PI diffusion and the AktPH interaction are as used previously[37-39] [$Da = 3$, $\mu = 5$, $\kappa_P = 2$, $\upsilon_t = e + x_0(1 - \langle e \rangle)$, $\upsilon_b = x_0(1 - \langle e \rangle)$]; those describing the PDGF dose response are as used in Figs. 4.1 and 4.3 ($\alpha d_{max} = 10$, $\kappa_E = 0.1$ and $L^* = 1$ nM). The two remaining parameter values ($\sigma = 15.0$, $x_0 = 0.016$) were specified to match the overall fluorescence intensities observed prior to stimulation and after uniform PDGF stimulation. (*c*) Finite-element calculations accounting for enhanced 3' PI levels in leading-edge hot spots. Hot spots were modeled as regions with locally enhanced PI 3-kinase activity [$\upsilon_b = \upsilon_t = e + x_0(1 - \langle e \rangle)$] and slower 3' PI diffusion coefficient (reduced by half). Other parameters are as in *b*, except $\sigma = 16.3$, $x_0 = 0.015$. (*d*) Comparison of observed (symbols) and calculated (solid lines; the model with hot spots is in red) TIRF profiles along the line scan indicated (5 pixel width).

5.4.4 Kinetic analysis of responses to transient PDGF pulses

Another test of a mathematical model is its ability to reproduce the cellular response to a transient or pulsed stimulus, an approach that can indicate the presence of feedback interactions[40]. To see if our model could explain the 3' PI responses to transient PDGF stimulation, PDGF was pulsed from the micropipette for a certain period, and CFP-AktPH

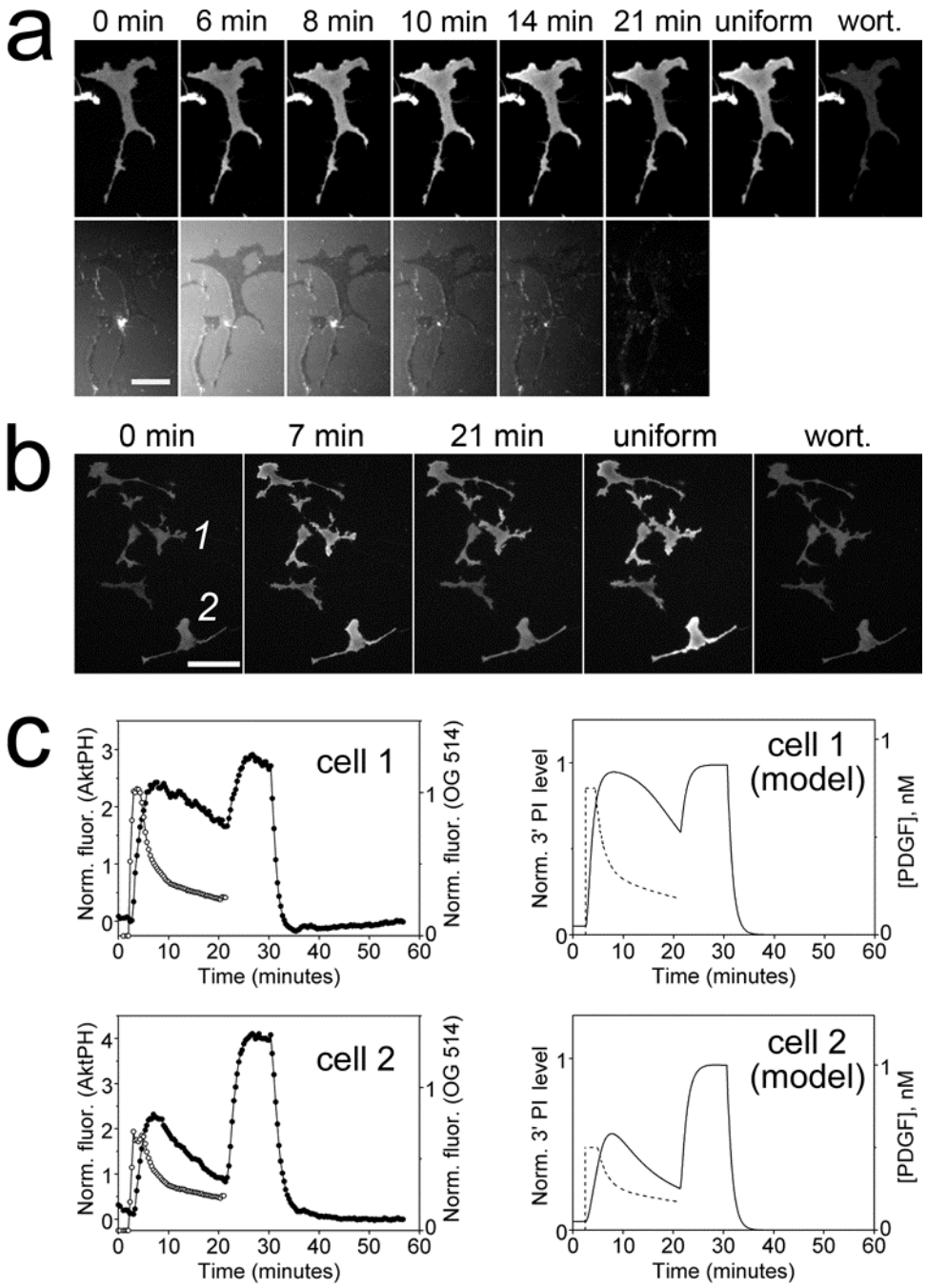

Figure 5.5 PI 3-kinase signaling kinetics in response to transient PDGF stimulation. (*a*) A CFP-AktPH-transfected fibroblast was stimulated with a moving PDGF gradient for 21 min, after which 10 nM PDGF (uniform) and subsequently wortmannin (wort.) were added as in Fig. 5.3. The time course montage shows TIRF images of the CFP-AktPH translocation (top row) and OG 514-dextran gradient (bottom row). Scale bar = 30 μm. (*b*) TIRF images of CFP-AktPH-transfected fibroblasts treated with a brief pulse of PDGF at 2 min, 10 nM PDGF (uniform) at 20 min and wortmannin (wort.) at 30 min. Scale bar = 60 μm. (*c*) The left panels plot average normalized TIRF intensity in the CFP-AktPH (●) and OG 514-dextran (○) channels as a function of time for the two cells indicated in *b*. The right panels are the corresponding kinetic model calculations (see Appendix E).

translocation during and after the pulse was recorded using TIRF microscopy (Fig. 5.5). By adjusting the flow rate, the steepness of the PDGF gradient during the pulse could be tuned to be high (Fig. 5.5 a) or shallow across cellular dimensions (Fig. 5.5 b and c). In both situations, PI 3-kinase signaling tends to persist for several minutes following the decay of the stimulus; in fact, the peak response was typically observed minutes after the PDGF concentration began to drop. Our kinetic model captures this behavior. It predicts that the 3' PI decay will lag whenever the duration of the pulse is insufficient for establishing a quasi-steady state (~ 10 min), with the time interval of the lag and rate of decay after the peak depending on the degree of PI 3-kinase saturation. Model and experiment are in quantitative agreement when one allows for the modest cell-to-cell variation in receptor and PI 3-kinase expression levels (Fig. 5.5 c).

5.4.5 Rho-family GTPases are not required for PDGF-stimulated PI 3-kinase activation

Our mathematical description of PDGF gradient sensing does not invoke feedback loops, and so we sought to rule out the need for Rho-family GTPases in amplifying PI 3-kinase activation in our system (Fig. 5.6). Such feedback is plausible given that PI 3-kinase regulatory subunits can interact directly with Rac-GTP[41,42]. In differentiated HL-60 cells, inactivation of Rho-family GTPases by *C. difficile* toxin B treatment ablated 3' PI accumulation in response to chemoattractants but not to insulin[8,22]. The latter signals through insulin and insulin-like growth factor receptors, which, like PDGF receptors, are receptor tyrosine kinases.

In fibroblasts, *C. difficile* toxin B treatment yielded the characteristic depolarized, rounded cell morphology and significantly smaller contact areas (Fig. 5.6 a) but did not compromise cell viability as judged by trypan blue exclusion (not shown). In response to PDGF stimulation, these cells responded with the normal, several-fold increase in TIRF excitation of fluorescent AktPH. To ensure that the fluorescence profile was not caused by differential adhesion across the contact area or other membrane artifacts in toxin-treated cells, experiments were performed using cells co-expressing YFP-AktPH and the membrane marker Lyn-CFP (Fig. 5.6 b). Although there were some regions with higher YFP-AktPH and Lyn-CFP TIRF intensities, ratio images confirmed specific, PDGF-induced 3' PI

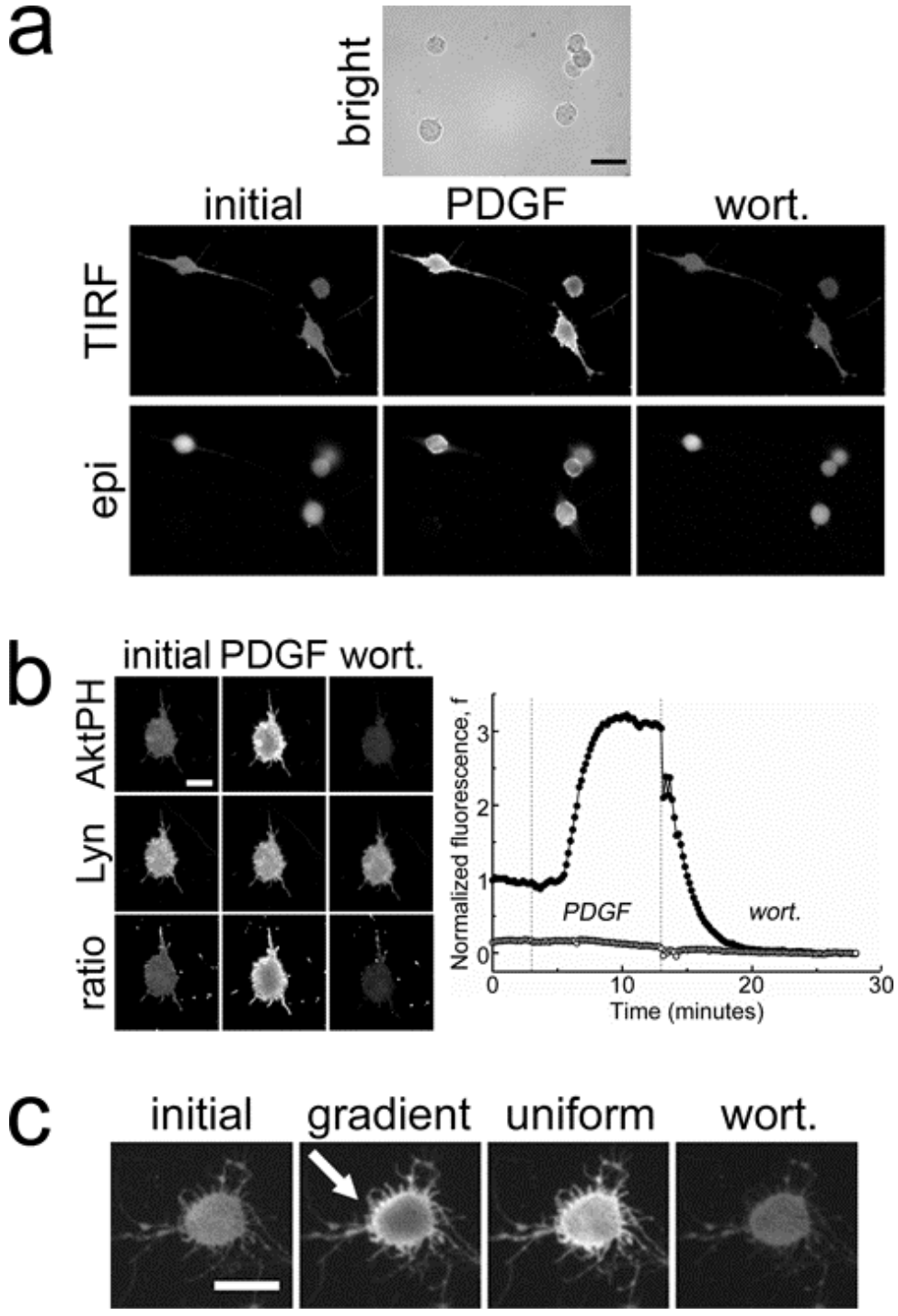

Figure 5.6 PDGF-stimulated PI 3-kinase activation is not dependent on Rho-family GTPases. (*a*) Bright field, TIRF, and epifluorescence images of GFP-AktPH-transfected fibroblasts, pre-treated with *C. difficile* toxin B, responding to successive additions of 10 nM PDGF and wortmannin (wort). Inactivation of Rho-family GTPases dramatically alters cell morphology but not PDGF-stimulated PI 3-kinase activation. Scale bar = 30 μm. (*b*) TIRF images of a fibroblast, co-transfected with YFP-AktPH and the membrane marker Lyn-CFP, treated as in *a*. Ratio images are YFP/CFP, and scale bar = 15 μm. The average normalized TIRF

intensity is plotted as a function of time for the YFP-AktPH (●) and Lyn-CFP (○) channels. (*c*) PDGF gradient sensing after inactivation of Rho-family GTPases. Toxin-treated cells typically showed AktPH translocation in TIRF but not a definite gradient sensing response, which was expected given the relatively small cell dimensions. The cell shown here is one of those in which a noticeable gradient response was seen. The arrow indicates the PDGF gradient orientation from high to low, and scale bar = 15 μm.

production with similar radial profile and kinetics as compared with cells not treated with the toxin.

When toxin-treated fibroblasts were exposed to PDGF gradients, CFP-AktPH translocation was readily observed, and asymmetric TIRF profiles consistent with proper gradient sensing were seen in some cells (Fig. 5.6 c). This outcome was not as robust as in our other gradient experiments, however, which was to be expected given the much smaller distance across the cells (~ 15 μm). This yields both smaller relative PDGF gradients and significant tempering of the intracellular 3' PI gradient through lateral diffusion of the lipid.

5.5 DISCUSSION

Using a combination of quantitative modeling and analysis, we have demonstrated that 3' PI-mediated PDGF gradient sensing in fibroblasts is sensitive to both the relative steepness and midpoint concentration of the gradient. Strong responses require relatively steep gradients ($\delta > 0.3$) and intermediate midpoint PDGF concentrations spanning a relatively narrow range (0.1–2 nM); these midpoint concentrations yield near maximal PI 3-kinase activation without saturating PDGF receptor binding. These characteristics and the lack of rapid adaptation in response to uniform PDGF stimulation suggest a different and simpler gradient sensing mechanism from those in fast-migrating, amoeboid cells such as *D. discoideum* and neutrophils. Accordingly, our model contains no feedback amplification or inhibition, with receptor signaling in different locations coupled only through exchange of PI 3-kinase molecules from a common, cytosolic pool, yet the model is quantitatively consistent with experimental observations.

Another wrinkle in the PDGF sensing mechanism is the influence of 3' PI hot spots, which we recently characterized in the context of uniform PDGF stimulation[38]. Regions of locally enhanced 3' PI levels have also been observed in chemoattractant-stimulated *D. discoideum*[9] and primary dendritic cells[43], although there are differences in the kinetics across cell types. In PDGF-stimulated fibroblasts, hot spots exhibit characteristics consistent with locally enhanced PI 3-kinase activation and reduced 3' PI turnover, and it is conceivable that feedback loops upstream of PI 3-kinase are spatially focused in these regions. Their localization in apparent membrane protrusion structures at the leading edge(s) suggests involvement of the cytoskeleton and/or Rho-family GTPases and an importance in cell motility. Thus, as illustrated in Fig. 5.4, the overall asymmetry in PI 3-kinase signaling depends on the morphological polarity of the cell relative to the gradient. A conceptual model emerges in which cells integrate both intrinsic and external spatial biases in order to migrate persistently towards PDGF gradients (Fig. 5.7).

The mechanism of PDGF gradient sensing is logical in light of the physiology of fibroblast invasion during wound healing, a process that evolves over several days. With PDGF and other factors produced specifically in the fibrin clot, and dermal fibroblasts found in the adjacent tissue, a PDGF concentration profile will naturally arise within hours. One

would expect the steepest PDGF gradient at the clot-dermis interface initially, and this gradient could be quite sharp if the relative PDGF diffusion and proteolysis rates in the tissue were favorable. The overall fibroblast response is slow, and the directedness of their migration does not need to change with time. Furthermore, PDGF receptor signaling is pleiotropic, influencing fibroblast proliferation and survival in addition to chemotaxis. Desensitization of PI 3-kinase signaling would compromise these other functions, which generally depend on the absolute concentration of stimulus.

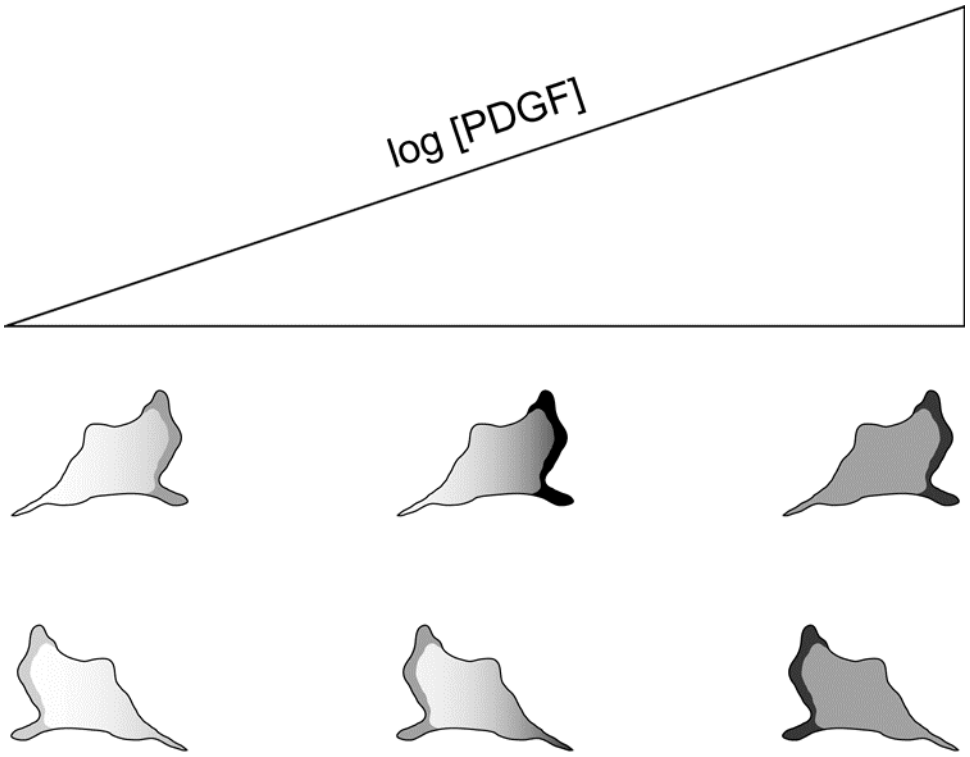

Figure 5.7 Integration of external and intrinsic biases in PDGF gradient sensing. Cells are depicted at three positions in a PDGF gradient, corresponding to low, intermediate, and high midpoint concentrations. Optimal sensing of the external gradient is seen in a narrow range of intermediate concentrations, sufficient for maximal PI 3-kinase activation at the plasma membrane. Higher concentrations that saturate receptor occupancy have a leveling effect on PI 3-kinase recruitment across the cell. Hot spots of PI 3-kinase signaling are located at the leading edge and other regions of membrane protrusion, imposing an intrinsic, localized bias that depends on the cell's direction of movement relative to the gradient. This suggests a mechanism by which fibroblasts migrate with even greater speed and/or persistence towards the PDGF source.

This is not to say that PDGF receptor-mediated signaling, through PI 3-kinase and other pathways, is unregulated. Activated PDGF receptors are rapidly internalized, mediating receptor downregulation and establishment of a true steady state after ~ 1 h of

constant stimulation. This mode of regulation may provide the answer to the next, most important question with regard to fibroblast invasion of wounds: if chemotaxis is sensitive to the gradient steepness and absolute concentration of PDGF, how can this sensitivity be maintained as the fibroblast front (granulation tissue) progresses deeper into the clot? In solid tissue, it is likely that endocytosis of active PDGF/PDGF receptor complexes contributes significantly to the clearance of PDGF from the extracellular milieu, an effect that would be fibroblast density-dependent. The invading granulation tissue could thus produce a relatively constant and sharp PDGF gradient at its front, which could be maintained at the proper midpoint concentration.

Given the complexity of cell polarity, cytoskeletal dynamics, and overall migration processes, as well as the issues raised above concerning the integrated physiological system, it is reasonable to expect that mathematical modeling and other quantitative approaches will be increasingly valuable in their analysis. Especially when designed in tandem with experiments, as applied here to PDGF gradient sensing, such approaches can reveal and aid in characterizing the key underlying mechanisms.

5.6 REFERENCES

1. Devreotes, P.N. & Zigmond, S.H. Chemotaxis in eukaryotic cells: a focus on leukocytes and Dictyostelium. Annu. Rev. Cell Biol. 4, 649-686 (1988).
2. Merlot, S. & Firtel, R.A. Leading the way: directional sensing through phosphatidylinositol 3-kinase and other signaling pathways. J. Cell Sci. 116, 3471-3478 (2003).
3. Ridley, A.J. Rho GTPases and cell migration. J. Cell Sci. 114, 2713-2722 (2001).
4. Wang, F. et al. Lipid products of PI(3)Ks maintain persistent cell polarity and directed motility in neutrophils. Nat. Cell Biol. 4, 513-518 (2002).
5. Srinivasan, S. et al. Rac and Cdc42 play distinct roles in regulating PI(3,4,5)P3 and polarity during neutrophil chemotaxis. J. Cell Biol. 160, 375-385 (2003).
6. Stephens, L.R., Hughes, K.T. & Irvine, R.F. Pathway of phosphatidylinositol(3,4,5)-trisphosphate synthesis in activated neutrophils. Nature 351, 33-39 (1991).
7. Zigmond, S.H. & Sullivan, S.J. Sensory adaptation of leukocytes to chemotactic peptides. J. Cell Biol. 82, 517-527 (1979).
8. Servant, G. et al. Polarization of chemoattractant receptor signaling during neutrophil chemotaxis. Science 287, 1037-1040 (2000).
9. Postma, M. et al. Sensitization of Dictyostelium chemotaxis by phosphoinositide-3-kinase-mediated self-organizing signalling patches. J. Cell Sci. 117, 2925-2035 (2004).
10. Zigmond, S.H. Ability of polymorphonuclear leukocytes to orient in gradients of chemotactic factors. J. Cell Biol. 75, 606-616 (1977).
11. Parent, C.A., Blacklock, B.J., Froehlich, W.M., Murphy, D.B. & Devreotes, P.N. G protein signaling events are activated at the leading edge of chemotactic cells. Cell 95, 81-91 (1998).
12. Janetopoulos, C., Ma, L., Devreotes, P.N. & Iglesias, P.A. Chemoattractant-induced phosphatidylinositol 3,4,5-trisphosphate accumulation is spatially amplified and adapts, independent of the actin cytoskeleton. Proc. Natl. Acad. Sci. U.S.A. 101, 8951-8956 (2004).
13. Parent, C.A. & Devreotes, P.N. A cell's sense of direction. Science 284, 765-770 (1999).
14. Devreotes, P. & Janetopoulos, C. Eukaryotic chemotaxis: distinctions between directional sensing and polarization. J. Biol. Chem. 278, 20445-20448 (2003).
15. Weiner, O.D. Regulation of cell polarity during eukaryotic chemotaxis: the chemotactic compass. Curr. Opin. Cell Biol. 14, 196-202 (2002).
16. Meinhardt, H. Orientation of chemotactic cells and growth cones: models and mechanisms. J. Cell Sci. 112, 2867-2874 (1999).
17. Narang, A., Subramanian, K.K. & Lauffenburger, D.A. A mathematical model for chemoattractant gradient sensing based on receptor-regulated membrane phospholipid signaling dynamics. Ann. Biomed. Eng. 29, 677-691 (2001).
18. Postma, M. & Van Haastert, P.J.M. A diffusion-translocation model for gradient sensing by chemotactic cells. Biophys. J. 81, 1314-1323 (2001).
19. Levchenko, A. & Iglesias, P.A. Models of eukaryotic gradient sensing: application to chemotaxis of amoebae and neutrophils. Biophys. J. 82, 50-63 (2002).
20. Subramanian, K.K. & Narang, A. A mechanistic model for eukaryotic gradient sensing: spontaneous and induced phosphoinositide polarization. J. Theor. Biol., 49-67 (2004).
21. Ma, L., Janetopoulos, C., Yang, L., Devreotes, P.N. & Iglesias, P.A. Two complementary, local excitation, global inhibition mechanisms acting in parallel can explain the chemoattractant-induced regulation of PI(3,4,5)P3 response in Dictyostelium cells. Biophys. J. 87, 3764-3774 (2004).
22. Weiner, O.D. et al. A PtdInsP3- and Rho GTPase-mediated positive feedback loop regulates neutrophil polarity. Nat. Cell Biol. 4, 509-512 (2002).
23. Singer, A.J. & Clark, R.A.F. Mechanisms of disease: cutaneous wound healing. N. Engl. J. Med. 341, 738-746 (1999).
24. Deuel, T.F., Kawahara, R.S., Mustoe, T.A. & Pierce, G.F. Growth factors and wound healing: platelet-derived growth factor as a model cytokine. Annu. Rev. Med. 42, 567-584 (1991).
25. Heldin, C.-H. & Westermark, B. Mechanism of action and in vivo role of platelet-derived growth factor. Physiol. Rev. 79, 1283-1316 (1999).

26. Kundra, V. et al. Regulation of chemotaxis by the platelet-derived growth factor receptor-b. Nature 367, 474-476 (1994).
27. Wennström, S. et al. Activation of phosphoinositide 3-kinase is required for PDGF-stimulated membrane ruffling. Curr. Biol. 4, 385-393 (1994).
28. Wennström, S. et al. Membrane ruffling and chemotaxis transduced by the PDGF b-receptor require the binding site for phosphatidylinositol 3' kinase. Oncogene 9, 651-660 (1994).
29. Wymann, M. & Arcaro, A. Platelet-derived growth factor-induced phosphatidylinositol 3-kinase activation mediates actin rearrangements in fibroblasts. Biochem. J. 298, 517-520 (1994).
30. Haugh, J.M., Codazzi, F., Teruel, M. & Meyer, T. Spatial sensing in fibroblasts mediated by 3' phosphoinositides. J. Cell Biol. 151, 1269-1279 (2000).
31. Lauffenburger, D.A. & Horwitz, A.F. Cell migration: a physically integrated molecular process. Cell 84, 359-369 (1996).
32. Vanhaesebroeck, B. et al. Synthesis and function of 3-phosphorylated inositol lipids. Annu. Rev. Biochem. 70, 535-602 (2001).
33. Hawkins, P.T., Jackson, T.R. & Stephens, L.R. Platelet-derived growth factor stimulates synthesis of PtdIns(3,4,5)P3 by activating a PtdIns(4,5)P2 3-OH kinase. Nature 358, 157-159 (1992).
34. Jackson, T.R., Stephens, L.R. & Hawkins, P.T. Receptor specificity of growth factor-stimulated synthesis of 3-phosphorylated inositol lipids in Swiss 3T3 cells. J. Biol. Chem. 267, 16627-16636 (1992).
35. Park, C.S., Schneider, I.C. & Haugh, J.M. Kinetic analysis of platelet-derived growth factor receptor/phosphoinositide 3-kinase/Akt signaling in fibroblasts. J. Biol. Chem. 278, 37064-37072 (2003).
36. Kazlauskas, A. & Cooper, J.A. Phosphorylation of the PDGF receptor b-subunit creates a tight binding site for phosphatidylinositol-3 kinase. EMBO J. 9, 3279-3286 (1990).
37. Schneider, I.C. & Haugh, J.M. Spatial analysis of 3' phosphoinositide signaling in living fibroblasts: II. Parameter estimates for individual cells from experiments. Biophys. J. 86, 599-608 (2004).
38. Schneider, I.C., Parrish, E.M. & Haugh, J.M. Spatial analysis of 3' phosphoinositide signaling in living fibroblasts, III: Influence of cell morphology and morphological polarity. Biophys. J., 1420-1430 (2005).
39. Haugh, J.M. & Schneider, I.C. Spatial analysis of 3' phosphoinositide signaling in living fibroblasts: I. Uniform stimulation model and bounds on dimensionless groups. Biophys. J. 86, 589-598 (2004).
40. Bhalla, U.S., Ram, P.T. & Iyengar, R. MAP kinase phosphatase as a locus of flexibility in a mitogen-activated protein kinase signaling network. Science 297, 1018-1023 (2002).
41. Tolias, K.F., Cantley, L.C. & Carpenter, C.L. Rho family GTPases bind to phosphoinositide kinases. J. Biol. Chem. 270, 17656-17659 (1995).
42. Bokoch, G.M., Vlahos, C.J., Wang, Y., Knaus, U.G. & Traynor-Kaplan, A.E. Rac GTPase interacts specifically with phosphatidylinositol 3-kinase. Biochem. J. 315, 775-779 (1996).
43. Arrieumerlou, C. & Meyer, M. A local coupling model and compass parameter for eukaryotic chemotaxis. Dev. Cell 8, 215-227 (2005).
44. Teruel, M.N., Blanpied, T.A., Shen, K., Augustine, G.J. & Meyer, T. A versatile microporation technique for the transfection of cultured CNS neurons. J. Neurosci. Methods 93, 37-48 (1999).
45. Axelrod, D. Total internal reflection fluorescence microscopy in cell biology. Traffic 2, 764-774 (2001).
46. Steyer, J.A. & Almers, W. A real-time view of life within 100 nm of the plasma membrane. Nat. Rev. Mol. Cell Biol. 2, 268-275 (2001).
47. Toomre, D. & Manstein, D.J. Lighting up the cell surface with evanescent wave microscopy. Trends Cell Biol. 11, 298-303 (2001).
48. Lanni, F., Waggoner, A.S. & Taylor, D.L. Structural organization of interphase 3T3 fibroblasts studied by total internal reflection fluorescence microscopy. J. Cell Biol. 100, 1091-1102 (1985).

APPENDIX A: Uniform stimulation model solution and calculations for a hemisphere

Solution of the partial differential equations for a hemisphere

From Equations 2.1-2.3, the 3' PI densities in the two domains are found using the Finite Fourier Transform method (Deen 1998):

$$\begin{aligned} &x_b(\rho,\tau) = e^{-\tau}\int_0^\tau \upsilon_b e^{\tau} d\tau \\ &\quad + 2\sum_{n=0}^{\infty} \Phi_n e^{-b_n\tau}\left[\int_0^1 x_b(\rho,0)\Phi_n \rho d\rho + \int_0^\tau g e^{b_n\tau} d\tau\right] \\ &\Phi_n(\rho) \equiv J_0(\lambda_n\rho)/J_0(\lambda_n); \quad J_1(\lambda_n) = 0; \\ &b_n \equiv 1 + \lambda_n{}^2/Da \end{aligned} \qquad \text{(A1);}$$

$$\begin{aligned} &x_t(\eta,\tau) = \alpha e^{-\alpha\tau}\int_0^\tau \upsilon_t e^{\alpha\tau} d\tau \\ &\quad + \sum_{n=0}^{\infty} \Psi_n e^{-a_n\tau}\left[\int_0^1 x_t(\eta,0)\Psi_n d\eta - \Psi_n(0)\int_0^\tau g e^{a_n\tau} d\tau\right] \\ &\Psi_n(\eta) \equiv (4n+1)^{1/2} P_{2n}(\eta); \\ &a_n \equiv \alpha + 2n(2n+1)\gamma/Da \end{aligned} \qquad \text{(A2),}$$

where J_m and P_m are Bessel functions and Legendre polynomials of order m, respectively, and the boundary gradient function g is defined as

$$g(\tau) = \frac{1}{Da}\frac{\partial x_b(1,\tau)}{\partial\rho} = \frac{\gamma}{Da}\frac{\partial x_t(0,\tau)}{\partial\eta} \qquad \text{(A3).}$$

Calculated average and steady state 3' PI concentrations

The average 3' PI concentration in each domain is found using surface integrals. Only the leading terms in the infinite series contribute:

$$\begin{aligned}\overline{x}_b(\tau) &\equiv 2\int_0^1 x_b(\rho,\tau)\rho d\rho \\ &= e^{-\tau}\left[\overline{x}_b(0) + \int_0^\tau \upsilon_b e^\tau d\tau + 2\int_0^\tau g e^\tau d\tau\right]\end{aligned} \tag{A4};$$

$$\begin{aligned}\overline{x}_t(\tau) &\equiv \int_0^1 x_t(\eta,t)d\eta \\ &= e^{-\alpha\tau}\left[\overline{x}_t(0) + \alpha\int_0^\tau \upsilon_t e^{\alpha\tau} d\tau - \int_0^\tau g e^{\alpha\tau} d\tau\right]\end{aligned} \tag{A5}.$$

These quantities are used to calculate the total number of 3' PI molecules in the cell, which is proportional to

$$x_{Tot}(\tau) \equiv 2\overline{x}_t(\tau) + \overline{x}_b(\tau) \tag{A6}.$$

Provided that a nonzero steady state is achieved, one may define X^* such that $\upsilon_{t,ss} = 1$, and the boundary gradient g_{ss} and the dimensionless steady state 3' PI distribution in the bottom domain are readily derived:

$$\begin{aligned}g_{ss} &= (1-\nu)\left[Da^{1/2}\frac{I_0(Da^{1/2})}{I_1(Da^{1/2})} + \sum_{n=0}^{\infty}\frac{\Psi_n^2(0)}{a_n}\right]^{-1} \\ x_{b,ss}(\rho) &= \nu + g_{ss}\frac{Da^{1/2}I_0(Da^{1/2}\rho)}{I_1(Da^{1/2})};\quad \nu \equiv \frac{V_{b,ss}}{V_{t,ss}}\frac{k_t}{k_b}\end{aligned} \tag{A7},$$

where I_m are modified Bessel functions of order m. At steady state, the quantity x_{Tot} from Equation A6 reduces to

$$x_{Tot,ss} = 2 + \nu - 2(\alpha^{-1} - 1)g_{ss} \tag{A8}.$$

As described in Chapter 2, convenient steady state metrics are the quantities $f_{SS}(0)/f_{avg,SS}$ and $f_{avg,SS}/p_{SS}$, given by

$$\frac{f_{ss}(0)}{f_{avg,SS}} = \frac{\sigma\left[\nu + Da^{1/2} g_{ss} \big/ I_1(Da^{1/2})\right] - x_{Tot,ss}}{\sigma(\nu + 2g_{ss}) - x_{Tot,ss}} \qquad \text{(A9);}$$

$$f_{avg,SS} \big/ p_{ss} = \sigma(\nu + 2g_{ss}) \big/ x_{Tot,ss} - 1 \qquad \text{(A10).}$$

Computation of 3' PI density profiles

The quantities $x_b(\rho,\tau)$, $x_t(\eta,\tau)$, $\bar{x}_b(\tau)$, and $\bar{x}_t(\tau)$ were computed using subroutines composed in FORTRAN 90. Briefly, each spatial domain is split into 50 equal segments in ρ or η, and the initial conditions $x_b(\tilde{\rho})$ and $x_t(\tilde{\eta})$ are read from data files. Before stimulation, the initial conditions $x_b(\rho,0) = x_t(\eta,0) = x_0$ (constant) were generally assumed; for PI 3-kinase inhibition, the steady state distributions immediately before inhibitor addition are used to reinitialize the simulation. The infinite series in Equations A1 & A2 are truncated at 2000 terms, and the integrals containing $x_b(\rho,0)$ and $x_t(\eta,0)$ are evaluated numerically. Dimensionless time τ is stepped 1000 times for each of the intervals 10^{-5}, 10^{-4}, 10^{-3}, and 10^{-2}, for a total time τ of 11.11. At each time step, the boundary gradient function $g(\tau)$ and the associated integrals are estimated as described below. It was confirmed that decreasing the time steps by a factor of 10, or increasing the number of terms in the infinite series by two-fold, did not significantly affect the program output at a resolution of 0.01 in τ.

The function $g(\tau)$ is found by matching $x_b(1,\tau)$ and $x_t(0,\tau)$ at the perimeter. Its evaluation is aided by the approximation that it is linear over a sufficiently small interval, i.e.,

$$\int_{y_1}^{y_2} g(y)e^{y}dy \approx e^{y_2}g(y_2) - e^{y_1}g(y_1) - \frac{e^{y_2}-e^{y_1}}{y_2-y_1}\left[g(y_2)-g(y_1)\right] \qquad \text{(A11)}.$$

Our new method for estimating $g(\tau)$ involves a linear interpolation, incorporating Equations A1, A2, & A11:

$$g(\tau) \approx \frac{1}{2}\left[g(\tau-\Delta\tau)+g(\tau+\Delta\tau)\right]$$

$$\approx \frac{h(\tau)-\sum_{n=0}^{\infty}\left[\frac{\Phi_n^2(0)}{a_n}\Omega_{a_n}(\tau,2\Delta\tau)+\frac{2}{b_n}\Omega_{b_n}(\tau,2\Delta\tau)\right]}{\sum_{n=0}^{\infty}\left[\frac{\Phi_n^2(0)}{a_n}\left(1-\frac{1-e^{-2a_n\Delta\tau}}{2a_n\Delta\tau}\right)+\frac{2}{b_n}\left(1-\frac{1-e^{-2b_n\Delta\tau}}{2b_n\Delta\tau}\right)\right]}$$

$$h(\tau) \equiv \alpha e^{-\alpha\tau}\int_0^{\tau}\upsilon_t e^{\alpha\tau}d\tau - e^{-\tau}\int_0^{\tau}\upsilon_b e^{\tau}d\tau + \sum_{n=0}^{\infty}\left[\Psi_n(0)e^{-a_n\tau}\int_0^1 x_{t,0}\Psi_n d\eta - 2e^{-b_n\tau}\int_0^1 x_{b,0}\Phi_n\rho d\rho\right] \qquad \text{(A12)},$$

subject to the recursion formula

$$\Omega_c(y,\Delta y) = e^{-c\Delta y}\Omega_c(y-\Delta y,\Delta y)+\frac{(1-e^{-c\Delta y})^2}{c\Delta y}g(y-\Delta y)$$
$$\Omega_c(0,\Delta y) = 0 \qquad \text{(A13)}.$$

APPENDIX B: From lipid density profiles to fluorescence profiles

The fluorescence intensity, F, is normalized to give the scaled quantity, f, where F_{cyt} is the intensity observed when all of the fluorescent probe is in the cytosol:

$$f(\rho,\tau) \equiv \frac{F(\rho,\tau) - F_{cyt}}{F_{cyt}} \qquad \text{(B1).}$$

The fluorescence F is the sum of two contributions, from probe molecules in the cytosol and from those bound to the membrane contact area. We assume that the probe diffuses rapidly within the cytosol. Taking C to be the free concentration of the probe everywhere in the cytosol, and noting that the energy of an evanescent wave decays exponentially with distance, the cytosolic contribution is given by

$$F_1 = aC(\tau)\int_0^\infty e^{-z/d_{cell}}\,dz = ad_{cell}C(\tau) \qquad \text{(B2),}$$

where a is the fluorescence per unit GFP-AktPH and d_{cell} is the space constant for the penetration of the evanescent wave (~ 100 nm). Let $p(\tau)$ be the fraction of the probe that is bound to 3' PIs in both the bottom and top membrane domains; assuming pseudo-equilibrium between bound and unbound probe, and accounting for the fact that probe binding depletes both the cytosolic probe and the number of free 3' PI molecules, p is given by

$$\begin{aligned} p(\tau) &= 1 - V_{cyt}C(\tau)/P_{Tot} \\ &= \frac{C(\tau)}{K_D}\left[\frac{A_c X^* x_{Tot}(\tau)}{P_{Tot}} - p(\tau)\right] \end{aligned} \qquad \text{(B3),}$$

where P_{Tot} is the total number of probe molecules in the cell, V_{cyt} is volume of the cytosol, K_D is the dissociation constant of the probe-3' PI interaction, and A_c is the surface area of the membrane contact region. With x_{Tot} defined as in Equation A6, the quantity $A_c X^* x_{Tot}$ is the total number of 3' PI molecules in the cell. Pseudo-equilibrium also holds at every point in

the contact area; defining $PX(\rho,\tau)$ as the density of probe-3' PI complexes at a given location,

$$PX(\rho,\tau) = \frac{C(\tau)}{K_D}\left[X^* x_b(\rho,\tau) - PX(\rho,\tau)\right] \quad \text{(B4).}$$

Combining Equations B3 & B4,

$$PX(\rho,\tau) = \frac{x_b(\rho,\tau)}{x_{Tot}(\tau)}\frac{P_{Tot}}{A_c}p(\tau) \quad \text{(B5).}$$

Now suppose that the bound probe is confined to a small distance δ adjacent to the plasma membrane (< 10 nm). The effective concentration of the bound probe at a particular contact area position is thus PX/δ, and assuming $\delta/d_{cell} << 1$, its fluorescence contribution is

$$F_2 = a(PX/\delta)\int_0^{\delta} e^{-z/d_{cell}}dz \approx aPX(\rho,\tau) \quad \text{(B6).}$$

The total fluorescence, F, is found by summing F_1 and F_2 from Equations B2 & B6. Finally, noting that

$$F_{cyt} = a\frac{P_{Tot}}{V_{cyt}}d_{cell} \quad \text{(B7),}$$

and incorporating Equations B1, B3, & B5, we obtain the normalized fluorescence, $f(\rho,\tau)$:

$$f(\rho,\tau) = \left[\frac{\sigma x_b(\rho,\tau)}{x_{Tot}(\tau)} - 1\right]p(\tau); \quad \sigma \equiv \frac{V_{cyt}}{A_c d_{cell}} \quad \text{(B9).}$$

From the relations given in Equation B3, $C(\tau)$ can be eliminated and $p(\tau)$ expressed in terms of $x_{Tot}(\tau)$ and constants:

$$p(\tau) = \frac{1 + \kappa + \mu x_{Tot} - \left[(1 + \kappa + \mu x_{Tot})^2 - 4\mu x_{Tot}\right]^{1/2}}{2} \qquad \text{(B10).}$$

$$\kappa \equiv K_D V_{cyt} / P_{Tot} \; ; \quad \mu \equiv A_c X^* / P_{Tot}$$

APPENDIX C: Independent determination of σ

The parameter σ is defined as the volume of the cytosol over the effective excitation volume of the evanescent wave:

$$\sigma \equiv V_{cyt} \Big/ A_c d_{cell} \qquad \text{(C1)},$$

where V_{cyt} is the volume of the cytosol, A_c is the surface area of the membrane contact zone, and d_{cell} is the effective penetration depth of the evanescent wave into the cell (~ 100 nm). Our approach is to sequentially image the same cell using epifluorescence (entire volume) and TIRF excitation of EYFP and ECFP probes. To acquire epifluorescence, our Zeiss stand was also equipped with a HBO 50 lamp and optics train, and excitation dichroics for ECFP and EYFP were from Chroma. The experiments described here were all performed on the same day.

The first experiment is used to calibrate the power densities of the excitation sources. Cells are co-transfected with soluble YFP and CFP. The average fluorescence intensities for epifluorescence and TIRF excitation in the YFP channel are given by:

$$\begin{aligned} \overline{F}_{Epi,Y} A_{epi} &= q_{Epi,Y} V_{cyt} C_Y \\ \overline{F}_{TIRF,Y} &= q_{TIRF,Y} \beta_Y d_{cell,Y} C_Y \\ \beta_Y &= \exp\left(-h_{gap} \Big/ d_{buff,Y}\right) \end{aligned} \qquad \text{(C2)}.$$

The constants $q_{Epi,Y}$ and $q_{TIRF,Y}$ are the fluorescence emission detected in the YFP channel per mole YFP in the excitation region for epifluorescence and TIRF excitation modes, respectively. They account for the power density of excitation, absorbance and quantum yield by the fluorophore, and quantum efficiency of the light collection and detection setup. C_Y is the concentration of YFP in the cytosol, A_{epi} is the area of the region of interest in epifluorescence mode, $d_{buff,Y}$ is the space constant of evanescent wave decay in the extracellular buffer, and h_{gap} is the average height of the gap between the glass surface and the inner face of the plasma membrane. With corresponding measurements in the CFP

channel, and noting that d_{cell} is proportional to excitation wavelength, we obtain the cytosolic ratio $\rho_{c/c}$:

$$\rho_{c/c} \equiv \frac{\overline{F}_{TIRF,C}}{\overline{F}_{TIRF,Y}} \frac{\overline{F}_{Epi,Y}}{\overline{F}_{Epi,C}} = \frac{q_{TIRF,C}}{q_{TIRF,Y}} \frac{q_{Epi,Y}}{q_{Epi,C}} \frac{\beta_C}{\beta_Y} \frac{\lambda_{ex,C}}{\lambda_{ex,Y}} \qquad \text{(C3)},$$

where $\lambda_{ex,C}/\lambda_{ex,Y}$ is the ratio of the excitation wavelengths used to excite CFP and YFP in TIRF mode. Technically, the ratio β_C/β_Y varies among cells with different h_{gap}, but the variation is expected to be small. For example, we estimate that a difference in h_{gap} of 50 nm yields a difference in β_C/β_Y of only 8%. Applying this methodology to different cells imaged in multiple fields, we observed a $\rho_{c/c}$ value of $4.259 \pm 0.925 \times 10^{-3}$ (mean ± s.d., $n = 14$).

In the second experiment, cells are co-transfected with soluble YFP and a plasma membrane-targeted CFP construct containing the myristoylation sequence of Lyn. Assuming that the confinement distance of lyn-CFP at the plasma membrane (< 10 nm) is much less than $d_{cell,C}$ (~ 100 nm), the average fluorescence intensities for epifluorescence and TIRF excitation in the CFP channel (for a hemisphere geometry) would be

$$\begin{aligned} \overline{F}_{Epi,lynC} A_{epi} &= q_{Epi,C} N_{lynC} \\ \overline{F}_{TIRF,lynC} &= q_{TIRF,C} \beta_C N_{lynC} / 3A_c \end{aligned} \qquad \text{(C4)},$$

where N_{lynC} is the moles of lyn-CFP expressed in the cell. Thus, we may define the membrane/cytosol ratio, $\rho_{m/c}$, as

$$\rho_{m/c} \equiv \frac{\overline{F}_{TIRF,lynC}}{\overline{F}_{TIRF,Y}} \frac{\overline{F}_{Epi,Y}}{\overline{F}_{Epi,lynC}} = \frac{q_{TIRF,C}}{q_{TIRF,Y}} \frac{q_{Epi,Y}}{q_{Epi,C}} \frac{\beta_C}{\beta_Y} \frac{V_{cyt}}{3d_{cell,Y} A_c} \qquad \text{(C5)}.$$

Measurements in multiple fields yielded $\rho_{m/c} = 26.51 \pm 6.02 \times 10^{-3}$ (mean ± s.d., $n = 16$).

Combining the results of these two experiments gives the value of σ. For example, to obtain the value for GFP excitation, σ_G,

$$\sigma_G = 3\frac{\lambda_{ex,C}}{\lambda_{ex,G}}\frac{\rho_{m/c}}{\rho_{c/c}} \qquad \text{(C6)}.$$

With $\lambda_{ex,C}$ = 457 nm and $\lambda_{ex,G}$ = 488 nm, and applying standard propagation of error, one obtains a σ_G value of 17.5 ± 5.5.

APPENDIX D: Uniform stimulation model solution and calculations for a two-sided arbitrary geometry.

Partial differential equations and boundary conditions

Let x_t and x_b be the 3' PI density profiles in the top (nonadherent) and bottom (contact area) domains of the plasma membrane. PI 3-kinase activation is characterized by different time-dependent source terms in the top and bottom domains (υ_t and υ_b, respectively); here we explicitly assume that the 3' PI diffusion coefficient and turnover rate constant, D and k respectively, are the same in both domains. In mathematical terms, the conservation equations to be solved are

$$\begin{aligned} &\frac{\partial x_t}{\partial \tau} = Da^{-1}\nabla^2 x_t - x_t + \upsilon_t(\tau); \\ &\frac{\partial x_b}{\partial \tau} = Da^{-1}\nabla^2 x_b - x_b + \upsilon_b(\tau); \\ &\tau = kt; \quad Da = kL^2/D. \end{aligned} \tag{D1}$$

The characteristic length scale, L, relates the size of the model domain to actual lengths. It is assumed here that the cell is flat, i.e., the top and bottom domains are mirror images of one another, with exchange at the periphery; for now we make no other restriction on the shape of the cell. Denoting S as the shared periphery of both domains, the matching boundary conditions must be satisfied on S:

$$x_t\big|_S = x_b\big|_S = x\big|_S; \tag{D2}$$

$$n \cdot \nabla x_t\big|_S = -n \cdot \nabla x_b\big|_S, \tag{D3}$$

where n is the unit vector normal to the boundary. Eq. D3 may be expressed as

$$n \cdot \nabla\left(x_t + x_b\right)\big|_S = 0. \tag{D4}$$

The form of Eq. D1, along with Eq. D4, yields a major simplification: if the initial lipid profiles also satisfy Eq. D2, the sum of $x_t + x_b$ at any corresponding position in the two boundaries, defined as x_{Tot}, is a function of time only:

$$\begin{aligned} &x_t + x_b = x_{Tot}(\tau) = e^{-\tau}\left[x_{Tot}(0) + \int_0^\tau \upsilon e^{\tau'} d\tau'\right]; \\ &\upsilon(\tau) = \upsilon_t + \upsilon_b. \end{aligned} \tag{D5}$$

Incorporating Eq. D2, we obtain a closed-form boundary condition, which can be used to solve Eq. D1 for the bottom domain:

$$x\big|_S = x_{Tot}(\tau)/2\,. \tag{D6}$$

Therefore, when the underlying assumptions are valid, the 3' PI density is the same at all points around the periphery.

Solution of partial differential equations for a two-sided disk

We turn now to a circular bottom domain of radius R ($L = R$), with a specified concentration at the periphery. The general solution is given in terms of $z = x_b - x\big|_S$, as a function of radial position $\rho = r/R$ and dimensionless time:

$$\begin{aligned}
&z(\rho,\tau) = 2\sum_{n=1}^{\infty}\Theta_n e^{-\beta_n\tau}\left[\Phi_{n,0} - \frac{\int_0^{\tau}(\upsilon_t-\upsilon_b)e^{\beta_n\tau'}d\tau'}{2\zeta_n}\right];\\
&\Theta_n(\rho) = J_0(\zeta_n\rho)/J_1(\zeta_n);\quad J_0(\zeta_n) = 0;\\
&\Phi_{n,0} = \int_0^1 z(\rho,0)\Theta_n\rho d\rho;\\
&\beta_n = 1+\zeta_n{}^2/Da\,,
\end{aligned} \tag{D7}$$

where J_m are Bessel functions of order m. For the association phase of an experiment, in which PI 3-kinase is rapidly activated by maximal receptor stimulation ($\upsilon_t = 1$; $\upsilon_b = \nu$) and the 3' PI profile is assumed to be flat initially ($x_b(\rho,0) = x_0$, $z(\rho,0) = 0$),

$$\begin{aligned}
&x\big|_S(\tau) = x_0e^{-\tau} + \left(\frac{1+\nu}{2}\right)\left(1-e^{-\tau}\right);\\
&z(\rho,\tau) = -(1-\nu)\sum_{n=1}^{\infty}\frac{\Theta_n}{\zeta_n\beta_n}\left(1-e^{-\beta_n\tau}\right).
\end{aligned} \tag{D8}$$

At steady state, the lipid profile simplifies to

$$x_{b,ss}(\rho) = \nu + \frac{(1-\nu)}{2}\frac{I_0\left(Da^{1/2}\rho\right)}{I_0\left(Da^{1/2}\right)}. \tag{D9}$$

For the dissociation phase of the experiment, in which PI 3-kinase activity is instantaneously blocked ($\upsilon_t = \upsilon_b = 0$), it is noted that Eq. D9 serves as the initial condition, with $x_{b,ss}(\rho) + x_{t,ss}(\rho) = 1 + \nu$ at all ρ. Hence,

$$x\big|_S = \left(\frac{1+\nu}{2}\right)e^{-\tau};$$
$$z(\rho,\tau) = -(1-\nu)\sum_{n=1}^{\infty}\frac{\Theta_n e^{-\beta_n \tau}}{\zeta_n \beta_n}. \tag{D10}$$

The derivation of Eq. D10 is obtained using either of the following identities:

$$\int_0^1 {\Theta_n}^2 \rho d\rho = \frac{1}{2};$$
$$\int_0^1 \frac{I_0\left(Da^{1/2}\rho\right)}{I_0\left(Da^{1/2}\right)}\Theta_n \rho d\rho = \frac{\zeta_n}{Da + {\zeta_n}^2} = \frac{\zeta_n}{Da\beta_n}. \tag{D11}$$

APPENDIX E: Gradient Modeling Details

Kinetic model for receptor activation

The model used in Figs 5.1 d & 5.5 c was adapted from an experimentally validated kinetic model developed previously (Park and others 2003). We start with a model for receptor activation. Defining R, C_1, and C_2 as the density of free receptors, 1:1 receptor-ligand complexes, and functional receptor dimers in the membrane, respectively, and $[L]$ as the concentration of PDGF added at time $t = 0$,

$$C_1 = [L]R/K_{D,} \; ; \tag{E1}$$

$$\frac{\mathrm{d}(R + C_1)}{\mathrm{d}t} = V_S - k_t(R + C_1) + 2\left(k_{-x}C_2 - k_x C_1^{\,2}\right); \tag{E2}$$

$$\frac{\mathrm{d}C_2}{\mathrm{d}t} = k_x C_1^{\,2} - (k_{-x} + k_e)C_2 \; ; \tag{E3}$$

$$R(0) = R_0 = V_S/k_t \; ; \quad C_1(0) = C_2(0) = 0 \, . \tag{E4}$$

Receptor densities are nondimensionalized by scaling R, C_1, C_2, and V_s by the initial surface receptor expression level, R_0; substituting its definition,

$$c_1 = [L]r/K_{D,L} \; ; \tag{E5}$$

$$\frac{\mathrm{d}(r + c_1)}{\mathrm{d}t} = k_t(1 - r - c_1) + 2\left(k_{-x}c_2 - k_x R_0 c_1^{\,2}\right); \tag{E6}$$

$$\frac{\mathrm{d}c_2}{\mathrm{d}t} = k_x R_0 c_1^{\,2} - (k_{-x} + k_e)c_2 \; ; \tag{E7}$$

$$r(0) = 1; \quad c_1(0) = c_2(0) = 0 \, . \tag{E8}$$

The output of the model is the dimer fraction, $d = 2c_2$, calculated as a function of time using standard numerical integration. In a spatial gradient of PDGF, we assume that d is simply determined by the local PDGF concentration, which is justified given that transmembrane receptors tend to diffuse relatively slowly in cell membranes, and that the average receptor activation level, $\langle d \rangle$, is defined by the midpoint PDGF concentration.

At the level of enzyme (PI 3-kinase) recruitment, we assume rapid diffusion of enzyme in the cytosol and pseudo-equilibrium binding with activated receptors. The density of receptor-enzyme complexes at location ξ, RE*(ξ,τ), is thus given by

$$RE^*(\xi,\tau) = \frac{d(\xi,\tau)R_0[E]_{cyt}}{K_{D,E} + [E]_{cyt}}, \tag{E9}$$

where $[E]_{cyt}$ is the enzyme concentration in the cytosol, and $K_{D,E}$ is the effective dissociation constant for the interaction. The average density of receptor-enzyme complexes is thus

$$\langle RE^* \rangle = \frac{\langle d \rangle R_0[E]_{cyt}}{K_{D,E} + [E]_{cyt}} \tag{E10}$$

Assuming conservation of the total number of enzyme molecules, E_{Tot},

$$E_{Tot} = A_{mem}\langle RE^* \rangle + V_{cyt}[E]_{cyt}, \tag{E11}$$

where A_{mem} is the area of the plasma membrane, and V_{cyt} is the volume of the cytosol. Combining Eqs. E9-E11 in dimensionless form, we obtain

$$\begin{gathered} e(\xi,t) = \frac{A_{mem}RE^*(x)}{E_{Tot}} = \alpha d(\xi,t)\left(\frac{1-\langle e \rangle}{\kappa_E + 1 - \langle e \rangle}\right); \\ \langle e \rangle = \frac{1+\kappa_E + \alpha\langle d \rangle - \sqrt{(1+\kappa_E+\alpha\langle d \rangle)^2 - 4\alpha\langle d \rangle}}{2}; \\ \alpha = A_{mem}R_0/E_{Tot}; \quad \kappa_E = V_{cyt}K_{D,E}/E_{Tot}. \end{gathered} \tag{E12}$$

The result in Eq. E12 was given as Eq. 5.8 in Chapter 5 and applies to both the kinetic and quasi-steady state models.

Finally, the dimensionless 3' PI level, x, is determined by $e(\xi,t)$ and is subject to pseudo-first order turnover as justified previously (Park and others 2003; Schneider and Haugh 2004):

$$\frac{dx}{dt} = k_{3PI}\left[e + x_0(1 - \langle e \rangle) - x\right], \quad x(0) = x_0. \tag{E13}$$

Parameter values used in Fig. 5.1 d are given in Table E1. Allowing for cell-to-cell variability in receptor expression, as in Fig. 5.5 c, affects the values of the parameter groupings k_xR_0, α, and κ_E.

Table E1: Kinetic model parameter values.

Parameter	Description	Base value
$K_{D,L}$	PDGF single-site dissociation constant	1.5 nM
$k_x R_0$	Dimerization rate constant	0.3 min-1 *
k_{-x}	Dimer uncoupling rate constant	0.07 min-1
K_e	Dimer endocytosis rate constant	0.15 min-1 †
k_t	Membrane turnover rate constant	0.02 min-1
α	Receptor/enzyme expression ratio	50 *, ‡
κ_E	Dimensionless receptor-enzyme dissociation constant	0.1 ‡
K_{3PI}	3' PI turnover rate constant	1 min-1
X_0	Dimensionless 3' PI density in unstimulated cells	0.05

Adapted from ref. 1. The specific membrane turnover rate k_t assumes a membrane lifetime of ~ 30-60 minutes. * These parameter groupings are proportional to the PDGF receptor expression level and were adjusted for both cells in Fig. 5.5 c by a factor of 0.5. † The endocytic rate constant k_e is reduced here from the value of ~ 0.2 min-1 estimated at 37°C. ‡ These parameter groupings are inversely proportional to the PI 3-kinase expression level and were adjusted for cell 2 in Fig. 5.5 c by a factor of 0.4 (2.5-fold higher PI 3-kinase expression).

Quasi-steady state and spatial models

We find that the shape of the PDGF receptor phosphorylation dose response curve for NIH 3T3 cells(Park and others 2003) is fit well by the empirical function,

$$d = \frac{d_{\max} u^2}{1 + u + u^2}; \quad u = \frac{[L]}{L^*}. \tag{E14}$$

Eq. E14 was given as Eq. 5.7 in Chapter 5. The dimensionless PDGF concentration, u, is related to the actual PDGF concentration through the scaling constant L^*, the concentration of PDGF that yields one-third maximum receptor phosphorylation; a value of 1 nM was used in Fig. 5.3 c and Fig. 5.4 b & c. Fig. 5.1 a–c were generated using Eqs. E14 & E12.

The spatial profiles shown in Fig. 5.4 were produced using FEMLAB finite-element modeling software (Comsol, Burlington, MA) and methods described in Chapter 4. We first generated a smoothed PDGF gradient field, which presented a challenge because the cells partially occlude TIRF excitation of the volume marker (as seen in Figs. 5.2 & 5.4 a). By

fitting TIRF profiles along the four edges of a rectangular region enclosing the cell to polynomial functions, we obtained boundary conditions that allowed the interpolation of the interior points using Laplace's equation:

$$\nabla^2[L] = 0\,. \tag{E15}$$

A spatial map of $\alpha d(\xi)$ (with αd_{max} specified) followed from Eq. E14, and its average value was obtained using the subdomain integration feature in FEMLAB. A spatial map of $e(\xi)$ then followed from Eq. E12. The steady-state profiles of 3' PI density x_t and x_b in the nonadherent (top) and contact area (bottom) portions of the membrane were solved according to

$$\begin{aligned} &\nabla^2 x_t + Da\left[e + x_0\left(1 - \langle e\rangle\right) - x_t\right] = 0; \\ &\nabla^2 x_b + Da\left[x_0\left(1 - \langle e\rangle\right) - x_b\right] = 0, \end{aligned} \tag{E16}$$

subject to matching boundary conditions at the contact area periphery. The parameter *Da* describes the ratio of 3' PI turnover to diffusion (Haugh and Schneider 2004); the smaller its value, the more the 3' PI gradient is blurred by lateral diffusion of the lipid. The lack of receptor-mediated 3' PI production in the bottom domain was characterized previously (Haugh and others 2000; Schneider and Haugh 2004). Finally, normalized TIRF profiles were calculated assuming pseudo-equilibrium binding of AktPH to 3' PIs (Haugh and Schneider 2004):

$$\begin{aligned} &f(\xi) = \left(\sigma \frac{x_b(\xi)}{x_{Tot}} - 1\right) p_{SS}; \\ &p_{SS} = \frac{1 + \kappa_P + \mu x_{Tot} - \sqrt{\left(1 + \kappa_P + \mu x_{Tot}\right)^2 - 4\mu x_{Tot}}}{2}; \\ &\sigma = V_{cyt} / A_{mem} d_{cell}; \quad x_{Tot} = \langle e\rangle + 2x_0\left(1 - \langle e\rangle\right), \\ &\kappa_P = K_{D,P} V_{cyt} / P_{Tot}; \quad \mu = A_{mem} X^* / P_{Tot}\,. \end{aligned} \tag{E17}$$

REFERENCES

Deen WM. 1998. Analysis of Transport Phenomena. New York: Oxford University Press.

Haugh JM, Codazzi F, Teruel M, Meyer T. 2000. Spatial sensing in fibroblasts mediated by 3' phosphoinositides. J. Cell Biol. 151(6):1269-1279.

Haugh JM, Schneider IC. 2004. Spatial analysis of 3' phosphoinositide signaling in living fibroblasts: I. Uniform stimulation model and bounds on dimensionless groups. Biophys. J. 86:589-598.

Park CS, Schneider IC, Haugh JM. 2003. Kinetic analysis of platelet-derived growth factor receptor/phosphoinositide 3-kinase/Akt signaling in fibroblasts. J. Biol. Chem. 278:37064-37072.

Schneider IC, Haugh JM. 2004. Spatial analysis of 3' phosphoinositide signaling in living fibroblasts: II. Parameter estimates for individual cells from experiments. Biophys. J. 86:599-608.